Enclosure 1

OCRWM	ERRATA 002	3. QA: QA 4. Page 1 of 1

1. Condition Report No.	2. DC Tracking Number
CR-2104	39268 DOC.20040405.0005

5. Product DI	6. Title	7. Revision
MDL-NBS-HS-000001	Drift-Scale Coupled Processes (DST and THC Seepage) Models	02

8. Description of Error	9. Clarification/Restriction
1. P.39, Table 4.1-2, last entry row, left column. AMR DI # should be ANL-EBS-MD-000030 and not ANL-EBS-MD-00030.	1. Make editorial correction as follows: P.39, Table 4.1-2, last entry row, left column. AMR DI # should be ANL-EBS-MD-000030 and not ANL-EBS-MD-00030.
2. P. 46, Table 4.1-5, rows 3, 4, and 5, source for top of invert as measured from bottom of drift (invert thickness) has BSC 2003 [DIRS 164052] listed as source in four places in the table. Correct source is BSC 2003 [DIRS 164101].	2. On p. 46, Table 4.1-5, rows 3, 4, and 5, change BSC 2003 [DIRS 164052] to BSC 2003 [DIRS 164101]. Reference to BSC 2003 [DIRS 164052] in Section 9.1 on page 347 should be deleted and reference to BSC 2003 [DIRS 164101] should be added. BSC 2003 [DIRS 164101] is drawing 800-IED-WIS0-00302-000-00A.
3. Page 103, Section 6.5.1, first sentence and page 149, Section 6.7.1, first sentence. A superceded document, BSC 2003 [DIRS 162444], has been used as the source for drift diameter in these two locations in the document. In other locations in the document, the correct document BSC 2003 [DIRS 164069] was cited as source for drift diameter.	3. For consistency BSC 2003 [DIRS 164069] should replace BSC 2003 [DIRS 162444] in Section 6.5.1, page 103, first sentence and Section 6.7.1, page 149, first sentence. Reference to BSC 2003 [DIRS 162444] should be removed from Section 9.1, page 347.
4. P. 317, Section 7.1.12, last paragraph sentences 3 and 4 both inaccurately reflect the boreholes completed (two) at the time that DIRS was locked and the report was approved as well as the work planned at that time. Since this information is not pertinent to the validation of the model, these two sentences should be removed.	4. P. 317, Section 7.1.12, last paragraph, remove sentences 3 and 4, beginning with "One additional borehole" and ending with "induced by open boreholes."

10. Responsible Manager (Print Name)	Initials	Date
Paul R. Dixon	PRD	04/05/04

DOC.20040213.0002

OCRWM	ERRATA 001	3. QA: QA 4. Page 1 of 3

1. Condition Report No.	2. DC Tracking Number
CR-1100	38369

5. Product DI	6. Title	7. Revision
MDL-NBS-HS-000001	Drift-Scale Coupled Processes (DST and THC Seepage) Models	02

8. Description of Error	9. Clarification/Restriction
A search of DIRS indicates you are currently using DIRS Reference 161530 *Drift-Scale Coupled Processes (DST and TH Seepage) Models*, MDL-NBS-HS-000015 REV 00, which has been assigned URN 1087. This document has never been approved and the URN is invalid. The DIRS reference has been marked as bad and cannot be used.	The model report, *Drift-Scale Coupled Processes (DST and THC Seepage) Models* (DI: MDL-NBS-HS-000001 REV02) and associated DIRS have been corrected to reference DIRS 166512 [BSC (Bechtel SAIC Company) 2003. *Drift-Scale Coupled Processes (DST and TH Seepage) Models*. MDL-NBS-HS-000015 REV 00C. Las Vegas, Nevada: Bechtel SAIC Company. ACC: MOL.20030910.0160, TBV-5666.] (See attached, corrected report page 346 and corrected DIRS pages 5.)

10. Responsible Manager (Print Name)	Initials	Date
Paul R. Dixon	PRD	2/17/04

159527 BSC (Bechtel SAIC Company) 2002. *Repository Design, Repository/PA IED Subsurface Facilities Plan Sht. 1 of 5, Sht. 2 of 5, Sht. 3 of 5, Sht. 4 of 5, and Sht. 5 of 5.* DWG-MGR-MD-000003 REV A. Las Vegas, Nevada: Bechtel SAIC Company. ACC: MOL.20020601.0194.

160819 BSC (Bechtel SAIC Company) 2002. *Technical Work Plan for: Performance Assessment Unsaturated Zone.* TWP-NBS-HS-000003 REV 02. Las Vegas, Nevada: Bechtel SAIC Company. ACC: MOL.20030102.0108.

160771 BSC (Bechtel SAIC Company) 2002. *Thermal Testing Measurements Report.* ANL-NBS-HS-000041 REV 00. Las Vegas, Nevada: Bechtel SAIC Company. ACC: MOL.20021004.0314.

160146 BSC (Bechtel SAIC Company) 2002. *Total System Performance Assessment-License Application Methods and Approach.* TDR-WIS-PA-000006 REV 00. Las Vegas, Nevada: Bechtel SAIC Company. ACC: MOL.20020923.0175.

164454 BSC (Bechtel SAIC Company) 2002. *Users Manual (UM) for TOUGHREACT V3.0.* 10396-UM-3.0-00. Las Vegas, Nevada: Bechtel SAIC Company. ACC: MOL.20030411.0090.

161760 BSC (Bechtel SAIC Company) 2002. *Ventilation Model Report.* ANL-EBS-MD-000030 REV 02. Las Vegas, Nevada: Bechtel SAIC Company. ACC: MOL.20030102.0140.

160975 BSC (Bechtel SAIC Company) 2002. *Ventilation Model.* ANL-EBS-MD-000030 REV 01 ICN 01. Las Vegas, Nevada: Bechtel SAIC Company. ACC: MOL.20021106.0055.

160109 BSC (Bechtel SAIC Company) 2003. *Development of Numerical Grids for UZ Flow and Transport Modeling.* ANL-NBS-HS-000015 REV 01. Las Vegas, Nevada: Bechtel SAIC Company. ACC: DOC.20030404.0005.

166512 BSC (Bechtel SAIC Company) 2003. *Drift-Scale Coupled Processes (DST and TH Seepage) Models.* MDL-NBS-HS-000015 REV 00C. Las Vegas, Nevada: Bechtel SAIC Company. ACC: MOL.20030910.0160. TBV-5666.

161519 BSC (Bechtel SAIC Company) 2003. *Interlocking Drip Shield.* 000-MW0-TED0-00101-000-00A, -00102-000-00A, and -00103-000-00A. 3 Sheets. Las Vegas, Nevada: Bechtel SAIC Company. ACC: ENG.20030205.0001; ENG.20030205.0002; ENG.20030205.0003.

164053 BSC (Bechtel SAIC Company) 2003. *Repository Design Project, RDP/PA IED Typical Waste Package Components Assembly 1 of 9.* 800-IED-WIS0-00201-000-00A. Las Vegas, Nevada: Bechtel SAIC Company. ACC: ENG.20030702.0001.

18	NBS-HS-000015 REV 01. Las Vegas, Nevada: Bechtel SAIC Company. ACC: DOC.20030404.0005. 160109			Abbreviations (table on pp. 23-26)		
19	BSC (Bechtel SAIC Company) 2003. *Drift-Scale Coupled Processes (DST and TH Seepage) Models.* MDL-NBS-HS-000015 REV 00C. Las Vegas, Nevada: Bechtel SAIC Company. ACC: MOL.20030910.0160. TBV-5666 166512	Entire	Reference Only	6.6.2.3, 7.1.9, 7.1.10.3	TH processes description	N/A
		6.2.1.1	Reference Only	6.4.1	TH processes description	N/A
		6.2.3	Reference Only	6.8.5.2	Results of drift-scale TH model	N/A
		7	Reference Only	6.4.6.1	Dual-permeability approach validation	N/A
		6.2.3.2.3;Figure 6.2.3.1-3	Reference Only	6.8.5.4	TH simulation results	N/A
		6.2.2	Reference Only	6.5.5.1	TH simulation results	N/A
		6.2.3.2.3	Reference Only	6.6.2.3	Flow focusing evaluations	N/A
20	BSC (Bechtel SAIC Company) 2003. *Interlocking Drip Shield.* 000-MW0-TED0-00101-000-00A, -00102-000-00A, and -00103-000-00A. 3 Sheets. Las Vegas, Nevada: Bechtel SAIC Company. ACC: ENG.20030205.0001; ENG.20030205.0002; ENG.20030205.0003. 161519	Entire	Technical Information	Table 4.1-5	Drip shield thickness	N/A
21	BSC (Bechtel SAIC Company) 2003. *Repository Design Project, RDP/PA IED Typical Waste Package Components Assembly 1 of 9.* 800-IED-WIS0-00201-000-00A. Las Vegas, Nevada: Bechtel SAIC Company. ACC: ENG.20030702.0001. 164053	Entire	Technical Information	Tables 4.1-2, 4.1-5	Waste package outer diameter	N/A
22	BSC (Bechtel SAIC Company) 2003. *Repository Design Project, Repository/PA IED Emplacement Drift Committed Materials 1 of 2.* 800-IED-WIS0-00301-000-00A. Las Vegas,	Entire	Technical Information	Table 4.1-5	Invert thickness	N/A

OCRWM	MODEL COVER SHEET	1. QA: QA Page 1 of 362

DOC.20030804.0004

2. Type of Mathematical Model

☒ Process Model ☐ Abstraction Model ☐ System Model

Describe Intended Use of Model

This Model Report documents the THC Seepage Model and the DST THC Model. The THC Seepage Model is a drift-scale process model for predicting the composition of gas and water that could enter waste-emplacement drifts and the effects of mineral alteration on flow in rocks surrounding drifts. The Drift Scale Test (DST) THC model is a drift-scale process model relying on the same conceptual model and much of the same input data (i.e., physical, hydrological, thermodynamic, and kinetic) as the THC Seepage Model. The DST THC Model is the primary method for validating the THC Seepage Model by comparing predicted water and gas compositions, as well as mineral alteration patterns, with observed data from the Drift Scale Test. These models provide the framework to evaluate THC coupled processes at the drift scale, predict flow and transport behavior for specified thermal-loading conditions, and predict the evolution of mineral alteration and fluid chemistry around potential waste emplacement drifts. The DST THC Model is used solely for the validation of the THC Seepage Model and it is not used for calibration to measured data.

3. Title

Drift-Scale Coupled Processes (DST and THC Seepage) Models

4. DI (including Rev. No. and Change No., if applicable):

MDL-NBS-HS-000001 REV 02

5. Total Attachments	6. Attachment Numbers - No. of Pages in Each
11	I-2, II-4, III-2, IV-4, V-2, VI-4, VII-4, VIII-4, IX-4, X-8, XI-2

	Printed Name	Signature	Date
7. Originator	N. Spycher		7/29/03
8. CSO	M. Zhu		07/29/03
9. Checker	R.A. Wagner	Ralph Wagner	29Jul03
10. QER	S. Harris	Stephen Harris	7-30-03
11. Responsible Manager/Lead	J.S.Y. Wang/Y. Tsang	Jens S. Y. Wang/Yume Tsang	7-30-03
12. Responsible Manager	P. Dixon	Paul	7-30-03

13. Remarks

Block 7. E.L. Sonnenthal contributed to all Sections; P.F. Dobson contributed to Sections 7.2 and 7.3; J. Apps and S. Salah contributed to Section 4; T. Kneafsey contributed to Sections 7.2 and 7.3; C.B. Haukwa contributed to Section 6.6; and C. Valladao contributed to Section 9.

Block 9. P. Persoff is the additional checker for Sections 1-5. Peter Persoff 7/29/03

Technical review on REV 02A-Draft1 per YMP-LBNL-QIP-6.1 performed by: Y. Tsang (Sections 1-3, and 8), P. Dobson (Section 4), T. Xu (Sections 5, 6, and 6.1-6.4), G. Zhang (Sections 6.5-6.8, 7, and 7.1), J. Apps (Sections 7.2 and 7.3), C. Guay (Attachments).
Second independent technical review on REV 02A-Draft3 performed by J. Apps on entire Model Report.

Technical Error Report (TER) log number addressed in this Model Report
TER-02-0077

OFFICE OF CIVILIAN RADIOACTIVE WASTE MANAGEMENT
MODEL REVISION RECORD

2. Model Title:
Drift-Scale Coupled Processes (DST and THC Seepage) Models

3. DI (including Rev. No. and Change No., if applicable):
MDL-NBS-HS-000001 REV 02

4. Revision/Change No.	5. Description of Revision/Change
REV00	Initial Issue
REV01	Incorporated additional data from DST for model validation. Incorporated sensitivity studies, including effect of backfill versus no backfill. Additional Models/Updates: REV01 DST THC Model; Tptpmn THC No-Backfill Model; Tptpmn THC Heterogeneous Model; Tptpll THC Model; Plug-Flow Reactor Model Validation
REV01/ICN 01	Incorporated minor editorial changes to text and references. Incorporated additional figure (Figure 32b). Incorporated auditor's recommendations (Audit M&O-ARP-01-02). All changes are marked by a black vertical line on the margin of the affected page.
REV01/ICN02	-Removed incorrect reference DTN: MO0008THRMODYN.000 [153742], inserted correct reference DTN: MO0009THRMODYN.001 [152576] (this impacted sections 4, 8.3 and attachments V and VI). -Made editorial correction in section 5.A.7. -Added assumption 20 to section 5.A, to identify DTN: LA0008SC12213N.001 [153386] as data that augments DTN: MO0009THRMODYN.001 [152576]. -Revised three assumptions to indicate no further confirmation is required as the assumptions were adequately justified (C-1, C-4, and C-6). Revision of assumptions resulted in the removal of TBVs 5028, 5029, and 5030 in the Document Input Reference System (DIRS). -Updated section 8.3 to remove URNs where appropriate. -Changes to data status made in DIRS. -The following sections were revised in REV 01 ICN 02: Section 1 (p. 23), 2 (p. 27), 3 (p. 30), 4 (pp. 33, 37-38, 42), 5 (pp. 50, 53, 55), 6 (p. 107), 7 (p. 225), 8 (pp. 228-229, 235-240), Att. V (p. V-3), and VI (p. VI-3)
REV 02	Entire model documentation was revised. Side bars are not used because the changes were too extensive to use Step 5.9d)1) per AP-SIII.10Q/Rev.1/ICN 2.

CONTENTS

CONTENTS (continued)

CONTENTS (continued)

CONTENTS (continued)

LIST OF FIGURES

LIST OF FIGURES (Continued)

LIST OF FIGURES (Continued)

LIST OF FIGURES (Continued)

LIST OF FIGURES (Continued)

LIST OF FIGURES (Continued)

LIST OF FIGURES (Continued)

LIST OF FIGURES (Continued)

LIST OF FIGURES (Continued)

LIST OF FIGURES (Continued)

LIST OF FIGURES (Continued)

INTENTIONALLY LEFT BLANK

LIST OF TABLES

LIST OF TABLES (continued)

ACRONYMS

1-D	one-dimensional
2-D	two-dimensional
3-D	three-dimensional
ACC	Accession Number
AP	Administrative Procedure (DOE)
BET	Brunauer-Emmett-Teller
BSC	Bechtel SAIC Company, LLC
CRWMS	Civilian Radioactive Waste Management System
DIRS	Document Input Reference System
DOE	Department of Energy
DST	Drift Scale Test
DTN	Data Tracking Number
ECRB	Enhanced Characterization of Repository Block
EOS	Equation of State
ESF	Exploratory Studies Facility
FEP	Features, Events and Processes
Kth_{max}	Maximum Thermal Conductivity
LA	License Application
LBNL	Lawrence Berkeley National Laboratory
M&O	Management and Operating Contractor
NRC	Nuclear Regulatory Commission
OCRWM	Office of Civilian Radioactive Waste Management
PA	Performance Assessment
Q	Qualified
QA	Quality Assurance
QIP	Quality Implementing Procedure
SCM	Software Configuration Management
SN	Scientific Notebook
SR	Site Recommendation
STN	Software Tracking Number

ACRONYMS (continued)

TDMS	Technical Data Management System
TH	Thermal-Hydrological
THC	Thermal-Hydrological-Chemical
TSPA	Total System Performance Assessment
TWP	Technical Work Plan
UZ	unsaturated zone
UZ Model	Unsaturated Zone Flow and Transport Model
XRD	X-ray Diffraction
YMP	Yucca Mountain Project
YMRP	*Yucca Mountain Review Plan, Final Report*
WP	Waste Package

Major Hydrogeologic Units

CFu	Crater Flat undifferentiated hydrogeologic unit
CHn	Calico Hills nonwelded hydrogeologic unit
PTn	Paintbrush Tuff nonwelded hydrogeologic unit
TCw	Tiva Canyon welded hydrogeologic unit

Geologic and Model Layer Abbreviations

Stratigraphic Unit[a]						Abbreviation[a]	UZ Model Layer[b]
Group	Formation	Member	Zone	Subzone			
	Alluvium and Colluvium					Qal, Qc	
Timber Mountain Group						Tm	
	Rainier Mesa Tuff					Tmr	
Paintbrush Group						Tp	
		Post-tuff unit "x" bedded tuff				Tpbt6	
		Tuff unit "x"				Tpki (informal)	
		Pre-tuff unit "x" bedded tuff				Tpbt5	
	Tiva Canyon Tuff					Tpc	
		Crystal-Rich Member				Tpcr	
			Vitric zone			Tpcrv	
				Nonwelded subzone		Tpcrv3	
				Moderately welded subzone		Tpcrv2	
				Densely welded subzone		Tpcrv1	
			Nonlithophysal subzone			Tpcrn	tcw11
				Subvitrophyre transition subzone		Tpcrn4	
				Pumice-poor subzone		Tpcrn3	
				Mixed pumice subzone		Tpcrn2	
				Crystal transition subzone		Tpcrn1	
			Lithophysal zone			Tpcrl	
				Crystal transition subzone		Tpcrl1	
		Crystal-Poor Member				Tpcp	
			Upper lithophysal zone			Tpcpul	
				Spherulite-rich subzone		Tpcpul1	
			Middle nonlithophysal zone			Tpcpmn	
				Upper subzone		Tpcpmn3	
				Lithophysal subzone		Tpcpmn2	tcw12
				Lower subzone		Tpcpmn1	
			Lower lithophysal zone			Tpcpll	
				Hackly-fractured subzone		Tpcpllh	
			Lower nonlithophysal zone			Tpcpln	

Geologic and Model Layer Abbreviations (continued)

Stratigraphic Unit[a]					Abbreviation[a]	UZ Model Layer[b]
Group	Formation	Member	Zone	Subzone		
				Hackly subzone	TpcpInh	tcw12 (continued)
				Columnar subzone	TpcpInc	
			Vitric zone		Tpcpv	tcw13
				Densely welded subzone	Tpcpv3	
				Moderately welded subzone	Tpcpv2	
				Nonwelded subzone	Tpcpv1	ptn21
		Pre-Tiva Canyon bedded tuff			Tpbt4	ptn22
	Yucca Mountain Tuff				Tpy	ptn23
		Pre-Yucca Mountain bedded tuff			Tpbt3	ptn24
	Pah Canyon Tuff				Tpp	ptn 25
		Pre-Pah Canyon bedded tuff			Tpbt2	ptn26
	Topopah Spring Tuff				Tpt	
		Crystal-Rich Member			Tptr	
			Vitric zone		Tptrv	
				Nonwelded subzone	Tptrv3	
				Moderately welded subzone	Tptrv2	
				Densely welded subzone	Tptrv1	tsw31
			Nonlithophysal zone		Tptrn	tsw32
				Dense subzone	Tptrn3	
				Vapor-phase corroded subzone	Tptrn2	
				Crystal transition subzone	Tptrn1	
			Lithophysal zone		Tptrl	tsw33
				Crystal transition subzone	Tptrl1	
		Crystal-Poor Member			Tptp	
			Lithic-rich zone		Tptpf or Tptrf	
			Upper lithophysal zone		Tptpul	
			Middle nonlithophysal zone		Tptpmn	tsw34
				Nonlithophysal subzone	Tptpmn3	
				Lithophysal bearing subzone	Tptpmn2	
				Nonlithophysal subzone	Tptpmn1	
			Lower lithophysal zone		Tptpll	tsw35
			Lower nonlithophysal zone		Tptpln	tsw36, tsw37

Geologic and Model Layer Abbreviations (continued)

Stratigraphic Unit[a]					Abbreviation[a]	UZ Model Layer[b]
Group	Formation	Member	Zone	Subzone		
			Vitric zone		Tptpv	tsw38
				Densely welded subzone	Tptpv3	
				Moderately welded subzone	Tptpv2	tsw39
				Nonwelded subzone	Tptpv1	ch1
		Pre-Topopah Spring bedded tuff			Tpbt1	
	Calico Hills Formation				Ta	ch2, ch3, ch4, ch5
		Bedded tuff			Tacbt	ch6
Crater Flat Group					Tc	pp4
	Prow Pass Tuff				Tcp	
		Prow Pass Tuff upper vitric nonwelded zone			Tcpuv	
		Prow Pass Tuff upper crystalline nonwelded zone			Tcpuc	pp3
		Prow Pass Tuff moderately-densely welded zone			Tcpmd	pp2
		Prow Pass Tuff lower crystalline nonwelded zone			Tcplc	
		Prow Pass Tuff lower vitric nonwelded zone			Tcplv	pp1
		Pre-Prow Pass Tuff bedded tuff			Tcpbt	
	Bullfrog Tuff				Tcb	
		Bullfrog Tuff upper vitric nonwelded zone			Tcbuv	
		Bullfrog Tuff upper crystalline nonwelded zone			Tcbuc	bf3
		Bullfrog Tuff welded zone			Tcbmd	
		Bullfrog Tuff lower crystalline nonwelded zone			Tcblc	
		Bullfrog Tuff lower vitric nonwelded zone			Tcblv	bf2
		Pre-Bullfrog Tuff bedded tuff			Tcbbt	
	Tram Tuff				Tct	
		Tram Tuff upper vitric nonwelded zone			Tctuv	

Geologic and Model Layer Abbreviations (continued)

Stratigraphic Unit[a]						Abbreviation[a]	UZ Model Layer[b]
Group	Formation	Member	Zone	Subzone			
				Tram Tuff upper crystalline nonwelded zone		Tctuc	
				Tram Tuff moderately-densely welded zone		Tctmd	tr3
				Tram Tuff lower crystalline nonwelded zone		Tctlc	
				Tram Tuff lower vitric nonwelded zone		Tctlv	
		Pre-Tram Tuff bedded tuff				Tctbt	
		Lava and flow breccia (informal)				Tll	
		Bedded tuff				Tllbt	
	Lithic Ridge Tuff					Tr	
		Bedded tuff				Tlrbt	
		Lava and flow breccia (informal)				Tll2	
		Bedded tuff				Tllbt	
		Lava and flow breccia (informal)				Tll3	tr2
		Bedded tuff				Tll3bt	
		Older tuffs (informal)				Tt	
			Unit a (informal)			Tta	
			Unit b (informal)			Ttb	
			Unit c (informal)			Ttc	
		Sedimentary rocks and calcified tuff (informal)				Tca	
		Tuff of Yucca Flat (informal)				Tyf	
Pre-Tertiary sedimentary rock							
	Lone Mountain Dolomite					Slm	
	Roberts Mountain Formation					Srm	

Sources: [a] BSC 2002 [159124], Table 4.
[b] BSC 2003 [160109], Table 11.

CHEMICAL ABBREVIATIONS

Elements

Al	Aluminum
C	Carbon
Ca	Calcium
Cl	Chlorine
F	Fluorine
Fe	Iron
H	Hydrogen
K	Potassium
Mg	Magnesium
N	Nitrogen
Na	Sodium
O	Oxygen
S	Sulfur
Si	Silicon

Chemical Compounds, Aqueous Species and Gases

AlO_2	Aluminum primary aqueous species (essentially same as $Al(OH)_4^-$); here used to describe total aqueous aluminum concentrations as AlO_2
CO_2	Carbon dioxide gas
H_2O	Water
HCO_3^-	Bicarbonate aqueous species; here used to describe total aqueous
$HFeO_2^0$	Iron primary aqueous species (essentially same as $Fe(OH)_3^0$; here used to describe total aqueous iron concentrations as $HFeO_2^0$
KSO_4	Potassium sulfate (solid; mineral name: arcanite)
$MgSO_4$	Magnesium sulfate (solid)

CHEMICAL ABBREVIATIONS (continued)

Na_2SO_4	Sodium sulfate (solid; mineral name: thenardite)
NaCl	Sodium chloride (solid; mineral name: halite)
$NaNO_3$	Sodium nitrate (solid)
NO_3^-	Nitrate aqueous species
O_2	Oxygen gas
P_{CO2}	Carbon dioxide partial pressure (in bar)
pH	Negative logarithm of the hydrogen ion activity
SiO_2	Silica
SO_4^{-2}	Sulfate aqueous species

Chemical Units

meq	milliequivalent (mol x 10^3 x ionic charge)
meq/L	milliequivalent per liter of solution
mg/L	milligram per liter of solution
mol	moles
mol/kg	moles per kilogram water (molality)
ppm	parts per million
ppmv	parts per million volume

1. PURPOSE

1.1 BACKGROUND

The purpose of this Model Report (REV02) is to document the unsaturated zone (UZ) models used to evaluate the potential effects of coupled thermal-hydrological-chemical (THC) processes on UZ flow and transport. This Model Report has been developed in accordance with the *Technical Work Plan for: Performance Assessment Unsaturated Zone* (Bechtel SAIC Company, LLC (BSC) 2002 [160819]). The technical work plan (TWP) describes planning information pertaining to the technical scope, content, and management of this Model Report in Section 1.12, Work Package AUZM08, *Coupled Effects on Flow and Seepage*. The plan for validation of the models documented in this Model Report is given in Attachment I, Model Validation Plans, Section I-3-4, of the TWP. Except for variations in acceptance criteria (Section 4.2), there were no deviations from this TWP. This report was developed in accordance with AP-SIII.10Q, *Models*.

This Model Report documents the THC Seepage Model and the Drift Scale Test (DST) THC Model. The THC Seepage Model is a drift-scale process model for predicting the composition of gas and water that could enter waste emplacement drifts and the effects of mineral alteration on flow in rocks surrounding drifts. The DST THC model is a drift-scale process model relying on the same conceptual model and much of the same input data (i.e., physical, hydrological, thermodynamic, and kinetic) as the THC Seepage Model. The DST THC Model is the primary method for validating the THC Seepage Model. The DST THC Model compares predicted water and gas compositions, as well as mineral alteration patterns, with observed data from the DST. These models provide the framework to evaluate THC coupled processes at the drift scale, predict flow and transport behavior for specified thermal-loading conditions, and predict the evolution of mineral alteration and fluid chemistry around potential waste emplacement drifts. The DST THC Model is used solely for the validation of the THC Seepage Model and is not used for calibration to measured data.

Data developed with the THC Seepage Model are to be abstracted for inclusion in the Model Report *Abstraction of Drift-Scale Coupled Processes* (upcoming revision of MDL-NBS-HS-000018 REV00 (CRWMS M&O 2000 [123916])). The abstracted results are used for Performance Assessment (PA). PA results support the License Application (LA).

The work scope for this Model Report is presented in the TWP cited above and summarized as follows: continue development of the repository drift-scale THC Seepage Model used in support of the Total System Performance Assessment (TSPA) in-drift geochemical model; study sensitivity of results to changes in input data and mineral assemblage; validate the models by comparison with field and experimental data; perform simulations to predict mineral dissolution and precipitation and their effects on fracture properties and chemistry of water (but not flow rates) that may seep into drifts; submit modeling results to the Technical Data Management System (TDMS) and document the models; and evaluate model uncertainty and the effect of uncertainty propagation to other models.

Major revisions in this document (REV02) compared to previous versions (REV00 and REV01) include the addition of new simulations that make use of improved treatment of various modeled

processes, together with updated rock properties and some new kinetic and thermodynamic input data. In addition, the uncertainties associated with predictions of the THC Seepage Model are further evaluated by considering five different input water compositions, some variations in infiltration rates, CO_2 effective diffusivity, and the effect of vapor-pressure lowering due to capillary pressure. Results of earlier THC work considering the emplacement of backfill over waste canisters has been removed from this revision, because the use of backfill is no longer being considered.

1.2 OVERVIEW OF MODELS

The DST THC Model, constructed for the DST, is used to investigate THC processes during the DST. The spatial scale and temperatures for the DST are similar to those for current designs of the repository. This similarity, combined with the relatively long time that it has been operating (four years of heating, ending in January 2002, and monitoring is continuing during cooling), makes the DST the best available experiment for validating drift-scale THC coupled process models (such as the THC Seepage Model). Measured data from the DST are used to evaluate and validate the conceptual and numerical models. Throughout the DST study, the conceptual model and its numerical formulation were improved and revised as necessary, so that results of the DST and laboratory experiments could be best reproduced. These revisions did not incorporate any adjustments to measured geochemical data.

The THC Seepage Model provides an analysis of the effects of THC processes on percolation water chemistry and gas-phase composition in the near-field host rock around the emplacement drifts. This analysis includes a complete description of the pertinent mineral-water processes in the host rock and their effect on the near-field environment. Several alternative conceptualizations of the THC Seepage Model (see below) are used to evaluate the effects of mineral dissolution and precipitation, the effects of CO_2 exsolution and transport in the region surrounding emplacement drifts, the potential for forming calcite, silica, or other mineral assemblage "precipitation caps," and the resulting changes to porosity, permeability, and percolation. Sensitivity studies are documented on the effect of varying rock properties, including fracture-permeability heterogeneity, reaction rates, repository emplacement-horizon lithology, geochemical systems, infiltration rates, and input water compositions. The effects of various model refinements and improvements implemented through successive revisions of this report are also documented. These include, for example, the effects of improved treatment of porosity-permeability coupling, improved treatment of mineral precipitation at the boiling front, and consideration of vapor-pressure lowering caused by capillary pressure.

The following designations have been assigned to the models and their alternative conceptualizations presented in this report:

- DST THC Model REV01: DST THC Model and simulations developed for the previous revision (REV01) of this Model Report (Section 7.1).
- DST THC Model REV02: DST THC Model and simulations developed for the current Model Report revision (Section 7.1). This model is an update of the DST THC model, using the same general setup except for updated rock properties and other various input data.

- Tptpmn THC Model REV01: THC Seepage Model considering a heat load in the Topopah Spring Tuff middle nonlithophysal lithostratigraphic unit (Tptpmn) (Section 6.5). This model was developed for REV01 of this Model Report.

- Tptpmn THC Heterogeneous Model REV01: THC Seepage Model considering a heat load in the Tptpmn with initial heterogeneous fracture permeability variations (Section 6.6). This model uses the same grid and THC parameters as in the Tptpmn THC Model. It was developed for the previous revision (REV01) of this Model Report.

- Tptpll THC Model REV01: THC Seepage Model considering a heat load in the Topopah Spring Tuff lower lithophysal lithostratigraphic unit (Tptpll) (Section 6.7). This model was developed for the previous revision (REV01) of this Model Report.

- Tptpll THC Model REV02: THC Seepage Model developed for this current Model Report revision (Section 6.8). This model is an update of the Tptpll THC Model REV01, using the same general setup except for updated rock properties and other various input data.

The first two models are collectively referred to as the DST THC Model, and the last four as alternative conceptualizations of the THC Seepage Model. These models are fully described in Sections 6 and 7.

It should be noted, here, that results handed to downstream users for LA work consist only of the Tptpll THC Model REV02 results. Other historical (REV01) results are presented here because they provide important complementary information to REV02 work with respect to the evaluation of model output uncertainty.

These REV01 results are treated as sensitivity analyses. As mentioned later in this report, the Tptpll THC Model REV02 was run using a range of input water compositions from various lithostratigraphic units (including Tptpmn, Tptpll, and Tptpul) and representative of natural variability. The spread in model results from the use of these different water compositions mostly encompasses the spread related to other factors such as drift location and infiltration rate, and other model conceptualizations discussed in Section 6.3. Therefore, the REV02 model results for the Tptpll unit (taking into account the variability introduced by the different input water compositions) should be applicable to other repository host rock units.

1.3 MODEL LIMITATIONS

A limitation of the THC Seepage Model, as in all predictive models, is the increased uncertainty associated with predictions required for times far beyond the duration of field tests. The model is also limited by its mathematical formulations and associated assumptions (Section 5) and approximations (Section 6.4.6). For example, neither the THC Seepage nor DST THC models were designed for accurate computation of mineral precipitation from very saline waters (ionic strength > 4 molal) resulting from evaporative concentration. Other model limitations affecting the uncertainty of model results are discussed in Section 6.9. Another limitation of the THC Seepage Model is that it is computationally intensive (run times up to ten days for one simulation). Hence, the number of simulations that have been performed for sensitivity study is

limited. Nevertheless, these limitations were for the most part overcome by evaluating the model sensitivity to key input parameters (Sections 6.5–6.8), and by comparing model results against data from the DST and laboratory experiments (Section 7). Also, the model conceptualization and mathematical formulation (Section 6.2–6.4) have been improved, through the successive revisions of this Model Report, such that a reasonably good agreement between calculated and measured data has been achieved.

The THC Seepage Model was developed with data for the Tptpmn and Tptpll lithostratigraphic units. Although many aspects of the model are applicable to other host rock units of the repository, differences in the mineralogy, geochemistry, and thermal-hydrological (TH) properties must be considered before the results can be directly applied elsewhere. These differences, however, are expected to be reflected in the range of pore-water compositions input into the model (Section 6.2.2.1), such that results of the THC Seepage Model as a whole (i.e., including the variability introduced by using various input water compositions) could be reasonably applied to other locations within the repository footprint. One limitation of the model is that it is a continuum model, with averaged properties or realizations of idealized permeability fields, and therefore is meant to represent overall changes in space and time. Thus, it must be applied with caution at any specific location.

The DST THC Model is a two dimensional (2-D) representation with homogeneous properties of a three-dimensional (3-D) experiment in heterogeneous fractured rock. Therefore, the model is meant to capture overall changes as a function of space and time, but cannot be expected to match data exactly at any one point in time.

By definition, models are idealizations of the real world. Input data summarized in Section 4 characterize the physical properties of the rock, but cannot include every detail of a natural system. In particular, the infiltration of water is laterally uniform over the model top boundary. As a result of such simplifications, the model results describe overall changes in space and time within the model domain, but must be applied with caution when predicting future conditions at any specific location.

The various alternative conceptualizations of the THC Seepage Model presented in this report consider a half-drift symmetrical and laterally homogenous model (thus resulting in the symmetric flow of heat away from one emplacement drift). Therefore, these conceptualizations cannot capture potential "edge effects" that could occur as the result of uneven heat flow around drifts at the boundaries of the repository. Edge effects have been evaluated with mountain-scale simulations in BSC (2001 [155950], Section 3.3.6) and will be further addressed in an upcoming revision (REV01) of MDL-NBS-HS-000007 (CRWMS M&O 2000 [144454]). Water and gas compositions predicted at the edge of the repository (BSC 2001 [155950], Section 3.3.6) are within the range of compositions simulated in this Model Report. For this reason, results presented here could be used to represent potential effects of THC processes on the composition of seepage at all waste package locations.

2. QUALITY ASSURANCE

Development of this Model Report and the supporting modeling activities have been determined to be subject to the Yucca Mountain Project's quality assurance (QA) program as indicated in *Technical Work Plan for: Performance Assessment Unsaturated Zone,* TWP-NBS-HS-000003 REV 02 (BSC 2002 [160819], Section 8.2, Work Package (WP) AUZM08). Approved QA procedures identified in the TWP (BSC 2002 [160819], Section 4) have been used to conduct and document the activities described in this Model Report. Electronic management of information was evaluated in accordance with Administrative Procedure (AP) SV.1Q, *Control of the Electronic Management of Information* and controlled under YMP-LBNL Quality Implementing Procedure—(QIP) SV.0, *Management of YMP-LBNL Electronic Data,* as planned in BSC (2002 [160819], Section 8.4).

This Model Report provides drift-scale THC processes of natural barriers that are important to the demonstration of compliance with the postclosure performance objective prescribed in 10 CFR 63.113 [156605]. Therefore it is classified as "Quality Level – 1" with regard to importance to waste isolation as defined in AP-2.22Q, *Classification Criteria and Maintenance of the Monitored Geologic Repository Q-List.* The report contributes to the analyses and modeling data used to support performance assessment (PA); the conclusions do not directly impact engineered features important to safety, as defined in AP-2.22Q.

INTENTIONALLY LEFT BLANK

3. USE OF SOFTWARE

The qualified software used in this study are listed in Table 3.1. These software have been baselined in accordance with AP-SI.1Q, *Software Management*, are appropriate for the intended use, have been used strictly within the range of validation, and were obtained from the Software Configuration Management (SCM).

TOUGHREACT V2.4 (LBNL 2001 [160880]), and V3.0 (LBNL 2002 [161256]) are the primary codes used for the DST THC and THC Seepage models. (Only use of TOUGHREACT V3.0 was planned in BSC 2002 [160819], Attachment II; both codes are qualified.) The code SOLVEQ/CHILLER V1.0 (LBNL 1999 [153217]) was utilized to prepare water-chemistry data for input to the models. SUPCRT92 V1.0 (LBNL 1999 [153218]) was used to generate thermodynamic data for use by SOLVEQ/CHILLER V1.0 (LBNL 1999 [153217]) and the various TOUGHREACT versions. The code TOUGH2 V1.4 (LBNL 2000 [146496]) was used to generate boundary conditions. The code AMESH V1.0 (LBNL 1999 [153216]) was used to generate grids for the models, and GSLIB V1.0SISIMV1.204 (LBNL 2000 [153100]) was used to create geostatistical permeability realizations. Other routines listed in Table 3.1 were used for various data pre- and post-processing tasks.

Results of historical simulations performed for Site Recommendation (SR), first presented in the previous revision (REV01) of this Model Report, are included in this report to supplement the results of more recent simulations carried out for this report revision (REV02). These earlier simulations, carried out only for SR, were for the most part run using an interim unqualified version of TOUGHREACT (Version 2.3, LBNL 2001 [153101]) because interim use of unqualified software was allowed for SR work. During the validation process, the source code for TOUGHREACT V2.3 changed to TOUGHREACT V2.4 (LBNL 2001 [160880]) which was subsequently validated and baselined. A comparison of unqualified TOUGHREACT V2.3 with qualified TOUGHREACT V2.4 was performed including an associated impact review, which concluded that the simulations with unqualified V2.3 were verified with the qualified V2.4 BSC (2001 [164414]).

This Model Report documents the DST THC and THC Seepage models as listed in Section 1. The input and output files for the model runs presented in this Model Report are listed in Attachment X.

Table 3-1. Qualified Software Used in This Report

Software Name and Version	Software Tracking Number (STN)	DIRS Reference Number
TOUGHREACT V3.0	10396-3.0-00	161256
TOUGHREACT V2.4	10396-2.4-00	160880[1]
TOUGHREACT V2.2	10154-2.2-00	153219 (retired)[1]
SOLVEQ/CHILLER V1.0	10057-1.0-00	153217
SUPCRT92 V1.0	10058-1.0-00	153218
TOUGH2 V1.4	10007-1.4-01	146496
AMESH V1.0	10045-1.0-00	153216
GSLIB V1.0SISIMV1.204	10397-1.0SISIMV1.204-00	153100
flipk V1.0	10320-1.0-00	152883
switch V1.0	10322-1.0-00	152899
regress V1.0	10321-1.0-00	152900
mk_incon V1.0	10350-1.0-00	152901
kreg V1.0	10318-1.0-00	152902
KREG V1.1	10318-1.1-00	161258
kswitch V1.0	10319-1.0-00	153087
KSWITCH V1.1	10319-1.1-00	161259
THERMOCHK V1.1	10895-1.1-00	161262
DBCONV V1.0	10893-1.0-00	161263
CUTCHEM V1.0	10898-1.0-0.0	161127
exclude.f V1.0	10316-1.0-00	153089
assign.f V1.0	10315-1.0-00	153090
merggrid2.f V1.0	10314-1.0-00	153091
mk_circ2 V1.0	10312-1.0-00	153092
mk_rect2 V1.0	10313-1.0-00	153093
2kgridv1a.for V1.0	10382-1.0-00	153067
mk_grav2.f V1.0	10379-1.0-00	153068
sav1d_dst2d.f V1.0	10381-1.0-00	153083
mrgdrift.f V1.0	10380-1.0-00	153082
avgperm.f V1.0	10378-1.0-00	153085

[1] Software used for historical simulations only – not used for REV02 simulations

4. INPUTS

4.1 DATA AND PARAMETERS

This section presents all input data used for the drift-scale coupled-processes models feeding TSPA-LA activities (simulations presented in Section 6.8). The qualified (Q) status of all direct inputs is shown in the Document Input Reference System (DIRS) database. Because this Model Report documents models of coupled phenomena, a wide variety of input data is required. Sources of direct input data are summarized in Table 4.1-1, and sources of design technical information are reported in Table 4.1-2. Input data and parameter uncertainties are further addressed in Sections 6 and 7. Model inputs related to sensitivity analyses and model validation are documented in Sections 6.4.8 and 7.

Results of historical simulations carried out for REV01 of this Model Report are presented in this report revision (Sections 6.5–6.7, 7.1.8, 7.2) to supplement results of more recent (REV02) work (Section 6.8 and 7.1). These REV01 simulations were included in this report because they provide valuable information for assessing the sensitivity of THC models to various input data and model improvements from REV01 to REV02. These historical simulations were not used to generate any results for TSPA-LA; their sources are presented in Section 6.4.8.

No unqualified data have been qualified in the report. The status of unqualified data used is indicated in the DIRS.

4.1.1 Hydrological and Thermal Properties

Source DTNs for hydrological and thermal properties are listed in Table 4.1-1. Specific values of hydrological and thermal properties for the repository hydrogeologic model units tsw33, tsw34, and tsw35 (Topopah Spring Tuff upper-lithophysal, middle-nonlithophysal, and lower-lithophysal units, respectively) are summarized later in Section 6 (Table 6.4-1).

Modeling analyses utilized data from the "mean calibrated" hydrological property sets for the present-day climate. The data sets include properties that were calibrated, such as fracture and matrix permeabilities and van Genuchten parameters, and properties such as porosity, heat capacity, and thermal conductivity obtained from field measurements. DTNs for infiltration rates and model-boundary temperatures are also included in Table 4.1-1. Specific hydrological and thermal properties for the in-drift components of the THC Seepage Model are given in Section 4.1.7.

4.1.2 Mineralogical Data

These input data consist of mineral volume fractions per total solid volume and their reactive surface areas. Reactive surface areas are used to characterize minerals either in the matrix of the rock (cm^2/g mineral), or those on the surface of fractures (m^2/m^3 of total medium, including pore space), respectively.

These data were taken from DTN: LB0101DSTTHCR1.002 [161277] and DTN: LB0101DSTTHCR1.004 [161279]. For convenience, these data are shown in Attachment II (volume fractions) and Attachment IV (reactive surface areas), respectively. The mineralogical data are for a stratigraphic column near the center of the repository.

Table 4.1-1. Data Tracking Numbers for Sources of Direct Input Data for the Drift-Scale Coupled-Processes Models Used to Feed TSPA-LA Activities

DTNs	Data/Parameter Description[1]
Hydrological and Thermal Rock Properties	
LB991091233129.006 [111480]	Fracture tortuosity
LB0205REVUZPRP.001 [159525]	Fracture parameters: permeability, porosity, van Genuchten m, residual saturation, satiated saturation, fracture frequency, fracture to matrix area
LB0208UZDSCPMI.002 [161243]	Fracture and matrix van Genuchten alpha, matrix permeability
LB0207REVUZPRP.002 [159672]	Matrix parameters: van Genuchten m, residual saturation, satiated saturation
LB0210THRMLPRP.001 [160799]	Matrix porosity and thermal properties: dry- and wet-rock grain conductivity, grain specific heat, and grain density
LL000114004242.090 [142884]	Infiltration rates—average infiltration rate (mean, lower bound, and upper bound for present day, monsoon, and glacial transition climates) from the TH drift-scale models.
Mineralogical Data	
LA9908JC831321.001 [113495]	Model input and output files for Mineralogic Model "MM3.0" Version 3.0.
LA0009SL831151.001 [153485]	Mineralogical characterization of the ESF SHT Block
LA9912SL831151.001 [146447] LA9912SL831151.002 [146449]	DST and SHT fracture mineralogy data
LB0101DSTTHCR1.002 [161277][2] LB0101DSTTHCR1.004 [161279][2]	Mineral volume fractions Mineral surface areas
Kinetic Data	
LB0307KNTDBRTM.001 [164433]	Rate constants and activation energies
Thermodynamic Data	
LB0307THMDBRTM.001 [164434]	Thermodynamic data for aqueous species and minerals: equilibrium constants, molecular weights, molar volumes, Debye-Hückel parameters, CO_2 molecular diameter
Analytical Water and Gas Chemistry Data	
MO0005PORWATER.000 [150930]	Analyses of pore waters from Alcove 5 core samples in the ESF (HD-PERM-2 and HD-PERM-3 samples)
GS020408312272.003 [160899]	Pore water analyses from Cross Drift and USW SD-9 borehole core samples (see Table 4.1-3)
Tptpmn and Tptpll THC Model Grid Data	
LB990501233129.004 [111475]	Stratigraphy (Z coordinates of hydrogeologic units) for: Borehole USW SD-9 (column i64) in UZ site-scale calibration model grid (Tptpmn THC models) Central location (column j34) (Tptpll THC Model)
LB990701233129.002 [125604]	Top and bottom boundary temperatures, pressure, liquid/gas saturations, and boundary elevations
LB990601233124.001 [105888]	Permeability Measurements in Tptpmn

NOTES: [1] Values of thermal and hydrological properties used in the THC models are summarized in Table 6.4-1
[2] Intermediate results from REV01. These can be used here or in future report revisions.

Table 4.1-2. Sources of Technical Information Used as Direct Input for Model Design Used to Feed TSPA-LA Activities

DTNs/Sources	Parameter Description
Repository Drift Design Data	
800-IED-EBS0-00402-000-00B (BSC 2003 [161727])	Drift spacing
800-IED-EBS0-00201-000-00A (BSC 2003 [164069])	Drift diameter
800-IED-WIS0-00201-000-00A (BSC 2002 [164053])	Waste package diameter
CRWMS M&O 2000 [151014]	Hydrological and thermal properties of drift design elements (Table 4.1-5)
SN0002T0872799.009 [153364]	Effective thermal conductivity
CRWMS M&O 2000 [149137] (Design Criterion, p. 23)	Lower-invert thermal conductivity
BSC 2002 [159906]	Upper-invert thermal conductivity
800-IED-EBS0-00403-000-00B (BSC 2003 [161731])	Heat load (1.45 kW/m) (see text)
ANL-EBS-MD-00030 REV01 ICN 01 (BSC 2002 [160975], Table 6-6) [1]	Heat removal by ventilation (86.3%)

NOTE: [1] This has been superseded by BSC (2002 [161760], Table 6-5) showing slightly smaller (84%) heat removal. The impact of this difference on rock temperature around the drift is much smaller than the range of temperature conditions evaluated.

4.1.3 Water and Gas Chemistry

Sources of water- and gas-chemistry data are provided in Table 4.1-1. The pore-water compositions used as inputs to the models are shown in Table 4.1-3.

The only nearly complete pore-water analyses available at the start of these investigations, for samples collected from a repository unit near the repository footprint, were obtained in 1998 from the Tptpmn geologic unit in Alcove 5 near the DST. At the time, three pore-water samples were ultracentrifuged from Alcove 5 core. These analyses were reported in DTN: MO0005PORWATER.000 [150930]. The average of two of these analyses with the closest compositions (HD-PERM-2 and HD-PERM-3, Table 4.1-3) was initially chosen as the input water composition for pre-REV02 work and referenced hereafter as the Alcove 5 or HD-PERM water (see Section 6.2.2.1).

More recently, as part of REV02 work, a series of pore-water samples were ultracentrifuged from core collected in the Enhanced Characterization of Repository Block (ECRB) Cross Drift and from core obtained from the drilling of borehole SD-9. These samples were analyzed and the data were reported under DTN: GS020408312272.003 [160899]. Four of these samples (ECRB-SYS-CS7.3-7.7/UC, ECRB-SYS-CS2000/16.5-21.1/UC, SD-9/990.4-991.7/UC, and ECRB-SYS-CS500/12.0-16.7/UC) and HD-PERM water were selected as input water compositions for REV02 of the THC Seepage Model (Table 4.1-3). The rationale for selecting these samples and the determination of concentrations for constituents that were not measured are discussed in Section 6.2.2.1.

Table 4.1-3. Input Pore-Water Compositions

Sample ID →		ESF-HD-PERM-2 (30.1'-30.5')[1] (ESF Alcove 5)	ESF-HD-PERM-3 (34.8'-35.1')[1] (ESF Alcove 5)	ECRB-SYS-CS1000/7.3-7.7/UC[2]	ECRB-SYS-CS2000/16.5-21.1/UC[2]	SD-9/990.4-991.7/UC[2]	ECRB-SYS-CS500/12.0-16.7/UC[2]
Lithostratigraphic Unit →		Tptpmn	Tptpmn	Tptpul (base)	Tptpll	Tptpll	Tptpul
	Units						
pH (measured)	pH	8.32	8.31	7.6	7.4	7.9	8.0
Na^{+}	mg/L	61	62	39	130	84	57
K^{+}	mg/L	7	9	7.6	10.6	7.9	10.3
Ca^{+2}	mg/L	106	97	94	82	56	120
Mg^{+2}	mg/L	16.6	17.4	18.1	5.3	0.9	19.3
SiO_2	mg/L	31 (as Si)	35 (as Si)	42	48	50	49
Cl^{-}	mg/L	110	123	21	26	23	54
SO_4^{-2}	mg/L	111	120	36	39	10	78
HCO_3^{-} (measured)	mg/L	-	-	333	382	313	286
NO_3^{-}	mg/L	3	10	2.6	4.2	17	6.1
F^{-}	mg/L	0.96	0.76	3.4	11	2.5	4.8

NOTES: (1) Pore water analyses from Alcove 5 (Tptpmn) reported with DTN: MO0005PORWATER.000 [150930]. The sample ID corresponds to the ESF borehole ID and is followed by the sampling depth in feet from collar.
(2) Pore water analyses from the ECRB cross-drift and borehole SD-9 reported in DTN: GS020408312272.003 [160899]. Note, for ECRB samples, the sample ID contains the cross-drift station in meters (e.g., CS1000) and the sampled interval in feet from collar (e.g., 7.3-7.7). The ID of the SD-9 sample contains the sampled depth interval in feet from the ground surface.

4.1.4 Thermodynamic Data

These data consist mostly of chemical equilibrium constants in logarithmic form, log(K), as function of temperature (not to be confused with thermal conductivity, often described also using the letter K), for reactions describing the dissociation of secondary aqueous species, minerals, and gases involved in the model (e.g., Section 6.4.1). Molecular weight and diameter, molar volume, and ion size data for the calculation of aqueous activity coefficients are also included in the thermodynamic data sets. Kinetic rate constants k (always in lower case), are provided in separate databases discussed in Sections 4.1.5 (also see Sections 6.4.2 and 6.4.8) and are also not to be confused with equilibrium constants K.

Thermodynamic data for REV02 simulations (reported in Section 6.8) were taken from DTN: LB0307THMDBRTM.001 [164434]. For convenience, this data set is shown in Attachment VI (zeolite phases used are those identified in Attachment VI with names "heul/10-r02," "stell/10-r02," "mord/10-r02," and "clpt/10-r02," except for alternative data sets as discussed in Section 6.4.8.2). Most of these data are originally from the Yucca Mountain Project (YMP) thermodynamic database data0.ymp.R2 (DTN: MO0302SPATHDYN.000 [161756]). Documentation on changes from the data0.ymp.R2. database is provided in DTN: LB0307THMDBDRTM.001 [164434]. Most important changes from data0.ymp.R2 include:

- Aluminum aqueous species data consistent with thermodynamic data used in earlier revisions of this report. These aluminum data were derived from Pokrovskii and Helgeson (1995 [101699]). In the weakly-acid-to-alkaline pH values covered in this study, and at temperatures below 150°C, the Pokrovskii and Helgeson (1995 [101699]) data yield essentially the same gibbsite solubility as the data currently in data0.ymp.R2 (DTN: MO0302SPATHDYN.000 [161756]), and essentially the same pK values for the protonation of the AlO_2^- (or $Al(OH)_4^-$) to $HAlO_2$ (or $Al(OH)_3$).

- Revised aqueous silica thermodynamic properties yielding solubility constants (log(K)) values very similar to those reported by Rimstidt (1997 [101709]) for quartz and Gunnarsson and Arnórsson (2000 [160465]) for amorphous silica. These data are also consistent with thermodynamic data used in earlier revisions of this report, and provide more accurate amorphous silica solubilities than the data0.ymp.R2 data.

- Solubility constants for albite and anorthite from Arnórsson and Stefánsson (1999 [153329], p. 173). These data are consistent with those used in earlier versions of this report and with the aqueous silica data used here.

- Solubility constants for K-feldspar adjusted to yield equilibration of the HD-PERM pore water (Table 6.2-1) with illite (below) and K-feldspar. This adjustment results in a Gibbs free energy value for this phase at 25°C within the range of literature data reported by Arnórsson and Stefánsson 1999 [153329] (their Table 1) and within 700 calories of the value reported by Robie et al. (1979 [107109]). Without this adjustment, calculated potassium concentrations in pore waters are too small.

- Revised clay (smectite and illite) data consistent with those used in earlier versions of this report. The revisions include log(K) values for illite derived from accurate solubility

measurements by Kulik and Aja (1997 [128132]), and log(K) values for smectites adjusted to yield equilibration as an ideal solid solution at 25°C with the HD-PERM pore water (Table 6.2-1). The latter adjustment required less than 0.5% change in the Gibbs free-energy values of these smectites, well within the uncertainty of these values. Without this revision, the calculated pH of pore waters through time, under ambient conditions (no thermal load), becomes unrealistically elevated (Section 6.8.5.1).

- Revised zeolite (stellerite, heulandite, mordenite, and clinoptilolite) data for consistency with new stellerite data reported by Fridriksson et al. (2001 [160460]). Without this revision, an unrealistic calcium depletion is predicted to occur in pore waters under ambient conditions (no thermal load), due to the precipitation of large amounts of calcium zeolites (Section 6.8.5.1)

Of these changes, the last two have the most significant effect on simulation results compared to results obtained using the project database data0.ymp.R2 (DTN: MO0302SPATHDYN.000 [161756]) (Section 6.8.5.1). The stellerite thermodynamic data in data0.ymp.R2 reflect a significantly higher stability for this mineral than the new data from Fridriksson et al. (2001 [160460]) suggest. The clay data in data0.ymp.R2 also reflect a greater stability than the revised data used here. More details on all changes from the data0.ymp.R2. database are provided in the documentation accompanying the data filed under DTN: LB0307THMBDRTM.001 [164434].

Ambient simulations (Section 6.8.5.1) were conducted using alternative data sets including the data0.ymp.R2 database. These ambient simulations were run to provide a justification for the use of data from DTN: LB0307THMDBRTM.001 [164434] (which include the changes described above). Sources of data for the alternative data sets are presented in Section 6.4.8.2.

4.1.5 Kinetic Data

Kinetic data refer to the reaction rate constants (k_o), activation energies (E_a), and related data required to describe the rates of dissolution and precipitation of minerals as a function of temperatures and fluid chemistry.

Reaction rate laws can take numerous forms, of which a restricted number are used for the model analyses. The form of these rate laws and their significance are described in Section 6.4.2. Listed kinetic parameters are defined and used in Equations 6.4-5 through 6.4-8.

REV02 simulations were conducted using the kinetic data from DTN: LB0307KNTDBRTM.001 [164433]. For convenience, these data are shown in Table 4.1-4. These data were used in the absence of other existing qualified kinetic data.

Table 4.1-4. REV02 Kinetic Data

MINERAL	k_{+r} (mol m^{-2} s^{-1})[1] at 298.15 K	E_a (kJ/mol)[2]	m[3]	n[3]	Comment [4]
α-Cristobalite SiO_2	3.45×10^{-13}	68.9	1	1	dissolution only
Quartz SiO_2	4.52×10^{-14}	90.1	1	1	dissolution only
Tridymite SiO_2	3.45×10^{-13}	68.9	1	1	dissolution only
Amorphous silica SiO_2	7.32×10^{-13}	60.9	1	1	dissolution
	1.0×10^{-10}	50	4.4	1	precipitation
Opal-proxy SiO_2	7.32×10^{-13}	60.9	1	1	dissolution only
Microcline = K-spar $KAlSi_3O_8$	1.78×10^{-13}	36	1	1	reversible
Albite-low $NaAlSi_3O_8$	7.08×10^{-13}	67.7	1	1	reversible
Anorthite $CaAl_2Si_2O_8$	3.16×10^{-12}	67.7	1	1	dissolution only
Illite $K_{0.5}(Mg_{0.22}Al_{1.78})(Si_{3.72}Al_{0.28})O_{10}(OH)_2$	2.0×10^{-14}	58.6	1	1	reversible
Smectite-Ca $Ca_{0.145}(Mg_{0.26}Al_{1.74})(Si_{3.97}Al_{0.03})O_{10}(OH)_2$	2.0×10^{-14}	58.6	1	1	reversible
Smectite-Mg $(Mg_{0.405}Al_{1.74})(Si_{3.97}Al_{0.03})O_{10}(OH)_2$	2.0×10^{-14}	58.6	1	1	reversible
Smectite-Na $Na_{0.29}(Mg_{0.26}Al_{1.74})(Si_{3.97}Al_{0.03})O_{10}(OH)_2$	2.0×10^{-14}	58.6	1	1	reversible
Sepiolite $Mg_2Si_3O_{7.5}OH \cdot 3H_2O$	2.67×10^{-14}	58.6	1	1	reversible

Table 4.1-4. REV02 Kinetic Data (continued)

MINERAL	k_{+r} (mol m^{-2} s^{-1})[1] at 298.15 K	E_a (kJ/mol)[2]	m[3]	n[3]	Comment [4]
Kaolinite $Al_2Si_2O_5(OH)_4$	1.0×10^{-13}	7.1 (± 2.5)	1	1	reversible
Heulandite $Ca_{0.33}K_{0.04}Na_{0.1}(Al_{0.9}Si_{2.8}O_{7.2}) \cdot 2.6H_2O$	5.66×10^{-13}	58.0	1	1	dissolution
Clinoptilolite $Ca_{0.26}K_{0.08}Na_{0.04}(Al_{0.68}Si_{2.92}O_{7.2}) \cdot 2.6H_2O$	2.37×10^{-13}	58.0	1	1	reversible
Stellerite $Ca_{0.39}Na_{0.01}(Al_{0.79}Si_{2.81}O_{7.2}) \cdot 2.8H_2O$	5.66×10^{-13}	58.0	1	1	reversible
Mordenite $Ca_{0.15}Na_{0.21}K_{0.09}(Al_{0.6}Si_3O_{7.2}) \cdot 2.2H_2O$	5.66×10^{-13}	58.0	1	1	reversible
Calcite	1.60×10^{-6}	48.1	1	1	reversible
$CaCO_3$	equilibrium	NA	NA	NA	local equilibrium
Gypsum $CaSO_4 \cdot 2H_2O$	equilibrium	NA	NA	NA	local equilibrium
Fluorite CaF_2	1.22×10^{-7}	0.0	1	2	reversible
Hematite Fe_2O_3	equilibrium	NA	NA	NA	local equilibrium
Goethite FeOOH	equilibrium	NA	NA	NA	local equilibrium
Glass (vitrophyre)	7.72×10^{-15}	91.0	1	1	dissolution only

DTN: LB0307KNTDBRTM.001 [164433]

NOTES: (1) k_{+r}: dissolution/precipitation rate constants at 298.15 K.

(2) E_a: Activation energy.

(3) Exponents m and n in Equations 6.4-5, 6.4-7, and 6.4-8.

(4) "dissolution only" means precipitation of this mineral is not allowed, "reversible" indicates the same precipitation and dissolution rate apply.

4.1.6 Transport Parameters

Transport parameters considered in the model are diffusion coefficients for aqueous and gaseous species and tortuosities of the fracture, matrix, and engineered system components.

Diffusion coefficients for all aqueous species are direct inputs to the model and entered as the tracer diffusion coefficient of the chloride anion (Cl) at infinite dilution. The aqueous diffusion coefficient of Cl at infinite dilution is 2.03×10^{-9} m^2/s at 25°C (Lasaga 1998 [117091], Table 4.1, p. 315), which in the model input was rounded to 2.0×10^{-9} m^2/s. The value of 2.03×10^{-9} m^2/s is corroborated by Lide (1993 [123032], p. 5-111). The rationale for using these data sources is that they are accepted throughout the scientific community as reliable references.

The CO_2 diffusion coefficient is approximated from ideal gas behavior as described in Section 6.4.6.1, using direct inputs for molecular diameter (d_m) and molecular weight (M) as follows (unless specified otherwise in Section 6):

$d_m = 2.5 \times 10^{-10}$ m (DTN: LB0307THMDBRTM.001 [164434])

$M = .04401$ kg/mol (DTN: MO0302SPATHDYN.000 [161756])

Tortuosities were set to 0.7 for fractures (DTN: LB991091233129.006 [111480]) based on models of *in situ* testing data, and further modified as described in Section 6.4.6.1. Matrix tortuosities are unknown and assumed in Section 5, with rationale given in that section.

4.1.7 Design Information

Design information are specified, in contrast to data resulting from measurements. Design information are not "data" and are presented in this section for convenience because they are required for model input. Sources of design information are summarized in Table 4.1-2.

Two time periods are considered in the THC Seepage Model:

- A 50-year preclosure period during which a large amount of the heat released by the waste packages is removed by ventilation (see below)
- A postclosure period immediately following the initial 50-year preclosure period and extending to 100,000 years (the total simulation time), during which a drip shield is placed above the waste packages and no heat is removed by ventilation.

Accordingly, some of the drift-specific model-input design information are not the same for the preclosure and postclosure time periods. The model drift geometry and thermophysical properties of design elements are shown in Table 4.1-5 and Figure 4.1-1. Sources of this technical information are shown in this table and also referenced in Table 4.1-2. This drift design information is the same as that used for Site Recommendation. However, an important difference from previous model revisions is that the drift is modeled here as open to both advective and diffusive fluxes of liquid and gas. As a result, hydrological properties had to be assigned to open in-drift areas. These properties are included in Table 4.1-5. The discretization of the drift is consistent with the dimensions shown in Figure 4.1-1, within the limits imposed by the resolution of the model mesh.

Table 4.1-5. Drift Design Parameters

Parameter	Model Input		Information Exchange Drawing (IED)[1]	
	Source	Value	Current Value	Source
Drift diameter	800-IED-EBS0-00201-000-00A (BSC 2003 [164069])	5.5 m	5.5 m	800-IED-EBS0-00201-000-00A (BSC 2003 [164069])
Waste package outer diameter	800-IED-WIS0-00201-000-00A (BSC 2002 [164053]) (44-BWR waste package)	1.67 m (rounded off from 1.674 m)	1.318 – 2.110 m (1.674 m for 44-BWR waste package)	800-IED-WIS0-00201-000-00A (BSC 2002 [164053])
Top of invert as measured from bottom of drift	800-IED-WIS0-00301-000-00A (BSC 2003 [164052])	0.8 m (rounded off from 0.806 m)	0.806 m	800-IED-WIS0-00301-000-00A (BSC 2003 [164052])
Location of waste package center above bottom of drift	CRWMS M&O (2000 [151014], Table 2)	1.945 m	1.637 – 2.088 m	800-IED-EBS0-00201-000-00A (BSC 2003 [164069]) (center line of waste package height above invert) and 800-IED-WIS0-00301-000-00A (BSC 2003 [164052]) (invert thickness)
Location of waste package center below the drift springline	CRWMS M&O (2000 [151014], Table 2)	0.805 m	0.662 – 1.113 m	800-IED-EBS0-00201-000-00A (BSC 2003 [164069]) (drift diameter; center line of waste package height above invert) and 800-IED-WIS0-00301-000-00A (BSC 2003 [164052]) (invert thickness)
Drip shield thickness	CRWMS M&O (2000 [151014], Table 2)	0.02 m	0.015 m	000-MW0-TED0-00102-000-00A (BSC 2003 [161519]
Air gap between waste package surface and the inside of drip shield	CRWMS M&O (2000 [151014], Table 2)	0.396 m	0.079 – 0.920 m	800-IED-EBS0-00201-000-00A (BSC 2003 [164069]) (center line of waste package height above invert), 800-IED-WIS0-00201-000-00A (BSC 2002 [164053]) (diameter of waste package), and 000-MW0-TED0-00102-000-00A (BSC 2002 [161519] (inside height of drip shield)
Inside radius of drip shield	CRWMS M&O (2000 [151014], Table 2)	1.231 m	1.350 m	000-MW0-TED0-00102-000-00A (BSC 2002 [161519]
Waste package thermal conductivity	CRWMS M&O (2000 [151014], Table 2)	14.42 W/m K	Not in an IED	Not Applicable
Waste package density	CRWMS M&O (2000 [151014], Table 2)	8189.2 kg/m^3	Not in an IED	Not Applicable

Table 4.1-5. Drift Design Parameters (continued)

Parameter	Model Input		Information Exchange Drawing (IED)[1]	
	Source	Value	Current Value	Source
Waste package specific heat	CRWMS M&O (2000 [151014], Table 2)	488.86 J/kg K	Not in an IED	Not Applicable
Invert intrinsic permeability	CRWMS M&O (2000 [151014], Table 2)	6.152×10^{-10} m^2	Not in an IED	Not Applicable
Invert porosity	CRWMS M&O (2000 [151014], Table 2)	0.545	Not in an IED	Not Applicable
Invert grain density	CRWMS M&O (2000 [151014], Table 2)	2530 kg/m^3	Not in an IED	Not Applicable
Invert specific heat	CRWMS M&O (2000 [151014], Table 2)	948 J/kg K	Not in an IED	Not Applicable
Invert thermal conductivity (upper invert)	BSC 2002 [159906], Table 6-48 (100°C data, average between ballast K = 0.1 and 0.2 W/m-K)	1.52 W/m K	Not in an IED	Not Applicable
Invert thermal conductivity (lower invert)	CRWMS M&O 2000 [149137], Design Criterion, p. 23	0.15 W/m K (average measurement on two samples)	Not in an IED	Not Applicable
Open areas (linear capillary pressure and relative permeability functions)	Model setup (Section 6.4.6)		Not in an IED	Not Applicable
Permeability		1×10^{-10} m^2		
Residual saturation (drift wall / all other areas)		0.01 / 0.0		
Porosity		1.0		
Capillary pressure		0.0 Pa		
Invert capillarity (linear capillary pressure function)	Set equal to 1/(Van Genuchten alpha), with alpha = 1.2×10^{-3} Pa^{-1} (rounded off from value in CRWMS M&O 2000 [151014], Table 2)	833 Pa	Not in an IED	Not Applicable
Invert residual saturation	Rounded off from value in CRWMS M&O (2000 [151014], Table 2)	0.1	Not in an IED	Not Applicable

Source: [1] IEDs were not always used because many IEDs were not completed before the start of this study. Differences between values used and those in IEDs are not expected to significantly affect model results for locations in rock around the drift because these results are primarily dependent on the applied heat load and not on the specifics of in-drift engineered features.

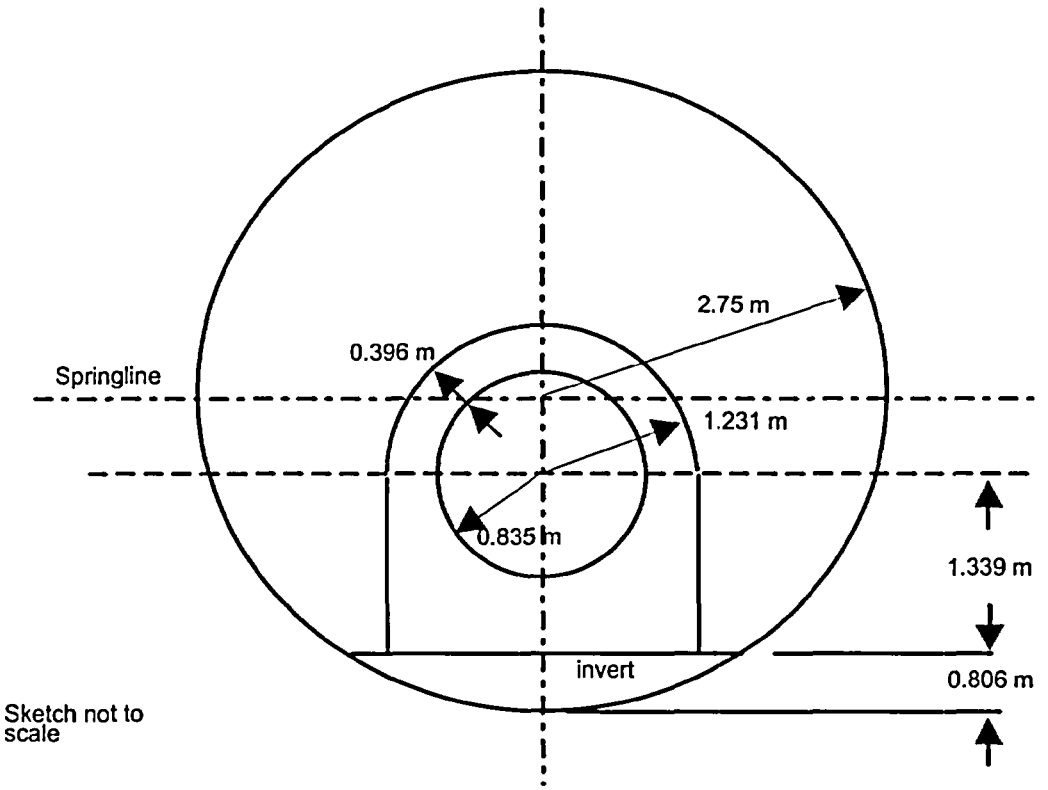

Source: Table 4.1-5

Figure 4.1-1. Sketch Showing Modeled In-Drift Dimensions

The drip shield was not explicitly modeled, but its thickness and thermal conductivity were considered in the width and thermal properties, respectively, of the open zone between the waste package and drip shield during the postclosure period.

The total (unventilated) heat load in REV02 simulations was obtained from BSC (2002 [159527]) (Attachment VIII). The initial heat transfer from the waste package is 1.45 $kW/m_{(drift)}$ which decays after 50 years to 0.593 kW/m and to 0.0684 W/m after 1,000 years. This is essentially the same heat load as shown in BSC 2003 [161731] which superseded BSC 2002 [159527], and also is very similar to the REV01 heat load. The heat removal rate during the 50-year preclosure period is 86.3% (BSC 2002 [160975], Table 6-6), which is significantly larger than the 70% used in REV01.

Heat transfer from the waste package to the drift wall is implemented in the model by using time-varying "effective" thermal conductivities (for open spaces within the drift) that were calculated to account for radiative and convective heat transport. These time-varying variables were input into the model as coefficients (values between 0 and 1) for each open zone within the drift. Each zone was also assigned a constant maximum thermal conductivity (Kth_{max}), which was then multiplied by the corresponding time-varying coefficients to obtain effective conductivities as a function of time (Attachment IX). The sources of this design information are listed in Table 4.1-2.

The effective thermal conductivities and corresponding open zones of the drift prior to closure are not the same as those following closure. Only one open space between the waste package and the drift wall is considered for the preclosure period. For postclosure, two zones are considered: (1) the open space between the waste package and the drip shield (Inner Zone, drip shield included) and (2) the open space between the drip shield and the drift wall (Outer Zone) (Figure 4.1-1). For preclosure, Kth_{max} = 10.568 W/m-K for the zone between the waste package and the drift wall. For postclosure, Kth_{max} = 2.298 W/m-K for the Inner Zone (between the waste package and the drip shield), and Kth_{max} = 14.407 W/m-K for the Outer Zone (between the drip shield and the drift wall). The sources of this design information are listed in Table 4.1-2. Accordingly, model runs were started with the preclosure thermal conductivities, then stopped after 50 years and restarted with the corresponding postclosure data.

The invert is divided into two zones with different thermal conductivities: 1.52 W/m-K for the upper half and 0.15 W/m-K for the lower half (Table 4.1-4).

The implementation of the drift design in the model is further documented in Spycher (2001 [160898], pp. 11–14; 116–129).

4.2 CRITERIA

Technical requirements to be satisfied by performance assessment (PA) are based on 10 CFR 63.114 [156605] (*Requirements for Performance Assessment*). These technical requirements are also identified in the Yucca Mountain *Project Requirements Document* (Canori and Leitner 2003 [161770], Section 3). The acceptance criteria that will be used by the Nuclear Regulatory Commission (NRC) to determine whether the technical requirements have been met are identified in the *Yucca Mountain Review Plan, Final Report* (YMRP; NRC 2003 [163274]). The pertinent requirements and acceptance criteria for this Model Report are summarized in Table 4.2-1. Note that different Acceptance Criteria were identified in the TWP (BSC 2002 [160819], Section 3) because the YMRP has been revised since completion of the TWP.

Table 4.2-1. Project Requirements and YMRP Acceptance Criteria Applicable to This Model Report

Requirement Number[a]	Requirement Title[a]	10 CFR 63 Link	YMRP Acceptance Criteria
PRD-002/T-015	Requirements for Performance Assessment	10 CFR 63.114(a-c) [156605]	Criteria 1 to 4 for *Quantity and Chemistry of Water Contacting Engineered Barriers and Waste Forms* [b]
PRD-002/T-016	Requirements for Multiple Barriers	10 CFR 63.115(c) [156605]	Criterion 3 for *Quantity and Chemistry of Water Contacting Engineered Barriers and Waste Forms* [c]

NOTES: [a] from Canori and Leitner (2003 [161770], Section 3)
[b] from NRC (2003 [163274], Section 2.2.1.3.3.3)
[c] from NRC (2003 [163274], Section 2.2.1.1.3)

The acceptance criteria identified in Section 2.2.1.3.3.3 of the YMRP (NRC 2003 [163274]) are given below, followed by a short description of their applicability to this Model Report:

- Acceptance Criterion 1, *System Description and Model Integration are Adequate*:

  The applicable subcriteria are:

  Subcriterion 1. This subcriterion requires that the total system performance assessment adequately incorporates important design features, physical phenomena, and couplings, and uses consistent and appropriate assumptions throughout the quantity and chemistry of water contacting waste packages and waste forms abstraction process. This subcriterion is addressed in Sections 6.2, 6.3, and 6.4.

  Subcriterion 2. This subcriterion requires that the abstraction of the quantity and chemistry of water contacting waste packages and waste forms uses assumptions, technical bases, data and models, that are appropriate and consistent with other related U.S. Department of Energy abstractions. Sections 5, 6, and 7 address this subcriterion regarding water chemistry.

  Subcriterion 4. This subcriterion requires that spatial and temporal abstractions appropriately address physical couplings (thermal-hydrologic-mechanical-chemical). Sections 6.8.5.3 and 6.8.5.4 address this subcriterion.

  Subcriterion 5. This subcriterion requires that sufficient technical bases and justification are provided for total system performance assessment assumptions and approximations for modeling coupled thermal-hydrologic-mechanical-chemical effects on seepage and flow, the waste package chemical environment, and the chemical environment for radionuclide release. This subcriterion also requires that the effects of distribution of flow on the amount of water contacting the waste packages and waste forms are consistently addressed, in all relevant abstractions. This report addresses coupled THC effects on water chemistry and flow in the UZ up to the drift wall (Section 6). It therefore addresses parts of this subcriterion.

  Subcriterion 8. This subcriterion requires that adequate technical bases are provided, including activities such as independent modeling, laboratory or field data, or sensitivity studies, for inclusion of any thermal-hydrologic-mechanical-chemical couplings and features, events, and processes (FEPs). FEPs are addressed in Section 6.1, technical bases in Sections 6.2–6.4, modeling and sensitivity studies in Sections 6.5–6.8, and modeling of field and laboratory experiments in Section 7.0, thus addressing this subcriterion.

  Subcriterion 9. This subcriterion requires that performance-affecting processes that have been observed in thermal-hydrologic tests and experiments are included into the performance assessment. Simulations presented in this report reproduce coupled THC effects observed in thermal test (Section 7.1) and laboratory experiments (Sections 7.2 and 7.3), and therefore address this subcriterion.

Subcriteria 3, 6, 7, 10, 11, and 12 are not applicable.

- Acceptance Criterion 2, *Data Are Sufficient for Model Justification*:

  The applicable subcriteria are:

  Subcriterion 1. This subcriterion requires that geological, hydrological and geochemical values used in the safety case are adequately justified, and that adequate descriptions of how data were used, interpreted, and appropriately synthesized into the parameters are provided. This subcriterion is addressed in Section 4.1, 6.2 (and in particular 6.2.2), 6.3, and 6.4.

  Subcriterion 2. This subcriterion requires that sufficient data were collected on the characteristics of the natural system and engineered materials to establish initial and boundary conditions for conceptual models of thermal-hydrologic-chemical coupled processes that affect seepage and flow and the waste package chemical environment. This report addresses parts of this subcriterion by considering variations in pore-water compositions (Section 6.2.2 and 6.8.5) and rock properties (Sections 6.5–6.8) representative of the natural system.

  Subcriterion 3. This subcriterion requires that thermo-hydrologic tests were designed and conducted with the explicit objectives of observing thermal-hydrologic processes for the temperature ranges expected for repository conditions and making measurements for mathematical models. This subcriteria also requires that data are sufficient to verify that thermal-hydrologic conceptual models address important thermal-hydrologic phenomena. Section 7.1, which presents details on results of the Drift Scale Test and simulations reproducing results of this test, addresses this subcriteria.

  Subcriteria 4 and 5 are not applicable.

- Acceptance Criterion 3, *Data Uncertainty Is Characterized and Propagated Through the Model Abstraction*

  Subcriterion 1. This subcriterion requires that models use parameter values, assumed ranges, probability distributions, and/or bounding assumptions that are technically defensible and reasonably account for uncertainties and variabilities. In this report, this subcriterion is addressed by using ranges if input data (e.g., pore-water composition, Section 6.2.2) and alternative conceptualizations of the modeled systems (Section 6.3) to model uncertainty is also discussed in Section 6.9.

  Subcriterion 2. This subcriterion requires that parameter values, assumed ranges, probability distributions, and bounding assumptions used in the calculations of quantity and chemistry of water contacting waste packages and waste forms are technically defensible and reasonable, based on data from the Yucca Mountain region (i.e., DST), and a combination of techniques that include laboratory experiments and field measurements and process-level modeling studies. This report addresses the parts of this subcriterion that relate to the uncertainty of the chemistry of water that could potentially

enter drifts, with inputs and results discussed in Sections 6.2.2, 6.8.5, 6.9, and validation including the results of the DST and laboratory experiments presented in Section 7.

Subcriterion 3. This subcriterion requires that input values used in the total system performance assessment calculations of quantity and chemistry of water contacting engineered barriers (e.g., drip shield and waste package) are consistent with the initial and boundary conditions and the assumptions of the conceptual models and design concepts for the Yucca Mountain site. This criterion also requires that correlations between input values are appropriately established in the U.S. Department of Energy total system performance assessment; that parameters used to define initial conditions, boundary conditions, and computational domain in sensitivity analyses involving coupled thermal-hydrologic-mechanical-chemical effects on seepage and flow, the waste package chemical environment, and the chemical environment for radionuclide release, are consistent with available data; and that reasonable or conservative ranges of parameters or function relations are established. This subcriterion is addressed with respect to the chemistry of water that could potentially enter drifts, with the conceptual models described in Sections 6.3–6.4 initial and boundary conditions discussed in Sections 6.5.2, 6.7.2 and 6.8.2, and ranges of input parameters presented in Sections 6.5.3, 6.6.1, 6.7.3 and 6.8.3.

Subcriterion 4. This subcriterion requires that adequate representation of uncertainties in the characteristics of the natural system and engineered materials is provided in parameter development for conceptual models, process-level models, and alternative conceptual models. This subcriterion also states that the U.S. Department of Energy may constrain these uncertainties using sensitivity analyses or conservative limits. This subcriterion is addressed by considering ranges of input parameters and alternative conceptualizations (e.g., Table 6-1 and Sections 6.2.2 and 6.3), as well as evaluations of the spread of model results (Section 6.9).

Subcriterion 5 is not applicable.

- Acceptance Criterion 4, *Model Uncertainty Is Characterized and Propagated Through the Model Abstraction*:

  Subcriterion 1. This subcriterion requires that alternative modeling approaches of features, events, and processes (FEPs), consistent with available data and current scientific understanding, are investigated. This subcriterion also requires that the results and limitations are appropriately considered in the abstraction. This subcriterion is addressed by reviewing FEPs (Section 6.1), by using alternative conceptual models (Section 6.3), and evaluating model limitation and uncertainty (Sections 1.3, 6.9 and 8.4).

  Subcriterion 2. This subcriterion requires that alternative modeling approaches are considered and the selected modeling approach is consistent with available data and current scientific understanding, and the results and limitations and uncertainties of the chosen model are provided. This subcriterion is addressed by considering various model conceptualizations (Section 6.3), evaluating spread in model results (Section 6.8.5), and reporting on limitations and uncertainties (Section 1.3, 6.9 and 8.4).

Subcriterion 3. This subcriterion requires that consideration of conceptual model uncertainty is consistent with available site characterization data, laboratory experiments, field measurements, natural analog information and process-level modeling studies; and that the treatment of conceptual model uncertainty does not result in an under-representation of the risk estimate. This subcriterion is addressed by using site-specific data (Section 4.1) as well as data from field and laboratory experiments (Section 7), and considering ranges of key input parameters (e.g. Section 6.2.2), alternative conceptualizations (Section 6.3), and spread in model results (Section 6.9).

Subcriterion 4. This subcriterion requires that adequate consideration is given to effects of thermal-hydrologic-mechanical-chemical coupled processes in the assessment of alternative conceptual models. These effects may include: (i) thermal-hydrologic effects on gas, water, and mineral chemistry; (ii) effects of microbial processes on the waste package chemical environment for radionuclide release; (iii) changes in water chemistry that may result from the release of corrosion products from the waste package and interactions between engineered materials and ground water; and (iv) changes in boundary conditions (e.g., drift shape and size) and hydrologic properties, relating to the response of the geomechanical system to thermal loading. This report addresses part (i) of this subcriterion through conceptual and mathematical models described in Sections 6.2 and 6.4, and model results presented in Sections 6.5.5, 6.6.2, 6.7.5, and 6.8.5.

Subcriterion 5 is not applicable.

The acceptance criterion identified in Section 2.2.1.1.3 of the YMRP (NRC 2003 [163274]) is given below, followed by a short description of its applicability to this Model Report

- Acceptance Criterion 3, *Technical Basis for Barrier Capability is Adequately Presented*:

  This model report documents the drift-scale coupled THC processes model that provides input to downstream users to predict the chemistry of water potentially contacting waste packages and waste forms. The technical bases for this model are consistent with the technical basis for the performance assessment, including consideration of the natural barrier created by host rocks, and the capillary pressure barrier at the drift wall (Sections 6.8.1, 6.8.5.2, and 6.8.5.4). The effect of a potential barrier created by mineral precipitation around the drift is also evaluated (Section 6.8.5.4).

4.3 CODES AND STANDARDS

No specific formally established standards have been identified as applying to this modeling activity.

INTENTIONALLY LEFT BLANK

5. ASSUMPTIONS

Development of methodology for the numerical modeling of heat and fluid flow in unsaturated fractured porous media, the calculation of mineral-water reactions, and the transport of aqueous and gaseous species are discussed in Section 6. Many simplifications and approximations underlie this methodology. Yet other simplifications and approximations are inherent in data that describe repository designs and associated parameters on which model simulations rely. In this section, only cases in which an assumption is made where there is an absence of data or information for the parameter or concept are described. These are listed below. Approximations and simplifications related to the development and implementation of the mathematical model applied for this study are presented as part of the model documentation in Section 6.4.6.

- The estimated matrix tortuosity of 0.2 is assumed to be applicable to the tuff matrix at Yucca Mountain (see Section 4.1.6). Because this value is within a range of values that differ by less than one order of magnitude, and is a factor applied along with the porosity to the diffusion coefficient, the effect on reaction-transport processes of a deviation in this number from the true value would be small. Therefore, no further justification or confirmation is necessary. A tortuosity of 0.7 is assumed for the invert. These values only slightly affect diffusive transport of CO_2 in the drift. The tortuosity of sand is about 0.7 (de Marsily 1986 [100439], p. 233), and because the invert is coarse granular material, its tortuosity would be expected to be between 0.7 and 1.0. Because reactions involving CO_2 are minimal in the drift, the diffusivity of CO_2 within in-drift components has a negligible effect on THC processes outside of the drift. Therefore, this assumption needs no further justification or confirmation.

INTENTIONALLY LEFT BLANK

6. MODEL DISCUSSION

This section presents the conceptual and mathematical models implemented for the development of the Drift Scale THC Seepage Model. Relevant features, events, and processes are also briefly discussed in Section 6.1. Details on the conceptualization and the mathematical treatment of the various coupled processes considered in the THC Seepage Model follow in Sections 6.2 through 6.4. The results of the THC Seepage Model are presented in Sections 6.5 through 6.8. In these sections, coupled THC processes are evaluated for 100,000 years under boundary conditions that are varied to represent the effects of potential climatic change, two repository host units, various input water compositions, and other alternative model conceptualizations. The validation of the THC Seepage Model is presented in Section 7. The model validation consists of simulating the water, gas, and mineral evolution in the Drift Scale Test using the DST THC Model (Section 7.1) and laboratory water-rock interaction experiments (Sections 7.2 and 7.3). The laboratory experiments are used to compare simulated and measured water compositions evolved during interaction with crushed tuff and mineral precipitation patterns in a fracture where boiling and reflux are taking place. These validation simulations rely on the same conceptualizations and mathematical formulations presented in this section.

The development of the THC Seepage Model is summarized in Table 6-1, which include changes between model revisions and a summary of the various conceptualizations and sensitivities considered.

Table 6-1. Summary of Changes from the REV01 to the REV02 THC Seepage Model

	Tptpmn THC Model REV01	Tptpmn THC Heterogeneous Model REV01	Tptpll THC Model REV01	Tptpll THC Model REV02 (Current Model Report Revision)
Chronological order of model development	1	2	3	4
Main use of model	Compare with the Tptpll Model (REV01) to evaluate the effect of host hydrogeologic unit and stratigraphic location	Compare with the Homogenous Tptpmn Model (REV01) to evaluate the effect of fracture permeability heterogeneity	Compare with the Tptpmn model (REV01) to evaluate the effect of host hydrogeologic unit and stratigraphic location	Evaluate the effect of model improvements comparisons with the Tptpmn Model (REV01) and provides sensitivities to various data and conceptualizations as shown
TOUGHREACT version	2.3	2.3	2.3	3
Model dimensions: Thermal loading Ambient conditions (baseline)	 2-D 2-D (with drift)	 2-D 2-D (with drift)	 2-D 2-D (with drift)	 2-D 1-D (no drift)
Stratigraphic column location	SD-9	SD-9	Center of repository	Center of repository
Host lithostratigraphic unit	Tptpmn	Tptpmn	Tptpll	Tptpll

Table 6-1. Summary of Changes between the REV01 and REV02 THC Seepage Model (Continued)

	Tptpmn THC Model REV01	Tptpmn THC Heterogeneous Model REV01	Tptpll THC Model REV01	Tptpll THC Model REV02 (Current Model Report Revision)
Heterogeneous permeability	No	Yes	No	No
Geochemical system (Table 6.2-2)	Base Extended	Base Extended	Base Extended	Extended
Input pore water composition (Table 6.2-1)	ESF Alcove 5	ESF Alcove 5	ESF Alcove 5	ESF Alcove 5 ECRB, 500 m (sensitivity) ECRB, 1000 m (sensitivity) ECRB, 2000 m (sensitivity) SD-9, 990 ft (sensitivity)
Infiltration rates (mm/yr)	Stepped up 6, 16, 25	Stepped up 6, 16, 25	Stepped up 6, 16, 25	Stepped up 6, 16, 25 Constant 6 (sensitivity) Constant 25 (sensitivity)
Heat Load (kW/m) (Attachments VII and VIII)	1.45	1.45	1.45	1.45
Ventilation Period (yr)	50	50	50	50
Ventilation efficiency (% heat removal)	70	70	70	86.3
Drift wall conceptualization	Closed to advective fluid flow	Closed to advective fluid flow	Closed to advective fluid flow	Open
Invert thickness	0.6	0.6	0.8	0.8
Vapor-pressure lowering due to capillary pressure	No	No	No	Yes No (sensitivity)
CO_2 diffusion coefficient change	None	None	None	Six-fold increase No change (sensitivity)
Improved treatment of mineral precipitation at boiling front	No	No	No	Yes
Chronological changes in Mineralogy (see Table 6.2-2 and Attachments I and II)	Initial data	No change	Added fluorite and opal as primary minerals in host rock	Added sepiolite and removed goethite as possible secondary minerals
Main chronological changes in thermal properties (see Table 6.4-1)	Initial data	No change	In Tptpll versus Tptpmn: 23 and 13 % decrease in effective K_{dry} and K_{wet}, respectively	For Tptpll, 6% increase in K_{dry} and 6% decrease in K_{wet} (effective values)
Main chronological changes in hydrological properties (see Table 6.4-1)	Initial data	In Tptpmn fractures: heterogeneous, 4-order-of- magnitude spread in fracture permeabilities in Tptpmn (3 different realizations)	In Tptpll versus Tptpmn fractures: six times higher permeability, 80% increase in porosity, and six times higher capillarity (1/alpha)	In Tptpll fractures: 62% decrease in permeability, 47% decrease in porosity and 20% decrease in capillarity (1/alpha)

NOTE: Sources of model input data and technical information shown here are discussed in Section 4.

Results of earlier investigations (REV01) are presented in Sections 6.5 (Tptpmn THC Model REV01), 6.6 (Tptpmn THC Heterogeneous Model REV01), and 6.7 (Tptpll THC Model REV01). Many model revisions have been implemented since the completion of this earlier work. These revisions include updated model input parameters, a change in the drift wall conceptualization (open versus closed), and a more accurate treatment of mineral precipitation at the boiling front (Section 6.4.5). Results of simulations including these revisions are presented in Section 6.8, together with model results for various input water compositions, infiltration rates, and two boiling/evaporation conceptual models, (including/excluding vapor-pressure lowering caused by capillary pressure). Simulations of ambient conditions using various sources of thermodynamic data are also presented in Section 6.8 as a means of justifying the thermodynamic data (Section 4) used in the model.

REV01 simulations are included in this Model Report revision because they provide an important assessment of the sensitivity of model results to the drift geologic host unit (Tptpmn versus Tptpll) and fracture permeability heterogeneity. However, the significant model revisions between REV01 and REV02 hamper pinpointing direct cause-effect relationships between a given specific change between REV01 and REV02 and its effect on simulation results. For these reasons, the REV01 results are best regarded as a qualitative assessment of model sensitivity to drift location and fracture permeability heterogeneity. For predictive evaluations, preference should be given to the most recent results, keeping in mind that the model uncertainty encompasses the results of both earlier and recent work. REV01 results indicate that the effect of drift location and fracture heterogeneity on predicted water chemistry and mineral alteration may not be as significant as the effect of uncertainties in input water composition, thermodynamic data, and infiltration rates. Therefore, evaluating the latter uncertainties is given priority in this Model Report revision.

The model development, data, and results are documented in the scientific notebooks (SNs) listed in Table 6-2 below. The intended use of output data from this Model Report is discussed in Section 1.1. Applicable acceptance criteria from the YMRP were discussed in Section 4.2, with pointers referring to sections addressing these criteria. The barrier capability of the host rocks, the capillary barrier at the drift wall, and potential barrier resulting from mineral precipitation around the drift are given consideration in this report (e.g., Sections 6.8.2, 6.8.5.2, and 6.8.5.4).

Table 6-2. Scientific Notebooks

LBNL Scientific Notebook ID	M&O Scientific Notebook ID	Relevant Pages	Citation
YMP-LBNL-YWT-ELS-1	SN-LBNL-SCI-109-V1	35–70, 87–91, 120–179	Wang 2003 [161665]
YMP-LBNL-DSM-ELS-1	SN-LBNL-SCI-142-V1	3–20, 27–52, 87–96, 104–115	Wang 2003 [161665]
YMP-LBNL-DSM-NS-1	SN-LBNL-SCI-141-V1	1–143	Spycher 2001 [160898]
YMP-LBNL-YWT-NS-1.2	SN-LBNL-SCI-112-V2	13–14, 21–40, 60–66	Wang 2003 [161665]
YMP-LBNL-DSM-ELS-PD-1	SN-LBNL-SCI-190-V1	7–60, 66–70, 86–144	Dobson 2001 [160252]
YMP-LBNL-GSB-1.6.4	SN-LBNL-SCI-085-V2	24–33	Haukwa 2001 [160900]
YMP-LBNL-DSM-NS-2	SN-LBNL-SCI-141-V2	94, 99-191	Wang 2003 [161665]
YMP-LBNL-DSM-ELS-PD-2	SN-LBNL-SCI-190-V2	7–35, 37–38, 43–81, 85, 95–124	Wang 2003 [161665]

6.1 RELEVANT FEATURES, EVENTS, AND PROCESSES

The results of this model abstraction are part of the basis for the treatment of Features, Events, and Processes (FEPs) as discussed in the *Total System Performance Assessment-License Application Methods and Approach* (BSC 2002 [160146], Section 3.2.2). FEPs that are included and excluded from TSPA-LA, and that are the subject matter of this report, are summarized in Tables 6.1-1 and 6.1-2, respectively. These were taken from the LA FEP List (MO0301SEPFEPS1.000 [161496]). The LA FEP List is a revision to the previous project FEP list (Freeze et al. 2001 [154365]) used to develop the list of included FEPs in the *Technical Work Plan for: Performance Assessment Unsaturated Zone* (BSC 2002 [160819], Table 2-6). The cross-reference for each FEP to the relevant section (or sections) in this Model Report is given in Tables 6.1-1 and 6.1-2.

Complete or partial treatment of FEPs is provided herein. The results of this and other model reports are used to fully document the technical basis for the include/exclude status of these FEPs for TSPA-LA. The UZ department's documentation for the included FEPs listed in Table 6.1-1 is compiled from this and other model reports and can be found in the model abstraction reports as described in Sections 2.1.2 and 2.4 of the TWP (BSC 2002 [160819]) and the FEPs report as described in Section 1.12.10 of the TWP (BSC 2002 [160819]). Excluded FEPs are to be documented in the FEPs report as described in Section 1.12.10 of the TWP (BSC 2002 [160819]).

Table 6.1-1. Features, Events, and Processes Relevant to this Model Report and Included into TSPA-LA

LA FEP Number	FEP Name	YMP Description	Sections Discussing FEPs-Related Items In this Model Report
1.1.02.02.0A	Pre-closure ventilation	The duration of pre-closure ventilation acts together with waste package spacing (as per design) to control the extent of the boiling front.	4.1.7
1.2.02.01.0A	Fractures	Groundwater flow in the Yucca Mountain region and transport of any released radionuclides may take place along fractures. The rate of flow and the extent of transport in fractures are influenced by characteristics such as orientation, aperture, asperity, fracture length, connectivity, and the nature of any linings or infills.	6.2.1 6.4.3
1.3.01.00.0A	Climate change, global	Climate change may affect the long-term performance of the repository. This includes the effects of long-term change in global climate (e.g., glacial/interglacial cycles) and shorter-term change in regional and local climate. Climate is typically characterized by temporal variations in precipitation and temperature.	6.2.1.3 6.5.2 6.7.2 6.8.2
1.4.01.01.0A	Climate modification increases recharge	Climate modification (natural or artificial) causes an increase in recharge in the Yucca Mountain region. Increased recharge might lead to increased flux through the repository, perched water, or water table rise.	6.2.1.3 6.5.2 6.7.2 6.8.2
2.1.08.01.0A	Water influx at the repository	An increase in the unsaturated water flux at the repository affects thermal, hydrological, chemical, and mechanical behavior of the system. Increases in flux could result from climate change, but the cause of the increase is not an essential part of the FEP.	6.5.2 (climate) 6.7.2 (climate) 6.8.2 (climate) 6.5.5.1 (reflux) 6.7.5.1 (reflux) 6.8.5.2 (reflux)
2.2.03.01.0A	Stratigraphy	Stratigraphic information is necessary information for the performance assessment. This information should include identification of the relevant rock units, soils and alluvium, and their thickness, lateral extents, and relationships to each other. Major discontinuities should be identified.	4.1.2 6.5.1 6.7.1 6.8.1
2.2.03.02.0A	Rock properties of host rock and other units	Physical properties such as porosity and permeability of the relevant rock units, soils, and alluvium are necessary for the performance assessment. Possible heterogeneities in these properties should be considered. Questions concerning events and processes that may cause these physical properties to change over time are considered in other FEPs	4.1.1 6.2.1 6.4.4 6.6.1.1
2.2.07.02.0A	Unsaturated groundwater flow in the geosphere	Groundwater flow occurs in unsaturated rocks in most locations above the water table at Yucca Mountain, including at the location of the repository. See other FEPs for discussions of specific issues related to unsaturated flow. See related FEPs 2.2.07.03.0A (capillary rise), 2.2.07.04.0A (focusing of unsaturated flow), 2.2.07.05.0A (effects of episodic infiltration), 2.2.07.07.0A (perched water), 2.2.07.08.0A (fracture flow), 2.2.07.09.0A (matrix imbibition), 2.2.07.10.0A (condensation zone forms), 2.2.07.11.0A (resaturation of dry-out zone), and 2.2.10.10.0A (two-phase flow / heat pipes).	6.2.1

Table 6.1-1. Features, Events, and Processes Relevant to this Model Report and Included into TSPA-LA (continued)

LA FEP Number	FEP Name	YMP Description	Sections Discussing FEPs-Related Items In this Model Report
2.2.07.04.0A	Focusing of unsaturated flow (fingers, weeps)	Unsaturated flow can differentiate into zones of greater and lower saturation (fingers) that may persist as preferential flow paths. Heterogeneities in rock properties, including fractures and faults, may contribute to focusing. Focused flow may become locally saturated.	6.2.1 6.6.2.2
2.2.07.08.0A	Fracture flow in the UZ	Fractures or other analogous channels act as conduits for fluids to move into the subsurface to interact with the repository and as conduits for fluids to leave the vicinity of the repository and be conducted to the SZ. Water may flow through only a portion of the fracture network, including flow through a restricted portion of a given fracture plane.	6.2.1 6.4.3
2.2.07.09.0A	Matrix imbibition in the UZ	Water flowing in fractures or other channels in the unsaturated zone is imbibed into the surrounding rock matrix. This may occur during steady flow, episodic flow, or into matrix pores that have been dried out during the thermal period.	6.2.1
2.2.07.10.0A	Condensation zone forms around drifts	Condensation of the two-phase flow generated by repository heat forms in the rock where the temperature drops below the local vaporization temperature. Waste package emplacement geometry and thermal loading will affect the scale at which condensation caps form (over waste packages, over panels, or over the entire repository), and to the extent to which "shedding" will occur as water flows from the region above one drift to the region above another drift or into the rock between drifts.	6.2.1 6.5.5.1 6.6.2.1 6.8.5.4
2.2.07.11.0A	Resaturation of geosphere dryout zone	Following the peak thermal period, water in the condensation cap (see FEP 2.2.07.10.0A) may flow downward into the drifts. Influx of cooler water from above, such as might occur from episodic flow, may accelerate return flow from the condensation cap by lowering temperatures below the condensation point. Percolating groundwater will also contribute to resaturation of the dry out zone. Vapor flow, as distinct from liquid flow by capillary processes, may also contribute.	6.2.1 6.5.5 6.6.2 6.7.5 6.8.5
2.2.07.20.0A	Flow diversion around repository drifts	Flow in unsaturated rock tends to be diverted by openings such as waste emplacement drifts due to the effects of capillary forces. The resulting diversion of flow could have an effect on seepage into the repository. Flow diversion around the drift openings could also lead to the development of a zone of lower flow rates and low saturation beneath the drift, known as the drift shadow (see FEP 2.2.07.21.0A).	6.2.1 6.5.5.1 6.6.2.1 6.8.5.4

Table 6.1-1. Features, Events, and Processes Relevant to this Model Report and Included into TSPA-LA (continued)

LA FEP Number	FEP Name	YMP Description	Sections Discussing FEPs-Related Items In this Model Report
2.2.08.01.0B	Chemical characteristics of groundwater in the UZ	Chemistry and other characteristics of groundwater in the unsaturated zone may affect groundwater flow and radionuclide transport of dissolved and colloidal species. Groundwater chemistry and other characteristics, including temperature, pH, Eh, ionic strength, and major ionic concentrations, may vary spatially throughout the system as a result of different rock mineralogy.	4.1.3 6.2.2. 6.5.5.2 6.6.2.3 6.7.5.2 6.8.5.3 (Radionuclide and colloidal transport are addressed)
2.2.08.04.0A	Redissolution of *precipitates directs* more corrosive fluids to containers	Redissolution of precipitates which have plugged pores as a result of evaporation of groundwater in the dry-out zone, produces a pulse of fluid reaching the waste packages when gravity-driven flow resumes, which is more corrosive than the original fluid in the rock. See FEP 2.2.07.11.0A for a discussion of return flow from the condensation cap.	6.4.5 6.8.5.3
2.2.08.12.0A	Chemistry of water flowing into the drift	Inflowing water chemistry may be used in analysis or modeling that requires initial water chemistry in the drift. Chemistry of water flowing into the drift is affected by initial water chemistry in the rock, mineral and gas composition in the rock, and thermal hydrological-chemical processes in the rock.	6.2.1.2 6.2.2 6.5.5.2 6.6.2.3 6.7.5.2 6.8.5.3
2.2.10.10.0A	Two-phase buoyant flow / heat pipes	Heat from waste generates two-phase buoyant flow. The vapor phase (water vapor) escapes from the mountain. A heat pipe consists of a system for transferring energy between a hot and a cold region (source and sink respectively) using the heat of vaporization and movement of the vapor as the transfer mechanism. Two-phase circulation continues until the heat source is too weak to provide the thermal gradients required to drive it. Alteration of the rock adjacent to the drift may include dissolution, which maintains the permeability necessary to support the circulation (as inferred for some geothermal systems).	6.2.1
2.2.10.12.0A	Geosphere dry-out due to waste heat	Repository heat evaporates water from the UZ rocks near the drifts as the temperature exceeds the vaporization temperature. This zone of reduced water content (reduced saturation) migrates outward during the heating phase (about the first 1000 years) and then migrates back to the containers as heat diffuses throughout the mountain and the radioactive sources decay.	6.2.1 6.5.5.1 6.6.2.2 6.7.5.1 6.8.5.2

Table 6.1-2. Features, Events, and Processes Relevant to this Model Report and Excluded from TSPA-LA

LA FEP Number	FEP Name	YMP Description	Sections Discussing FEPs-Related Items In this Model Report
2.2.08.03.0B	Geochemical interactions and evolution in the UZ	Groundwater chemistry and other characteristics, including temperature, pH, Eh, ionic strength, and major ionic concentrations, may change through time, as a result of the evolution of the disposal system or from mixing with other waters. Geochemical interactions may lead to dissolution and precipitation of minerals along the groundwater flow path, affecting groundwater flow, rock properties and sorption of contaminants. Effects on hydrological flow properties of the rock, radionuclide solubilities, sorption processes, and colloidal transport are relevant. Kinetics of chemical reactions should be considered in the context of the time scale of concern. See also FEPs 2.2.08.01.0B (groundwater chemistry) and 2.2.08.07.0B (solubility).	6.2.2. 6.5.5.2 6.6.2.3 6.7.5.2 6.8.5.3 (Sorption effects and colloidal transport are not addressed)
2.1.09.12.0A	Rind (chemically altered zone) forms in the near-field	Thermal-chemical processes involving precipitation, condensation, and re-dissolution alter the properties of the adjacent rock. These alterations may form a rind, or altered zone, in the rock, with hydrological, thermal, and mineralogical properties different from the initial conditions.	6.2.1 6.4.4 6.5.5.2 6.6.2.3.1 6.7.5.2 6.8.5.4

6.2 CONCEPTUAL MODEL

This section describes the conceptual model underlying the Drift-Scale THC Seepage Model. The THC Seepage Model conceptualization is presented below in several parts. The first part deals with the conceptualization of the coupled processes that need to be taken into account to model water-gas-rock interactions in a heated unsaturated and fractured rock environment. In the second part, the conceptualization of the chemical system is presented, and a rationale is laid out for selecting input water compositions, mineral phases, and chemical constituents included within the model. Finally, the conceptualization of the physical model domain being modeled is discussed.

6.2.1 Conceptualization of Coupled THC Processes

The THC conceptual model underlies the numerical simulations of THC processes in the DST THC Model and in the THC Seepage Model. The TH conceptual model must be able to describe processes involving liquid and vapor flow, heat transport, and thermal effects resulting from boiling and condensation. The THC Conceptual Model must treat the transport of aqueous and gaseous species, mineralogical characteristics and changes, and aqueous and gaseous chemistry. A conceptual model of reaction-transport processes in the fractured welded tuffs of the repository host rock must also account for different rates of transport in highly permeable fractures compared to the much less permeable rock matrix (see for example, Steefel and Lichtner 1998 [144878], pp. 186–187).

In addition to the unsaturated hydrological properties required to simulate THC processes in the UZ, the data necessary for the evaluation of THC processes include the initial and boundary water and gas chemistry, the initial mineralogy, mineral volume fractions, reactive surface areas, equilibrium thermodynamic data for minerals, aqueous and gaseous species, kinetic data for mineral-water reactions, and diffusion coefficients for aqueous and gaseous species. The following subsections describe the conceptual model for thermal-hydrological (TH), geochemical, and coupled THC processes in the fractured tuffs.

6.2.1.1 TH Processes

TH processes in the fractured welded tuffs at Yucca Mountain have been examined theoretically and experimentally since the early 1980s (Pruess et al. 1984 [144801]; Pruess et al. 1990 [100818]; Buscheck and Nitao 1993 [100617]; Pruess 1997 [144794]; Tsang and Birkholzer 1999 [137577]; Kneafsey and Pruess 1998 [145636]). A conceptual model showing the important TH processes occurring around a drift (as derived through these studies and through observations of the Single Heater Test and the DST) is shown in Figure 6.2-1. This diagram also indicates (in boxes) the important parameters and issues addressed in the THC Seepage Model simulations. To summarize the processes as depicted in the figure, heat conduction from the drift wall into the rock matrix results in vaporization and boiling, with vapor migration out of matrix blocks into fractures. The vapor moves away from the drift through the permeable fracture network by buoyancy, by the increased vapor pressure caused by heating and boiling, and through local convection. In cooler regions, the vapor condenses on fracture walls, where it drains through the fracture network either down toward the heat source from above or away from the drift into the zone underlying the heat source. Slow imbibition of water from fractures into the matrix gradually leads to increases in the liquid saturation in the rock matrix. Under conditions of continuous heat loading, a dryout zone may develop closest to the heat source separated from the condensation zone by a nearly isothermal zone maintained at about the boiling temperature. Where this nearly isothermal zone is characterized by a continuous process of boiling, vapor transport, condensation, and migration of water back to the heat source (either by capillary forces or gravity drainage), this zone may be termed a heat pipe (Pruess et al. 1990 [100818], p. 1235).

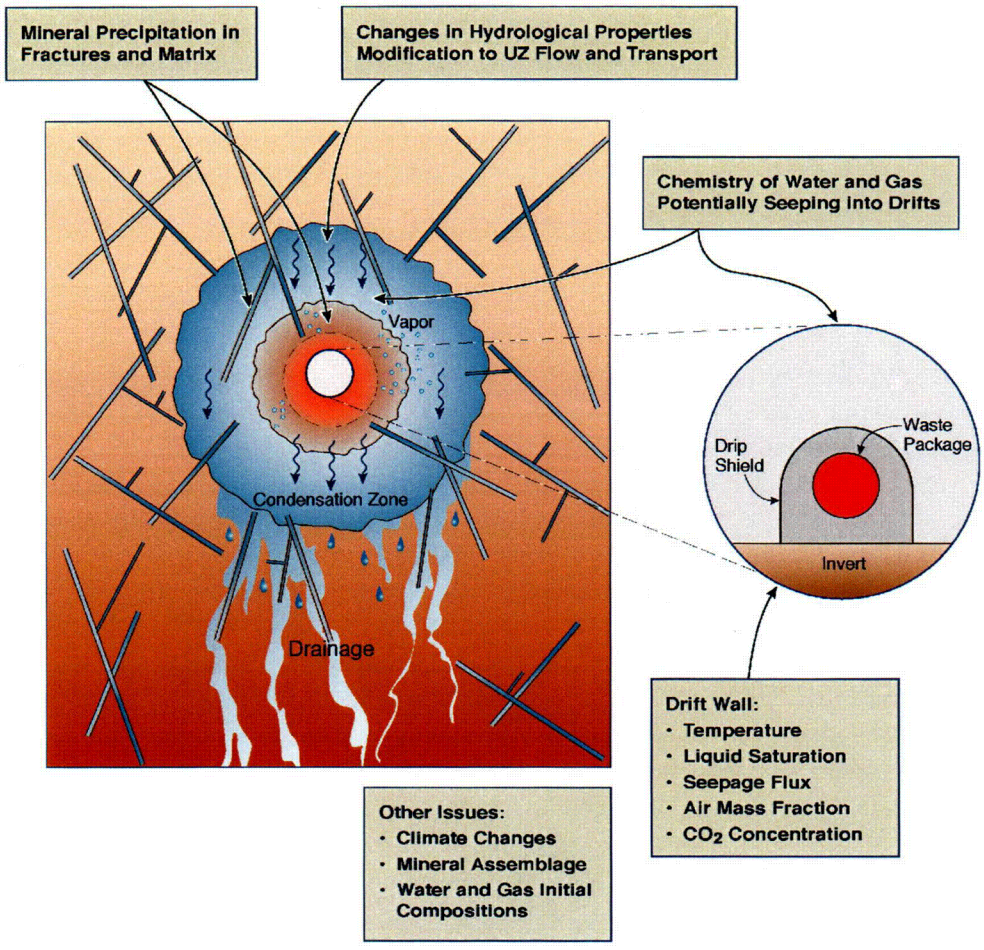

Figure 6.2-1. Schematic Diagram of THC Processes around a Heated Drift

6.2.1.2 THC Processes

The chemical evolution of waters, gases, and minerals is intimately coupled to the TH processes (boiling, condensation, and drainage) discussed in the previous section. The distribution of condensate in the fracture system determines where mineral dissolution and precipitation can occur in the fractures and where there can be direct interaction (via diffusion) between matrix pore waters and fracture waters. Figure 6.2-2 shows schematically the relationships between TH and geochemical processes in the zones of boiling, condensation, and drainage in the rock mass at the fracture-matrix interface outside of the drift and above the heat source.

C01

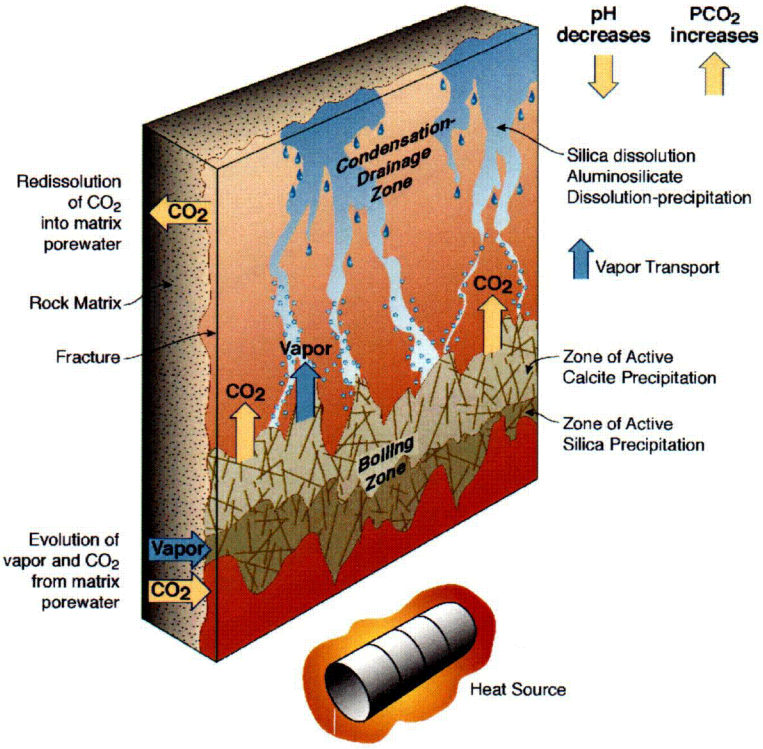

Figure 6.2-2. Schematic Diagram of Fracture-Matrix Interface, Showing the Relation Between TH Processes and Geochemical Processes

One important aspect of the system is the exsolution of CO_2 from the liquid phase as temperature increases. The exsolution of CO_2 in the boiling zone results in a local increase in pH, and a decrease in pH in the condensation zone into which the vapor enriched in CO_2 is transported and condensed. The extent to which the pH is shifted depends strongly on the rates of mineral-water reactions, which can buffer the change in pH. Because the diffusivities of gaseous species are several orders of magnitude greater than those of aqueous species, and because the advective transport of gases can be more rapid than that of liquids, the region where CO_2 degassing affects water and gas chemistry could be much larger than the region affected by the transport of aqueous species.

The effects of TH processes on water chemistry are varied and depend on the behavior of the dissolved species and their relation to mineral-water reactions. Conservative species (i.e., those that are unreactive and nonvolatile), such as chloride (Cl^-), become concentrated in waters undergoing vaporization or boiling, but are essentially absent from the vapor condensing in the fractures. Therefore, the concentration of conservative species in the draining condensate waters is determined by mixing with fracture pore waters and diffusive mixing with matrix pore waters. Concentrations of aqueous species, such as calcium (Ca^{+2}), are also affected by calcite dissolution or precipitation, as well as by reactions involving Ca-bearing zeolites, clays, and plagioclase feldspar.

Zonation in the distribution of mineral phases can occur as a result of differences in mineral solubility as a function of temperature. The inverse relation between temperature and calcite solubility (as opposed to the silica phases, which are more soluble at higher temperatures) can

CO2

cause zonation in the distribution of calcite and silica phases in both the condensation and boiling zones (Figure 6.2-2). Precipitation of amorphous silica or another silica phase is likely to be confined to a narrower zone where evaporative concentration from boiling exceeds its solubility. In contrast, calcite could precipitate in fractures over a broad zone of elevated temperature and where CO_2 has exsolved because of temperature increases or boiling. Alteration of feldspars to clays and zeolites is likely to be most rapid in the boiling zone because of their increased solubility (as well as having higher dissolution and precipitation rates) at higher temperatures (Lasaga 1998 [117091], p. 66). In drainage zones, mineral alteration could be zoned within the rock matrix adjacent to a fracture, in a similar manner to that observed as a function of distance along the transport path (Steefel and Lichtner 1998 [144878], p. 186).

6.2.1.3 Effects of Infiltration and Climate Changes on THC Processes

Early in the thermal period of the repository, much of the chemistry of the UZ around drifts will be constrained by the chemistry of ambient fracture and matrix pore water, which could change as a result of boiling, dilution with condensate water, or mineral-water-gas reactions. Once the peak thermal period has subsided, percolating water will mix with the condensate above the repository and eventually rewet the dryout zone. The composition of the percolating waters (before mixing) could be similar to that presently found above the repository as matrix pore water, or it could be more dilute, reflecting wetter climate conditions. Changes in the percolation flux also affect the extent of mineral deposition and dissolution, because of the changes in the flux of dissolved species to the region around drifts. For example, the greater the flux of calcium, the more calcite would precipitate, for a given initial calcium concentration in percolating water. Higher percolation fluxes could increase the dissolution rates of minerals that are undersaturated in the fluid, because it could increase the degree to which the mineral is undersaturated.

6.2.1.4 Hydrological Property Changes in Fractures and Matrix

Mineral precipitation and dissolution in fractures and matrix have the potential for modifying the porosity, permeability, and unsaturated hydrological properties of the system. Because the molar volumes of minerals created by hydrolysis reactions (i.e., anhydrous phases, such as feldspars, reacting with aqueous fluids to form hydrous minerals, such as zeolites or clays) are commonly larger than the molar volumes of the primary reactant minerals, dissolution-precipitation reactions commonly lead to porosity reductions. The extent of mineral-water reaction is controlled by the surface areas of the mineral phases in contact with the aqueous fluid, and heterogeneity in the distribution of minerals in the fractures. Therefore, changes in porosity and permeability caused by these processes may also be heterogeneously distributed. Other factors that could lead to heterogeneity in property changes are the distribution of liquid saturation in fractures, the proportion of fractures having actively flowing water, and the rates of evaporative concentration due to boiling, which could change the dominant mechanisms of crystal growth and nucleation.

6.2.1.5 Dual-Permeability Model for THC Processes

Transport rates by fluid flow in fractures greater than the rate of equilibration via diffusion necessarily leads to disequilibrium between waters in fractures and matrix. This disequilibrium can lead to differences in the prevailing mineral assemblage and to differences in reaction rates.

Because the system is unsaturated and undergoes boiling, the transport of gaseous species is an important consideration. The model must also capture the differences between the initial mineralogy in fractures and matrix and their evolution. These separate yet interacting processes in fractures and matrix were treated by adapting the dual-permeability model to include geochemical as well as hydrological and thermal processes. In the dual-permeability model, each gridblock is partitioned into matrix and fracture continua, each characterized by its own pressure, temperature, liquid saturation, water and gas chemistry, and mineralogy. Figure 6.2-3 illustrates the dual-permeability conceptual model used for THC processes in the Drift-Scale THC Seepage Model and the DST THC Model.

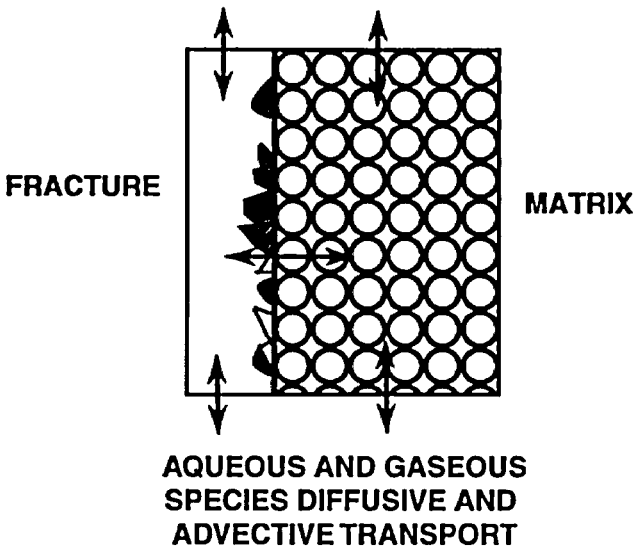

NOTE: Arrows refer to aqueous and gaseous species transport pathways. Angular objects in the fracture are minerals coating the fracture surface.

Figure 6.2-3. Conceptual Model (Schematic) for Reaction-Transport Processes in Dual-Permeability Media

As summarized in the preceding subsection, the conceptual model for THC processes incorporates a wide range of coupled physical and chemical processes. The following subsection describes the implementation of this conceptual framework into a numerical model.

6.2.2 Conceptualization of the Chemical System

The rationale used for defining the types and concentrations of chemical constituents (solid and gaseous) included in the THC Seepage Model is presented below. It includes the selection of initial pore-water and pore-gas compositions, the types and initial abundance of primary minerals, and the secondary minerals that may precipitate as the result of water-gas-rock interactions.

6.2.2.1 Initial Pore-Water and Pore-Gas Chemistry

The initial water composition input into the model could be chosen from either the pore-water chemistry in the UZ at or above the repository horizon, or from the perched water or saturated zone. The perched waters are generally much more dilute than UZ pore waters. Isotopic compositions ($^{36}Cl/Cl$, $^{18}O/^{16}O$, D/H, ^{14}C) and chloride concentrations suggest that the perched waters have a large proportion of late Pleistocene/early Holocene water (Levy et al. 1997 [126599], p. 906; Sonnenthal and Bodvarsson 1999 [117127], pp. 107–108). The saturated zone water is also more dilute than pore waters, and neither saturated nor perched water reflect calculated CO_2 partial pressures consistent with CO_2 concentrations in gas measured in the unsaturated zone in repository units. The saturated zone and perched-water compositions are therefore deemed poor candidates as initial input water compositions for the THC Seepage Model. Preference is given instead to actual pore waters from unsaturated regions within or above the repository units.

A conceptual model that explains the aqueous chemistry and background $^{36}Cl/Cl$ isotopic ratios in the ESF holds that percolating water must pass mostly through the Paintbrush nonwelded hydrogeologic unit (PTn) matrix (because of its high permeability and low fracture density) before reverting to predominantly fracture flow in the Topopah Spring welded hydrogeologic unit (TSw). As discussed in Levy et al. (1997 [126599], pp. 907–908), this seems to be true everywhere except near large structural discontinuities in the PTn (i.e., faults). Hence, percolating water in the TSw ultimately had come predominantly through the PTn matrix. Analyses of PTn pore waters (and some at the top of the TSw) and many chloride analyses of TSw pore waters are consistent with this interpretation (Sonnenthal and Bodvarsson 1999 [117127], pp. 140–141). The relatively higher concentrations of anions and cations in pore waters (compared to perched water) from the TSw, similar to PTn waters, are consistent with the premise that the waters had flowed through the PTn matrix.

The initial composition of water in fractures is taken to be the same as in the rock matrix throughout the model domain, using the same initial composition in all hydrogeologic units. The composition of water infiltrating the top of the model domain (in the Tiva Canyon welded hydrogeologic unit—TCw) is also set to be the same as the initial fracture and matrix pore-water composition, with the exception of minor changes related to a pH adjustment, reflecting a higher CO_2 partial pressure and a lower temperature at the top model boundary than deeper into the model domain (see below). Setting nearly identical compositions for infiltration at the top model boundary and initial fracture-matrix waters is a simplification of the natural system to avoid having to consider complex near-surface geochemical and transport processes such as evapotranspiration and biologically mediated reactions. It is also expected that the high matrix permeability and low fracture density in the PTn hydrogeologic unit (overlying the TSw) homogenize flow in this unit and thus homogenize the compositions of waters originating further up the stratigraphic column, further justifying this modeling approach.

At the initiation of this study, only a few nearly complete pore-water analyses from a repository unit were available. These were of water ultracentrifuged from core samples collected from the Tptpmn geologic unit in Alcove 5 near the DST. Three water samples were analyzed (HD-PERM-1, HD-PERM-2, and HD-PERM-3) from the same suite of core and yielded very similar compositions. Two of these analyses with nearly identical compositions were averaged for use as

an input water composition for pre-REV02 work (Table 6.2-1). Since then, a series of pore-water samples from repository host units have been analyzed. These samples were ultracentrifuged from core collected in the ECRB Cross Drift and in boreholes SD-9 and NRG-7/7A. The compositions of these waters are shown on a Piper diagram in Figure 6.2-4, together with the composition of HD-PERM samples, of perched water and pore water at similar depths (base of Tptpln) in borehole UZ-14, and of groundwater from well J-13. This figure also shows the hydrogeologic units from which the water samples were extracted. It is evident from Figure 6.2-4 that the span of potential initial water compositions to use in the THC Seepage Model is wide, with HD-PERM samples at one end (calcium-sulfate-chloride type) and groundwater from well J-13 at the other end (sodium-bicarbonate type). This figure also shows a tendency for samples from deeper hydrogeologic units to exhibit higher sodium (plus potassium) concentrations relative to calcium (plus magnesium) concentrations, and a higher proportion of aqueous carbonate (relative to chloride and sulfate) compared to shallower waters. The sodium increase relative to calcium with depth has been noted previously in pore-waters from hydrogeologic units above and below the repository units (Yang et al. 1996 [100194], p. 13). It is likely caused by the hydrolysis of volcanic glass and feldspars and, mostly below the repository units, exchange reactions with zeolites (e.g., BSC 2002 [160247]; Vaniman et al. 2001 [157427]). The precipitation of calcite in fractures under the ambient geothermal gradient would also exacerbate the decrease in calcium relative to sodium concentrations with depth. Trends in carbonate concentrations relative to chloride and sulfate concentrations are subject to large uncertainties as a result of the determination of total aqueous carbonate concentrations. An increase in aqueous carbonate concentration with depth could be attributed to the pH increase expected to accompany glass and feldspar hydrolysis reactions.

The differences in the proportions (not absolute values) of cations and anions in analyzed waters have an important bearing on the types of residual brines that could develop upon evaporation and boiling due to thermal loading (*In-Drift Precipitates/Salts Analysis*, see upcoming revision of BSC 2001 [156065]. Should these waters seep onto the surface of a hot waste package, knowledge of their end-brine composition is important to assess the likelihood and intensity of waste package corrosion (*Engineered Barrier System: Physical and Chemical Environment Model*, see upcoming revision of CRWMS M&O 2000 [151951]). Therefore, the span of selected input water compositions should take into account factors that influence the end-brine composition of these waters. One important factor is whether calcium (and magnesium) chloride brines could develop instead of sodium chloride brines. Calcium chloride brines can "survive" higher temperatures (i.e., exist at a lower relative humidity, more hygroscopic) than sodium chloride brines. Such brines are more likely to form if the total calcium concentration (in meq/L) exceeds the total aqueous carbonate concentration (in meq/L) in the initial water (calcite precipitation chemical divide; e.g., Drever 1997 [140067]). Waters with such compositions would have a tendency to plot in the upper half of the diamond-shaped area in Figure 6.2-4, although other waters may also plot in this area if their magnesium concentration were high relative to calcium. Other chemical divides after calcite precipitation (e.g., Drever 1997 [140067], p. 331; see also Rosenberg et al. 2001 [154862], p. 1238) could result in the development of brines that are less hygroscopic than calcium or magnesium chloride, even though the calcium content of the original waters (in equivalents) exceeds their total carbonate content. Less hygroscopic brines are more likely to develop if the nitrate and sulfate concentration in the original solution were elevated relative to chloride (*In-Drift*

Precipitates/Salts Analysis, see upcoming REV01 (BSC 2001 [156065])). No simple *a priori* criteria have been developed to determine with certainty the end-brine composition of a given water. However, factors such as composition plotting in the upper half of the diamond-shape area of Figure 6.2-4, together with low nitrate and sulfate concentrations relative to chloride, could be used to infer a higher likelihood of potentially deleterious brines developing.

The choice of input water composition must also consider the natural variability of pore-water compositions in the repository units. This natural variability is illustrated in Figure 6.2-4. The spatial coverage of these data is too small to associate a probability of occurrence for any of these pore-water compositions. From the considerations discussed above, one could expect deeper waters to exhibit lower calcium and higher total carbonate concentrations and therefore be less conducive to the formation of calcium chloride brines. However, other factors could affect the spatial distribution of pore-water compositions in the repository units. These factors include variations of infiltration rates in various parts of the repository footprint (Sonnenthal and Bodvarsson 1999 [117127], pp. 122–123) and possibly the presence or absence of ion-exchanging zeolites in areas above the repository. Furthermore, as noted above, the evolution of brine composition upon evaporation and boiling follows many other chemical divides besides the first calcite divide mentioned earlier.

Table 6.2-1. Input Pore-Water Compositions for the THC Seepage Model

Sample ID:		HD-PERM[1] (Alcove 5)		ECRB-SYS-CS1000/7.3-7.7/UC[2]		ECRB-SYS-CS2000/16.5-21.1/UC[2]		SD-9/990.4-991.7/UC[2]		ECRB-SYS-CS500/12.0-16.7/UC[2]	
Lithostratigraphic Unit:		Tptpmn		Tptpul (base)		Tptpll		Tptpll		Tptpul	
Simulation Water ID:		W0		W5		W4		W6		W7	
Water Input Type:		Fract/Matrix	Boundary	Fract/Matrix	Boundary	Fract/Matrix	Boundary	Fract/Matrix	Boundary	Fract/Matrix	Boundary
	Units										
Temperature	°C	25	17	25	17	25	17	25	17	25	17
pH (measured)	pH	8.31	-	7.6	-	7.4	-	7.9	-	8.0	-
pH (calc)[3]	pH	-	7.750	8.062	8.026	8.175	8.140	8.001	7.964	8.073	8.038
Na^+	mg/L	61.5	61.5	39	39	130	130	84	84	57	57
K^+	mg/L	8	8	7.6	7.6	10.6	10.6	7.9	7.9	10.3	10.3
Ca^{+2}	mg/L	101	101	94	94	82	82	56	56	120	120
Mg^{+2}	mg/L	17	17	18.1	18.1	5.3	5.3	0.9	0.9	19.3	19.3
SiO_2	mg/L	70.5	70.5	42.0	42.0	48	48	50	50	49	49
Cl^-	mg/L	117	117	21	21	26	26	23	23	54	54
SO_4^{-2}	mg/L	116	116	36	36	39	39	10	10	78	78
HCO_3^- (measured)	mg/L	-	-	333	-	382	382	313	-	286	-
HCO_3^- (calc)[4]	mg/L	200	216	395	400	515	515	335	338	412	417
NO_3^-	mg/L	6.5	6.5	2.6	2.6	4.2	4.2	17	17	6.1	6.1
F^-	mg/L	0.86	0.86	3.4	3.4	6.01[9] (11)	5.52	2.5	2.5	4.8	4.8
Al^{+3} (calc)[5]	molal	6.173E-10	9.775E-11	1.112E-09	3.415E-10	1.082E-09	3.305E-10	1.00E-09	3.08E-10	8.061E-10	2.477E-10
Fe^{+3} (calc)[6]	molal	1.155E-12	5.162E-13	1.138E-12	5.000E-13	1.143E-12	4.984E-13	1.14E-12	5.02E-13	1.138E-12	5.006E-13
$\log(PCO_2)$[7]	bar	-3.1	-2.5	-2.5	-2.5	-2.5	-2.5	-2.5	-2.5	-2.5	-2.5
CO_2 (approx)[8]	ppmv	900	3100	3100	3100	3100	3100	3100	3100	3100	3100

NOTES: Compositions shown are those used for initial fracture and matrix water (column labled "Fract/Matrix") and infiltration water at the model top boundary (column labeled "Boundary")

(1) Average of Tptpmn porewater analyses ESF-HD-PERM-2 (30.1'-30.5') and ESF HD-PERM-3 (34.8'-35.1'), DTN: MO0005PORWATER.000 [150930]

(2) Pore water analyses from the ECRB cross-drift and borehole SD-9 reported with DTN: GS020408312272.003 [160899]

(3) pH calculated by speciation at the temperature and $\log(P_{CO2})$ shown (using SOLVEQ/CHILLER V1.0 [153217]).

(4) Total aqueous carbonate as HCO_3^-, calculated from charge balance computed by speciation at the temperature and pH shown (at measured pH for HD-PERM sample; at calculated pH for other samples) (using SOLVEQ/CHILLER V1.0 [153217]). Note: these are slightly different values than values calculted fom charge balance reported in DTN: GS020408312272.003 [160899] because the latter do not include the effect of speciation .

(5) Calculated by equilibrating with illite at the temperature and calculated pH shown (using SOLVEQ/CHILLER V1.0 [153217]) (Section 6.2.2.1).

(6) Calculated by equilibrating with hematite at the temperature and calculated pH shown (using SOLVEQ/CHILLER V1.0 [153217]) (Section 6.2.2.1).

(7) Set at values shown except for HD-PERM sample at 25°C (calculated in this case) (Section 6.2.2.1).

(8) Approximate conversion assuming 1 bar total pressure.

(9) Value shown is calculated at equilibrium with fluorite at 25°C. Value in parentheses is measured value.

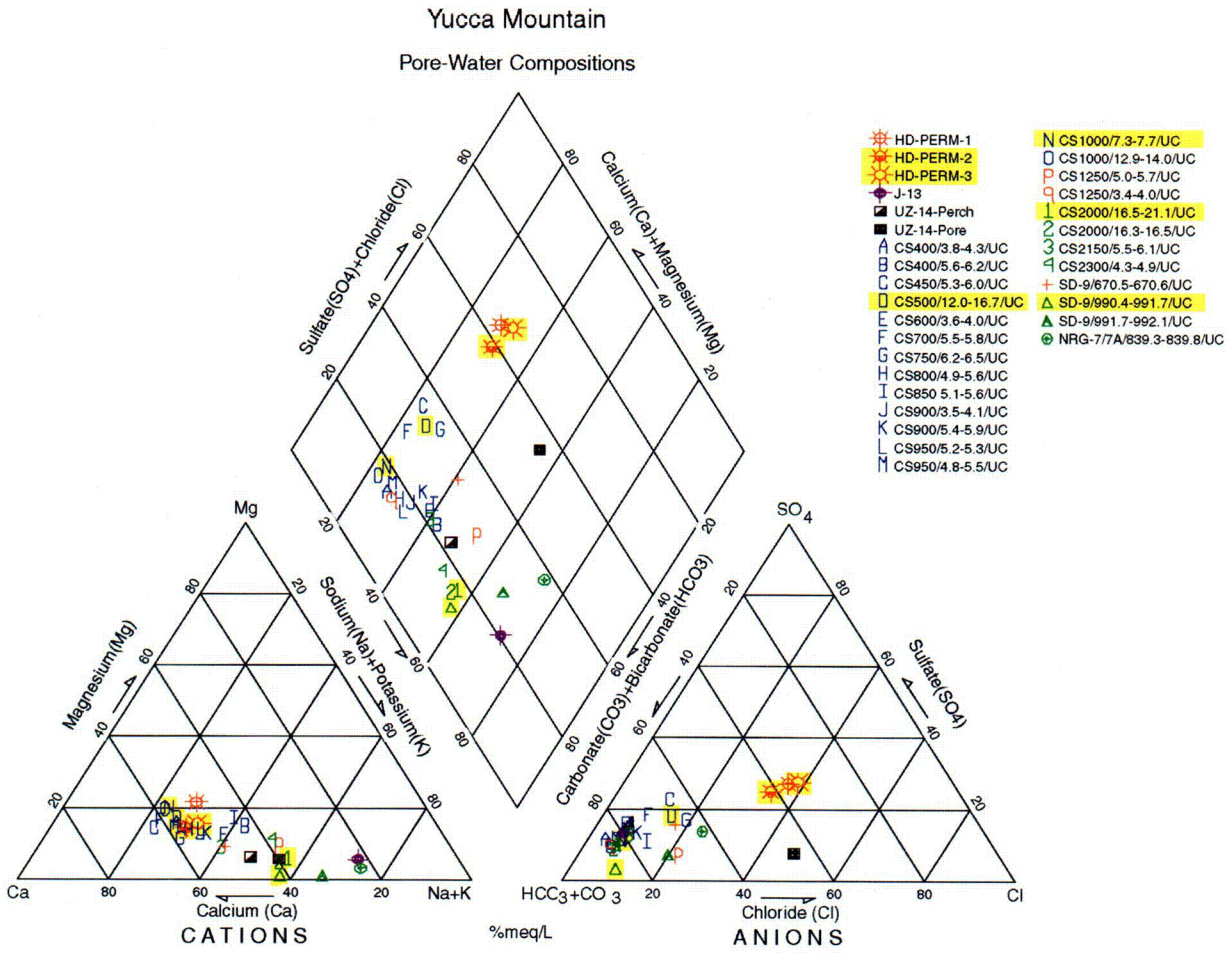

DTNs: GS020408312272.003 [160899], MO0005PORWATER.000 [150930]

NOTE: Samples labeled HD-PERM are pore waters from the Tptpmn unit in Alcove 5 of the ESF. Samples ID's starting with CS represent pore waters from the ECRB cross drift and are listed in order of increasing distance (m) into the drift (down stratigraphy), with labels reflecting lithostratigraphic units as follows: Tptpul (capitals A-O), Tptpmn (lower case p-q), and Tptpll (numbers 1-4). Additional borehole interval information after each CS sample labeling is sample interval distances from borehole collar given in feet. CS is abbreviation for Construction Station indicating distance along the ECRB cross drift in meters. Sample ID's starting with SD-9 and NRG-7 represent pore waters from boreholes with the same names and show the sampling interval in feet from ground surface. The first SD-9 sample at 670 ft is from the base of the Tptpul, and the others are from the Tptpll. The NRG7 sample is from the Tptpmn. Highlighted samples were chosen for this study (see text).

Figure 6.2-4. Piper Plot of Water Compositions (meq/L) from Repository Units

Given these considerations, initial water compositions were selected for REV02 simulations based on the following criteria:

(1) Capture the spread of pore-water compositions shown on Figure 6.2-4 and include, to the extent practicable, waters that may yield different end-brine compositions

(2) Include at least one pore water from the most important repository host unit (Tptpll)

(3) Use analyses that best balance charge if more than one sample meets the other criteria

C03

On these bases, the following water compositions were selected, listed here with an arbitrary identification (W0, W5, etc.) assigned for this Model Report:

"W0": HD-PERM water, from the Tptpmn unit in Alcove 5. This is an average composition (from Samples HD-PERM-2 and HD-PERM-3) used for all REV01 work. The HD-PERM samples plot higher than other pore waters on the diamond-shaped area in Figure 6.2-4, bounding the range of compositions in the calcium-sulfate-chloride field.

"W5": Sample CS-1000/7.3-7.7/UC, from the base of the Tptpul lithostratigraphic unit in the ECRB Cross Drift. This sample was selected because it exhibits one of the highest (Ca+Mg)/(Na+K) ratio of the ECRB Cross Drift samples, and exhibits better charge balance than other samples with high (Ca+Mg)/(Na+K) ratios.

"W4": Sample CS-2000/16.5-21.1/UC, from the Tptpll lithostratigraphic unit in the ECRB Cross Drift. This sample exhibits the lowest (Ca+Mg)/(Na+K) ratio of the ECRB Cross Drift samples and exhibits better charge balance than other samples of similar composition. Also, this sample is from the main repository host unit. It also contains a higher fluoride concentration than the other samples.

Upon further evaluation and a request from "downstream" project personnel, two additional samples were considered:

"W6": Sample SD-9/990.4-991.7, from the Tptpll lithostratigraphic unit in borehole SD-9. This sample exhibits a low (Ca+Mg)/(Na+K) ratio nearly identical to that of W4, but exhibits a better charge balance than W4 and a higher nitrate concentration compared to most other samples. This water is very similar in composition to Water W4.

"W7": Sample CS500/12.0-16.7, from the Tptpul lithostratigraphic unit in ECRB Cross Drift. This sample plots between the HD-PERM waters and Water W5 on Figure 6.2-4, further capturing the variability of water compositions in the upper part of Figure 6.2-4.

The compositions of these waters are given in Table 6.2-1. This table also includes calculated concentrations used for input into the THC Seepage Model, and distinguishes between the compositions used for initial fracture and matrix waters and slightly adjusted compositions used for infiltration water at the top model boundary, as discussed further below.

It is shown in Figure 6.2-4 that the water compositions chosen for input into the THC Seepage Model capture fairly well the spread of currently available pore-water compositions in repository units. Water compositions W4, W5, and W6 plot in the lower half of the diamond-shaped area on Figure 6.2-4. The HD-PERM waters and W7 plot in the upper half of this area, and for this reason may be more likely to evolve toward a calcium chloride brine than the other waters upon evaporation.

The set of analyzed species for these samples do not include iron and aluminum. Because these components are needed to include aluminum silicates in simulations, their concentrations were

calculated assuming equilibrium with hematite and illite, respectively. Illite was chosen to set the initial aluminum concentration because waters from Yucca Mountain typically plot on, or near, the illite-K-feldspar equilibrium boundary (Wang 2003 [161665], SN-LBNL-SCI-141-V2, pp. 176 and 184). Hematite is the most abundant iron oxide mineral found in the tuffs at Yucca Mountain and is a reasonable candidate to use for setting the initial iron concentration in solution.

The total aqueous carbonate concentration (reported here as HCO_3^-) was not measured in HD-PERM samples and was calculated from charge balance, after full speciation calculations (using SOLVEQ/CHILLER V1.0 (LBNL 1999 [153217])). Doing so yielded a partial pressure of CO_2 (at equilibrium with the HD-PERM water) near 10^{-3} bar, consistent with CO_2 concentrations near 1,000 ppmv measured in repository units in the ESF (DTN: LB0208ISODSTHP.001 [161638]) and in borehole UZ-1 (Yang et al. 1966 [100194], p. 43).

Total aqueous carbonate concentrations were reported for the other samples. However, the analyses of these samples reflect a fairly significant charge imbalance (2 to 11%). Also, it is known that aqueous carbonate analyses can be easily impacted by interference with atmospheric carbon dioxide during sample preparation. For these reasons, the carbonate concentrations were recalculated from charge balance after full speciation calculations.

Other adjustments were made to some of the reported analytical data before input into the model as follows. The pH reported for the ECRB and SD-9 samples yield equilibrium carbon dioxide partial pressures significantly higher (up to 14,000 ppmv) than what is observed in the repository units (typically around 1,000 ppmv). For this reason, the pH of these waters was recalculated to yield lower CO_2 partial pressures values more in line with concentrations measured in repository units. Bringing the CO_2 partial pressure down to near 1,000 ppmv required raising the water pH to values of 8.5 and higher. Such pH values seemed too high in comparison to values of 7.79, 8.31, and 8.32 reported for the HD-PERM samples (DTN: MO0005PORWATER.000 [150930]). Therefore, an intermediate but still reasonable CO_2 partial pressure around 3,100 ppmv ($\log(P_{CO_2}) \sim -2.5$) was used, yielding pH values in the 8–8.2 range (Table 6.2-1). In this respect, these water compositions are likely to represent high-end CO_2 concentrations, whereas the HD-PERM samples represent a somewhat lower bound.

Another adjustment to input water concentrations involved fluoride in sample ECRB-SYS-CS2000/16.5-21.1/UC. The fluoride concentration in this sample (11 mg/L) reflects a significant supersaturation with respect to fluorite (CaF_2 solid) at 25°C. The precipitation of fluorite is typically quite rapid (Section 4.1.5) and, for this reason, the fluoride concentration of this sample was lowered to a concentration reflecting saturation with fluorite (near 6 mg/L for this water).

As mentioned earlier, infiltration water at the top model boundary was taken to have the same composition as the initial pore water, but with adjusted total aqueous carbonate, aluminum, and iron concentrations to reflect a lower temperature (17°C) and higher CO_2 partial pressure near the ground surface. Using this boundary water yielded chemically steadier ambient water compositions at the location of the modeled drift (Section 6.4.3).

The initial CO_2 partial pressure in fractures and matrix was calculated as the partial pressure of CO_2 in chemical equilibrium with the input water composition at 25°C, assuming ideal gas

behavior (i.e., partial pressure is equal to fugacity). The 25°C temperature is close to the initial temperature at the location of the drift. For the Tptpmn THC Seepage Model, the initial CO_2 partial pressure in the drift was set to be consistent with a CO_2 concentration of 400 parts per million by volume (ppmv) in the drift, which is within the range of measured ambient concentrations in the ESF (DTN: LB990630123142.003 [111476]). For the Tptpll Seepage Model, the initial CO_2 partial pressure in the drift was assumed to be at equilibrium with the initial composition of pore water around the drift. The CO_2 concentration at the top model boundary was set (approximately 3,100 ppmv) to reflect a value consistent with the range of higher concentrations measured in shallow geologic units in borehole UZ-1 (Table 8 in Yang et al. 1996 [100194]). These higher CO_2 concentrations are most likely the result of biological activity near the ground surface.

6.2.2.2 Geochemical Systems

Minerals and chemical-aqueous components considered in this study are shown in Table 6.2-2. Initial mineral types and abundances were derived from x-ray diffraction (XRD) measurements on cores reported in the Yucca Mountain Mineralogical Model: LA9908JC831321.001 [113495] and analyses of fracture surfaces (Carlos et al. 1993 [105210], p. 47; LA9912SL831151.001 [146447]; LA9912SL831151.002 [146449]). Amounts of minerals observed, but present in quantities below the detection limit (typically around a percent for XRD) were estimated. Potential secondary minerals (i.e., those allowed to precipitate but which may not necessarily form) were determined from field observation of thermal alteration (e.g., Vaniman et al. 2001 [157427], p. 3409) and corroborated by running multicomponent heterogeneous equilibrium simulations of water-rock interaction (Wang 2003 [161665], SN-LBNL-SCI-141-V2, pp. 94–95) using SOLVEQ/CHILLER V1.0 (LBNL 1999 [153217]). From these simulations, the stable mineral assemblage at each reaction step was calculated from a large list of possible minerals (after suppressing phases known not to form under ambient pressures and low temperatures). For example, amorphous silica is allowed to precipitate instead of the other silica polymorphs, such as opal, tridymite, α-cristobalite, and quartz, because it is observed in experiments (Section 7). Anorthite is not observed as a secondary phase, so calcium enters other minerals such as zeolites and calcite.

The basis for selection of aqueous species included in this study were: (1) use the major components of pore water, (2) use all components in major rock-forming minerals considered in the model, and (3) use additional components specifically requested by downstream users (nitrate, iron, and fluoride).

Two alternative conceptualizations of the modeled geochemical system were used. The systems were denoted as "base case" and "extended case," and differ somewhat from one model variation to another (Table 6.2-2). The extended case includes the major solid phases (minerals and glass) encountered in geologic units at Yucca Mountain, together with a range of possible reaction product minerals, CO_2 gas, and the aqueous species necessary to include these solid phases and the pore-water composition within the THC model. The base case is a subset of the extended case excluding aluminum silicate minerals, which form or dissolve much less easily than minerals such as calcite or gypsum, and for which thermodynamic and kinetic data are not as well established as for the other minerals. As such, the base-case system conceptualizes a geochemical system in which aluminum silicate minerals are nonreactive. The base-case system

also does not include Fe- and Mg-bearing phases and aqueous species. The base-case system, in addition to the extended-case system, was only used in REV01 models. For REV02 work, only an extended-case geochemical system was considered.

Table 6.2-2. Minerals, Aqueous, and Gaseous Species Used in the THC Seepage Model

Aqueous Species		Minerals		
	Alternative Models		Alternative Models	Mineral Type[1]
H_2O	All	Calcite	All	P,S
H^+	All	Tridymite	All	P
Na^+	All	α–Cristobalite	All	P
K^+	a	Quartz	All	P
Ca^{+2}	All	Amorphous Silica	All	S
Mg^{+2}	a	Hematite	a	P,S
SiO_2	All	Fluorite	All	P,S
AlO_2^-	a	Gypsum	All	S
$HFeO_2^{-2}$	a	Goethite	d	S
HCO_3^-	All	Albite	a	P,S
Cl^-	All	K-Feldspar	a	P,S
SO_4^{-2}	All	Anorthite	a	P
F^-	All	Ca-Smectite	a	P,S
		Mg-Smectite	a	P,S
Gases		Na-Smectite	a	P,S
CO_2	All	Opal_proxy	b	P
H_2O	All	Illite	a	P,S
Air	All	Kaolinite	a	S
		Glass [2]	All	P
		Stellerite	a	P,S
		Heulandite	a	P,S
		Mordenite	a	P,S
		Clinoptilolite	a	P,S
		Sepiolite	c	S

NOTES: a Extended-case geochemical system only
b Only Tptpll REV01 and all REV02 models
c Only REV02 models
d Only REV01 extended-case models

[1] Primary (P) and secondary (S) minerals
[2] For base-case models, glass has the same thermodynamic properties as amorphous silica but is not allowed to precipitate.

6.2.3 Conceptualization of the Model Domain

The current repository design includes a planar series of parallel, equidistant, and horizontal waste emplacement drifts laid out over a large surface area. As such, encompassing all areas of the repository would require a large and detailed 3-D model. However, the scope of this Model Report covers THC processes at the drift scale. Therefore, the model was reduced and simplified to focus on areas surrounding a typical waste emplacement drift. Because the number of

gridblocks directly affects the simulation time, the model domain is reduced as much as possible without losing important information. The dip of repository host units is subhorizontal, and rock properties are laterally homogeneous between drifts. Under these conditions, a planar and parallel drift layout can be conceptualized, in two dimensions, as a series of symmetrical, identical half-drift X-Z models (X representing the horizontal distance in a direction perpendicular to the length of the drifts, and Z the vertical distance) with no-flux (heat, fluid, chemical) vertical boundaries between them. Note that this half-drift simplification based on symmetry is theoretically applicable only for homogeneous properties. It is, however, also a good approximation for the heterogeneous fracture permeability fields used in this report because of their weak spatial correlation.

Accordingly, the THC Seepage Model was reduced to a half-drift model with a width corresponding to the midpoint between drifts. The model is refined in the vicinity of the drift, and extends in a progressively coarser fashion to the TCw (near the ground surface) above the drift and to the water table below the drift. This symmetrical "chimney" model adequately represents coupled THC processes at the drift scale in areas that are not affected by repository-edge effects (i.e., effects resulting from the cooler temperature distribution at the repository edge). The evaluation of edge effects are not within the scope of this Model Report. Edge effects have been evaluated with mountain-scale THC simulations in BSC (2001 [155950], Section 3.3.6) and will be further addressed in upcoming revision of MDL-NBS-HS-000007, REV01. Water and gas compositions predicted at the edge of the repository (BSC 2001 [155950], Section 3.3.6) are within the range of compositions simulated in this Model Report. For this reason, results presented here could be used to represent potential effects of THC processes on the composition of seepage at all waste package locations.

6.3 ALTERNATIVE CONCEPTUAL MODELS

The THC Seepage Model includes various conceptualizations of drift location, drift representation, modeled stratigraphic column, geochemical systems, and boiling/evaporation mathematical models. These conceptualizations were implemented in various model variations and summarized as follows (see also Table 6-1):

- Tptpmn THC Model REV01 (Section 6.5). This model represents a stratigraphic column on the edge of the repository (borehole SD-9) and considers a drift in the Tptpmn lithostratigraphic unit. Two alternative geochemical systems are used with this model: a base-case system and an extended-case system (Section 6.2.2.2).

- Tptpmn THC Heterogeneous Model REV01 (Section 6.6). This model includes the same conceptualizations as the above model, except that it considers heterogeneous fracture permeability variations.

- Tptpll THC Model REV01 (Section 6.7). This model represents a stratigraphic column at the center of the repository with a drift in the Tptpll lithostratigraphic unit. Both base-case and extended-case geochemical systems (Section 6.2.2.2) are considered.

- Tptpll THC Model REV02 (Section 6.8). This model is an update of the REV01 Tptpll model. The following alternative conceptualizations are considered, compared to the

REV01 model: drift wall open to gas and liquid flow (versus closed in REV01), fixed versus stepwise increase in infiltration rate, and the effect of vapor-pressure lowering (resulting from capillary pressure) versus its absence.

Additional details on each of these alternative conceptualizations can be found in the sections noted above for each model variation. Alternative conceptualizations not treated here could yield differences in model results. Examples of such alternative models include the use of more than two porous media continua (to better represent lithophysae, and/or better capture gradients between fractures and matrix), heterogeneous fracture porosity (in addition to heterogeneous permeability), a wider range of infiltration rates, or other sets of potential secondary minerals, etc. These alternatives were not considered because they were expected to result in smaller differences in model results than the alternatives considered here. This is primarily because the range of input water compositions considered in the model (Section 6.2.2.1), by itself, already introduces a significant spread in model results (Section 6.8.5).

6.4 MATHEMATICAL MODEL

This section describes the mathematical formulations that underlie the THC Seepage Model (and the DST THC Model presented in Section 7). Reactive transport simulators other than TOUGHREACT and using various formulations exist. However, these simulators either have limitations that make them unsuitable for use in this study (e.g., dealing only with fully liquid-saturated conditions, or only with one continuum), or have drawbacks in terms of availability, technical support, and qualification status. TOUGHREACT (all versions) is the only software of its type that is qualified for Yucca Mountain work. Also, the authors of this report have contributed to the development of this software, and most particularly to its development for applications to the repository at Yucca Mountain. Therefore, it is natural that this software and its formulation were selected for this study.

For brevity, unless a formulation is used that is specific to a particular version of TOUGHREACT, hereafter the code version and reference are not cited.

6.4.1 General Numerical Model for Coupled THC Processes

Thermal and hydrological processes modeled using TOUGHREACT (all versions) are equivalent to those using TOUGH2 V1.6 (LBNL 2003 [161491]), and described in detail in BSC (2003 [161530], Section 6.2.1.1) and in the TOUGHREACT V3.0 User's Manual (BSC 2002 [164454]; LBNL 2002 [161256]).

The geochemical module incorporated in TOUGHREACT (V2.2 (LBNL 1999 [153219]); V2.3 (LBNL 2001 [153101]); V2.4 (LBNL 2001 [160880]); and V3.0 (LBNL 2002 [161256])) simultaneously solves a set of chemical mass-action, kinetic-rate expressions for mineral dissolution/precipitation, and mass-balance equations. This provides the extent of reaction and mass transfer between a set of given aqueous species, minerals, and gases at each gridblock of the flow model. Equations for heat, liquid and gas flow, aqueous and gaseous species transport, and chemical reactions are summarized in Xu and Pruess (2001 [156280], p. 30, Tables A and B (see also Xu and Pruess 1998 [117170]; Xu et al. 1998 [101751]; Xu et al. 2001 [161864])). Flow and reaction/transport equations are solved sequentially (e.g., Steefel and Lasaga 1994

[101480], p. 550). Equations for mineral-chemical equilibrium, kinetic rates, and permeability/porosity changes are given further below.

The setup of mass-action and mass-balance equations in TOUGHREACT V2.2 (LBNL 1999 [153219]), V2.3 (LBNL 2001 [153101]), and V3.0 (LBNL 2002 [161256]) is similar to the formulation implemented in Reed (1982 [117901], pp. 514–516). Additional provisions are made for mineral dissolution and precipitation under kinetic constraints and a volume-dependent formulation for gas equilibrium, as described below. The chemical system is described in terms of primary aqueous species (the independent variables). Minerals, gases, and secondary aqueous species are defined in terms of reactions involving only the primary species. It has been shown that if the diffusivities of all aqueous species are equal, only the transport of primary species (in terms of total dissolved concentrations) needs to be considered to solve the entire reactive flow/transport problem (Steefel and Lasaga 1994 [101480], p. 546).

The system of nonlinear equations describing chemical mass-balance, mass-action, and kinetic-rate expressions is solved by a Newton-Raphson iterative procedure. In TOUGHREACT V2.2 (LBNL 1999 [153219]), activity coefficients of aqueous species are computed by an extended Debye-Hückel equation (e.g., Drever 1997 [140067], p. 28, Equation 2-12). In TOUGHREACT V2.2 (LBNL 1999 [153219]), activity coefficients of neutral species are assumed equal to one, and the activity of water is computed using a method described in Garrels and Christ (1990 [144877], pp. 64–66), which essentially equates the water activity to its mole fraction. These methods are generally reliable for ionic strengths up to 2 molal. In TOUGHREACT V2.3 (LBNL 2001 [153101]), V2.4 (LBNL 2001 [160880]), and V3.0 (LBNL 2002 [161256]), activity coefficients of charged species and the activity of water are calculated with the method of Helgeson et al. (1981 [106024], Equations 298, 190, 106, and Tables 1, 3, 29, and 30) as further described in Wang 2003 ([161665], SN-LBNL-SCI-112-V2, pp. 21–27). Using this method, activities of water and activity coefficients of electrolytes typical of natural systems (NaCl, $CaCl_2$, Mg_2SO_4, Ca_2SO_4) were fairly well reproduced up to ionic strengths of 6 molal (Wang 2003 [161665], SN-LBNL-SCI-112-V2, pp. 28–30 and 32). In TOUGHREACT V2.3 (LBNL 2001 [153101]), V2.4 (LBNL 2001 [160880]), and V3.0 (LBNL 2002 [161256]), activity coefficients of selected neutral species are calculated using salting-out coefficients as described in Langmuir (1997 [100051], Equation 4.62 and Table 4.1-4).

Equilibration with mineral phases is computed by adding a mass-action equation, for each saturated mineral, into the system of nonlinear equations as follows:

$$\log(K_i) = \log(Q_i) \qquad \text{(Eq. 6.4-1)}$$

where K_i denotes the equilibrium constant and Q_i the product of the ion activities in the reaction that expresses mineral i in terms of the primary aqueous species. A term representing the amount of primary aqueous species consumed or produced by equilibration of minerals is added to the mass-balance equation for each primary species involved in mineral reactions, and this term is solved simultaneously with the concentrations of all primary species. Minerals thus dissolve if $\log (Q_i/K_i) < 0$ and precipitate if $\log (Q_i/K_i) > 0$. For some minerals (e.g., calcite in this report, see Section 6.4.3), a "supersaturation gap" can be specified, by which the mineral is not allowed to precipitate if $\log (Q_i/K_i)$ is greater than zero but less than a specified "gap" value (positive).

This gap can be set to decrease exponentially with temperature, as described in Wang 2003 ([161665], SN-LBNL-SCI-112-V2, p. 33).

Gas species, such as CO_2, are treated as ideal mixtures of gases in equilibrium with the aqueous solution. A mass-action equation is added to the system of simultaneous equations for each saturated gas present—except for H_2O vapor and air, which are handled separately through the flow module in TOUGHREACT. The gas mass-action equation takes the form:

$$\log(K_i) = \log(Q_i) - \log(P_i) \quad \text{(Eq. 6.4-2)}$$

where P_i is the partial pressure of gaseous species i. P_i is first calculated from the advective-diffusive gas transport equation in TOUGHREACT. Then P_i is replaced with the ideal gas law,

$$P_i = \frac{n_i RT}{V_g} \quad \text{(Eq. 6.4-3)}$$

where n_i denotes the number of moles of gas species i, R is the gas constant, T is the absolute temperature, and V_g is the gas total volume. By expressing V_g in terms of the gas saturation S_g, the porosity of the medium ϕ, and the volume of each gridblock in the flow model V_{block}, Equation 6.4-3 is rewritten as:

$$P_i = \frac{n_i RT}{V_{block} \phi S_g} \quad \text{(Eq. 6.4-4)}$$

The gas saturation is computed in the flow module of TOUGHREACT (reflecting H_2O and air partial pressures computed in this module). The amount of trace gas species (n_i/V_{block}) is then obtained by substitution of Equation 6.4-4 into Equation 6.4-2 and solving together with the concentrations of all primary species.

The partial pressures of trace gas species are not fed back to the multiphase flow module of TOUGHREACT V2.2 (LBNL 1999 [153219]) and V2.3 (LBNL 2001 [153101]) for solving the water and gas flow equations. Therefore, this method should only be applied to gases (excluding H_2O and air) with partial pressures significantly lower than the total gas pressure. No absolute cutoff exists at which this approximation breaks down, and therefore it is validated by comparison to DST-measured CO_2 concentrations. For cases where the partial pressures of a trace gas become closer to the total pressure, chemical equilibrium with the aqueous phase is computed correctly, but the gas pressure will be underestimated in the mass-balance equation solved for gas flow. Because CO_2 concentrations encountered in the DST and model simulations are generally less than a few percent, and rarely over 10%, this model for the gas species is a reasonable approximation for this particular system (see Section 6.4.6).

6.4.2 Kinetic Rate Laws

Rates of mineral dissolution and precipitation close to equilibrium can be described via a relationship of the rate to the saturation index (Q/K), as follows (Steefel and Lasaga 1994 [101480], p. 540):

$$Rate(mol\ s^{-1}kg^{-1}_{water}) = \mathrm{sgn}\left[\log\left(Q/K\right)\right] kA \prod_i a_i^p \left[\left(Q/K\right)^m - 1\right]^n \qquad \text{(Eq. 6.4-5)}$$

where a_i is the activity of each inhibiting or catalyzing species, and p is an empirically determined exponent and the variable A is the reactive surface area expressed in units of $m^2_{mineral}/kg_{water}$. The rate constant k (in mol m^{-2} s^{-1}) is given as (Steefel and Lasaga 1994 [101480], p. 541):

$$k = k_0 \exp\left[\frac{-E_a}{R}\left(\frac{1}{T} - \frac{1}{298.15}\right)\right] \qquad \text{(Eq. 6.4-6)}$$

where the temperature dependence of reaction rate is related to the activation energy (E_a) in units of kJ/mol and T is the temperature in Kelvin units. Following Steefel and Lasaga (1994 [101480], p. 568), by neglecting the effect of pH or other aqueous species activities on reaction rates, we set p=0 for each species so that the product $\prod_i a_i^p = 1$ has been eliminated from Equation 6.4-5. The ratio of the species activity product (Q) and the equilibrium constant (K) describes the extent to which a mineral is in disequilibrium with a given solution composition. For Q/K equal to one, the mineral is at equilibrium, and thus the net rate of reaction becomes zero. For Q/K greater than one, the mineral is oversaturated and thus the rate becomes negative. The expression "*sgn [log(Q/K)]*" ensures that the correct sign is enforced when the exponents m and n are not equal to one. The variable A is the reactive surface area expressed in units of $m^2_{mineral}/kg_{water}$. In the case of ideal solutions, the saturation index of the solid solution is calculated as the sum of the saturation indices of the individual endmembers, and the reaction rate of the solid solution is calculated as described in Wang 2003 ([161665], SN-LBNL-SCI-112-V2, pp. 37–40).

Carroll et al. (1998 [124275], p. 1379) noted that the calculated rates of amorphous silica precipitation, based on Rimstidt and Barnes (1980 [101708], p. 1683), are about three orders of magnitude lower than those observed in geothermal systems. Carroll et al. (1998 [124275], p. 1379) presented experimental data on amorphous silica precipitation for more complex geothermal fluids at higher degrees of supersaturation, and also for a near-saturation simple fluid chemistry. Under far from equilibrium conditions, the rate law for amorphous silica precipitation has been expressed as (Carroll et al. 1998 [124275], p. 1382):

$$Rate(mol\ s^{-1}kg_{water}^{-1}) = kA\left(Q/K\right)^{m} \quad \text{(Eq. 6.4-7)}$$

This rate does not tend to zero as Q/K goes to one, and therefore a modification was made to this law so that it tends to zero as Q/K approaches one (described in Wang 2003 ([161665], SN-LBNL-SCI-109-V1, p. 45), as follows:

$$Rate(mol\ s^{-1}kg_{water}^{-1}) = kA\left[\left(Q/K\right)^{m} - \frac{1}{\left(Q/K\right)^{2m}}\right] \quad \text{(Eq. 6.4-8)}$$

Over a finite time step (Δt), the change in the concentration of each primary species j on account of mineral precipitation or dissolution under kinetic constraints is computed from the sum of the rates, r_i, of all j-containing minerals i as follows:

$$\Delta C_j = -\sum r_i \nu_{ij} \Delta t \quad \text{(Eq. 6.4-9)}$$

where ν_{ij} is the stoichiometric coefficient of component j in mineral i. These concentration changes are incorporated into the mass-balance equation of each primary species involved in mineral reactions, using Equations 6.4-5 through 6.4-7, and solved simultaneously with the concentrations of all primary species.

6.4.3 Fracture and Matrix Mineral Reactive Surface Areas

6.4.3.1 Fracture Mineral Reactive Surface Areas

Reactive surface areas of minerals on fracture walls were calculated from the fracture-matrix interface area/volume ratio, the fracture porosity, and the derived mineral volume fractions. The fracture-matrix interface areas and fracture porosities for each unit were taken from appropriate calibrated properties sets (Table 4.1-1). These areas were based on the fracture densities, fracture porosities, and mean fracture diameter. The wall of the fracture is treated as a surface covered by mineral grains having the form of uniform hemispheres. The grain diameter and spatial density are not included in this calculation, so that the area is actually only marginally greater than the fracture geometric surface area. An alternative method to approximating the surface area in excess of the geometric area would be to include a roughness factor. The geometric surface area of the fracture wall can be approximated by:

$$A_r = \frac{\pi A_{f\text{-}m}}{2\phi_{f\text{-}m}} \quad \text{(Eq. 6.4-10)}$$

where, A_r is the reactive surface area ($m^2 / m^3_{\text{fracture medium}}$), $A_{f\text{-}m}$ is the fracture-matrix interface area/volume ratio ($m^2_{\text{fracture}} / m^3_{\text{fracture+matrix}}$ volume), and $\phi_{f\text{-}m}$ is the fracture porosity of the rock. $A_{f\text{-}m}$

is the surface area used as input to the model simulations as an approximation of the reactive surface area. This model for the fracture surface area considers that the areal coverage is approximately equivalent to the mineral volume fraction. A further modification, which was implemented in TOUGHREACT V2.3 (LBNL 2001 [153101]), relates the 3-D cross-sectional area to the 2-D surface area in the fracture, which yields a factor of 3/2, i.e., an increase of 50% in the reactive surface area. This relation was used for all DST THC Model REV01 sensitivity studies, Tptpmn, and Tptpll THC simulations, discussed in Sections 6.4–6.6.

The reactive surface area of each mineral (in units of $m^2_{mineral}/kg_{water}$) used in Equations 6.4-5 and 6.4-8 is then given by:

$$A_i\ (m^2/kg_{water}) = \frac{A_r f_i}{\rho_w \phi_f} \qquad \text{(Eq. 6.4-11)}$$

where f_i is the volume fraction of the mineral in the mineral assemblage, ρ_w is the density of water (taken as a constant 1,000 kg/m^3), and ϕ_f is the porosity of the fracture medium, as opposed to the fracture porosity of the rock. This is the surface area/water mass ratio for a mineral in a liquid-saturated system. Calculated volume fractions of minerals are tabulated in Attachments I and II.

To provide the correct rock/water ratio in an unsaturated system, the form of this surface area can be written as:

$$A_i\ (m^2/kg_{water}) = \frac{A_r f_i}{\rho_w \phi_f S_w} \qquad \text{(Eq. 6.4-12)}$$

where S_w is the water saturation. However, as S_w goes to zero, the reactive surface area would tend to infinity. Clearly, at a very low liquid saturation, the surface area of the rock contacted by water is likely much smaller than the total area.

Two methods have been implemented to address this phenomenon. The first method considers that the surface area contacted by water diminishes proportionately to the saturation. This yields the saturated surface area given by Equation 6.4-10. The second method employs the active-fracture-model concept (Liu et al. 1998 [105729], pp. 2636–2638) modified to consider water-rock reactions taking place below the residual saturation. The form of the active fracture parameter for reaction is then given by the following set of equations:

$$S_{ar} = (S_w - S_m)/(1 - S_m) \qquad \text{(Eq. 6.4-13)}$$

$$a_{fmr} = S_{ar}^{(1+\gamma)} \qquad \text{(Eq. 6.4-14)}$$

where S_m is the minimum liquid saturation for which water-rock reactions are considered and S_{ar} is the effective saturation available for reaction. The active fracture parameter, γ, is obtained from the calibrated hydrological property set (DTN: LB990861233129.001 [110226]). The factor that reduces the surface area contacted by the water phase is given by a_{fmr}. In all simulations S_m is set to the very small saturation of 1×10^{-4} or 1×10^{-5} to ensure that reactions take place until virtually no water is left (e.g., during dryout via ventilation or heating). Finally, the reactive surface area, using this modified form of the active fracture model, is given by:

$$A_i(\mathrm{m}^2/\mathrm{kg}_{\mathrm{water}}) = \frac{A_r a_{fmr}}{\rho_w \phi_f S_w} \qquad \text{(Eq. 6.4-15)}$$

The surface area calculated in this way is applicable only to reactions taking place in the fracture medium and is used directly in Equations 6.4-5 and 6.4-8. Note that this area is not comparable to the input surface areas that are listed in Attachments III and IV.

In the dual permeability method, the porosity of the fracture medium can be taken as 1.0; however, for modeling of mineral dissolution and precipitation, there would then be no rock to dissolve. Because the dissolution rates of many minerals are quite slow at temperatures below 100°C, only a small volume of rock adjoining the open space of the fracture needs to be considered as the starting rock fraction. In the DST THC REV01 and Tptpmn THC REV01 models, the porosity of the fracture medium was set to 0.99, thus making available 1% of the total fracture volume for reaction. In the Tptpll THC Model (REV01 and REV02) and other REV02 models, the fracture medium porosity was set to 0.5 (Section 6.4.6.1).

6.4.3.2 Matrix Mineral Reactive Surface Areas

Mineral surface areas in the rock matrix (Attachments III and IV) were taken from DTNs shown in Table 4.1-1. These values were estimated using the geometric area of a cubic array of truncated spheres that make up the framework of the rock. Clay minerals are considered as coatings of plate-like grains. The mineral surface areas of framework grains (truncated spheres) in contact with the open pore space are calculated using an initial grain diameter, followed by successive truncation of the grains in the vertical direction until the porosity of this system is close to the measured porosity of the rock. In the welded tuff, crystals are often tightly intergrown with little or no pore space within the aggregate. Thus, a check is made so that the resultant mean pore throat size and spacing yields a permeability (from a modified Hagen-Poiseuille relation (Ehrlich et al. 1991 [117799], p. 1582, Equation 11)) that is relatively close to the measured saturated permeability.

The grains forming the framework of this rock are considered to be the primary high-temperature phases of the tuff (i.e., quartz, cristobalite, tridymite, and feldspars). The abundance of secondary phases (i.e., those that formed as alteration products or low-temperature coatings on the primary assemblage), such as clay minerals, are used to reduce the free surface area of the framework grains. The surface areas of the secondary phases are approximated using a tabular morphology.

6.4.4 Effects of Mineral Precipitation/Dissolution on Hydrological Properties

6.4.4.1 Porosity Changes

Changes in porosity and permeability resulting from mineral dissolution and precipitation have the potential to modify percolation fluxes and seepage fluxes at the drift wall. In this analysis, porosity changes in matrix and fractures are directly tied to the volume changes that result from mineral precipitation and dissolution. The molar volumes of hydrous minerals, such as zeolites and clays, created by hydrolysis reactions with anhydrous phases, such as feldspars, are commonly larger than those of the primary reactant minerals. Therefore, constant molar dissolution-precipitation reactions can lead to porosity reductions. These changes are taken into account in this analysis. The porosity of the medium (fracture or matrix) is given by

$$\phi = 1 - \sum_{m=1}^{nm} fr_m - fr_u \qquad \text{(Eq. 6.4-16)}$$

where nm is the number of minerals, fr_m is the volume fraction of mineral m in the rock ($V_{mineral}/V_{medium}$, including porosity), and fr_u is the volume fraction of nonreactive rock. As the fr_m of each mineral changes, the porosity is recalculated at each time step. The porosity is not allowed to go below zero.

6.4.4.2 Fracture Permeability Changes

Fracture permeability changes can be approximated using the porosity change and considering plane parallel fractures of uniform aperture (cubic law—Steefel and Lasaga 1994 [101480], p. 556). If the fracture spacing and density remain constant, the updated permeability, k, is given by

$$k = k_i \left(\frac{\phi}{\phi_i} \right)^3 \qquad \text{(Eq. 6.4-17)}$$

where k_i and ϕ_i are the initial permeability and porosity, respectively. This law yields zero permeability only under the condition of zero fracture porosity.

In most experimental and natural systems, permeability reductions to values near zero occur at porosities significantly greater than zero. This generally is the result of mineral precipitation preferentially closing the narrower interconnecting apertures. The hydraulic aperture, as calculated from the fracture spacing and permeability (as determined through air-permeability measurements) using a cubic law relation, is a closer measure of the smaller apertures in the flow system. Using the hydraulic aperture, a much stronger relationship between permeability and porosity can be developed. This relationship can be approximated as follows:

The initial hydraulic aperture $b_{0,h}$ (m) is calculated using the following cubic law relation:

$$b_{0,h} = [12 k_0 s]^{1/3} \qquad \text{(Eq. 6.4-18)}$$

where k_0 is the initial fracture permeability (m^2) and s is the fracture spacing (m) for a single fracture set. The permeability (k') resulting from a change in the hydraulic aperture is given by

$$k' = \frac{(b_{0,h} + \Delta b)^3}{12s} \quad \text{(Eq. 6.4-19)}$$

where Δb is the aperture change resulting from mineral precipitation/dissolution. The aperture change resulting from a calculated volume change can be approximated by assuming precipitation of a uniform layer over the entire geometric surface area of the fracture, assuming also that this area (as well as the fracture spacing) remains constant. In geologic systems, the actual distribution of mineral alteration is much more heterogeneous and depends on many factors that are active at scales much smaller than the resolution of the model. The combined effect of the initial heterogeneities and localized precipitation processes can only be treated through model sensitivity studies and experiments. The initial aperture available for precipitation (b_g, the geometric, rather than the hydraulic, aperture) can be calculated (Attachment XI) from the ratio of the initial fracture porosity ($\phi_{f,0}$) to the fracture surface area (A_f), as follows:

$$b_g = \phi_{f,0} / A_f \quad \text{(Eq. 6.4-20)}$$

For a dual-permeability model, changes in the fracture porosity are calculated based on the porosity of the fracture medium, so that Δb can be approximated by

$$\Delta b = \frac{(\phi'_{fm} - \phi_{fm,0})}{\phi_{fm,0}} b_g \quad \text{(Eq. 6.4-21)}$$

Equations 6.4-18, 6.4-19, and 6.4-21 were implemented in TOUGHREACT V2.3 (LBNL 2001 [153101]) with input parameters of b_g and s. This relation was used for sensitivity studies on the Tptpmn THC Model simulations (heterogeneous and homogeneous permeability fields), DST THC REV01 and REV02 Model simulations, and Tptpll THC Model simulations.

6.4.4.3 Matrix Permeability Changes

Matrix permeability changes are calculated from changes in porosity using ratios of permeabilities calculated from the Carmen-Kozeny relation (Bear 1988 [101379], p. 166, Equation 5.10.18, symbolically replacing n by ϕ), and neglecting changes in grain size, tortuosity, and specific surface area as follows:

$$k = k_i \frac{(1-\phi_i)^2}{(1-\phi)^2} \left(\frac{\phi}{\phi_i}\right)^3 \quad \text{(Eq. 6.4-22)}$$

6.4.4.4 Effects of Permeability and Porosity Changes on Capillary Pressures

Changing permeability and porosity also results in changes in the unsaturated flow properties of the rock. These effects are treated by modifying the calculated capillary pressure (Pc) using the Leverett scaling relation (Slider 1976 [128146], p. 280) to obtain a scaled Pc' as follows:

$$Pc' = Pc\sqrt{\frac{k_i\phi}{k\phi_i}} \qquad \text{(Eq. 6.4-23)}$$

Simulations performed with TOUGHREACT V3.0 (LBNL 2002 [161256]) have the maximum value of Pc' (in Eq. 6.4-23) limited by the cutoff prescribed in the input file. All simulations done using earlier TOUGHREACT versions have the cutoff apply to Pc (not Pc') in Eq. 6.4-23 unless an extrapolation in the Pc-saturation curve was performed, in which case no cutoff was applied. Capillary pressure cutoff values used in various model revisions are discussed in Section 6.4.6.1 (approximation no. 15).

6.4.5 Mineral Precipitation in Dry Gridblocks

In certain cases of evaporation or boiling, a gridblock may experience an influx of water that evaporates completely during the solution of the flow equations. After the flow equations are solved, TOUGHREACT solves the transport equations followed by the speciation and reaction equations. The speciation and reaction equations require that the gridblock is "wet,"—that is, the liquid saturation is greater than zero (or a small value). Because of the lack of water in the gridblock, a method was developed for storing all residual aqueous species in a solid "salt" assemblage.

The amount of solute "stored" is simply the product of the concentration in the upstream gridblock and the flux of water into the gridblock that dries out. Also, any water that is initially present in the gridblock, and dries out, gives rise to some solute mass that is transformed into solid phases. For these cases, the mass of each primary solute species is saved and may be assigned to minerals in a prescribed order in the chemical input file. This approximation is performed so that solute mass loss is minimized and most of the solute mass can be accounted for in a solid mineral phase. Simulations performed with TOUGHREACT V2.4 (LBNL 2001 [160880]) and V3.0 (LBNL 2002 [161256]) have this option, whereas V2.2 (LBNL 1999 [153219]) and V2.3 (LBNL 2001 [153101]) do not.

In the simulations presented in this Model Report (REV02), for the specific cases when water flows into gridblocks that dry out in the flow calculation (by boiling or evaporation), the following solid phases are formed, stoichiometrically and in the following order: silica, calcite, gypsum, hematite, fluorite, $NaNO_3$, K_2SO_4, Na_2SO_4, $MgSO_4$, halite, and sylvite. The order is predetermined (i.e., nitrates are formed before chlorides) to ensure nitrate mass is not lost in cases where insufficient sodium remains to form $NaNO_3$ (in the absence of other nitrate salts that could have formed). The goal, here, is not to model evaporation accurately but to save as much mass of the dissolved constituents as possible for gridblocks that completely dry out.

Upon rewetting, the salt minerals (i.e., $NaNO_3$, K_2SO_4, Na_2SO_4, $MgSO_4$, halite, sylvite) are assumed to dissolve kinetically with a relatively fast rate constant (set here at 10^{-6} mol/m^2/s) and

a dissolution rate limited by their solubility (Section 6.4.2). The salt solubilities were taken from the data0.ymp.R2 database (DTN: MO0302SPATHDYN.000 [161756]), except that $NaNO_3$ (not in that database) was given the solubility of KNO_3 in that database. Therefore, this model captures the general behavior of salt dissolution as the boiling front recedes. However, the predicted major ion concentrations during the short time when these salts dissolve are approximate, because the identity of the salt phases is not based on a thermodynamic speciation/precipitation model, and their dissolution rates are only approximate.

6.4.6 Principal Model Approximations and Approaches

6.4.6.1. General Approximations in the Modeling of THC Processes

1. The rock is described by a dual-permeability model (Section 6.2.1.5), which considers separate but interacting fracture and matrix continua, each with specified permeabilities. In the dual-permeability model, the fracture continuum is considered as co-located but interacting with the matrix continuum, in terms of the flow of heat, water, and vapor through advection, diffusion, and conduction (for heat). The aqueous and gaseous species are transported via advection and molecular diffusion between the fractures and matrix. Each continuum has its own well-defined initial physical and chemical properties. The dual-permeability approach for modeling physical processes in fractured porous media is discussed in detail in Doughty (1999 [135997], pp. 76–77). This approach is validated by comparing geochemical data obtained from the DST to results of simulations of the DST (Section 7.1). It is also further validated in BSC (2003 [161530], Section 7).

2. The mass of minerals precipitated is small and its thermal properties are similar to those of the host rock. Therefore, the thermal properties are not modified to account for precipitated minerals.

3. The infiltrating water and the fracture water are set to the same chemical composition as the matrix pore-water samples that were collected (Table 6.2-1). The rationale for this modeling approach is given in Section 6.2.2.1.

4. Effects of changes in the partial pressure of CO_2 (resulting from heating, water reaction with calcite, and gas-phase transport) on the density of the gas phase are neglected. This is justified because, in this study, CO_2 generally accounts for less than 5% and always less than 10% of the gas phase volume (air, water, and CO_2). Although the molecular weight of CO_2 is greater than that of air (approximately 44 g/mol versus 29 g/mol), the density is only increased proportionally to the volume fraction of CO_2 and the ratio of the molecular weights. This would result in a density increase of about 5% for a gas with a CO_2 volume fraction of 10%. These conditions make the effect of evolved CO_2 on the physical properties of the gas phase negligibly small and justify the use of this approximation. The effect of CO_2 on the density of steam (molecular weight approximately 18 g/mol) would be somewhat greater, however increases in the steam fraction accompanying boiling would tend to dilute the CO_2 fraction.

5. The effects of changes in water chemistry on the water density and viscosity are neglected. This approximation is justified because aqueous-species concentrations are low in waters at most values of the liquid saturation (in the rock matrix or fractures). In cases where concentrations are significantly higher, the liquid saturation is generally much less than 1%. Therefore, the liquid is nearly immobile because of the very small relative permeability for the liquid phase under such conditions.

6. Diffusion coefficients of all aqueous species are set to the same value (the value for the chloride anion; see Section 4.1.6). This is justified because the tracer diffusion coefficients of aqueous species differ by at most about one order of magnitude, with many differing by less than a factor of 2 (Lasaga 1998 [117091], p. 315). The strong effects of water-rock interaction, boiling condensation, and rapid fracture drainage overwhelm effects of aqueous species diffusion.

   Diffusion coefficients for gases are calculated. In the gas phase, CO_2 is the only transported reactive species (other than H_2O vapor). For an ideal gas, the tracer diffusion coefficient of a gaseous species can be expressed as a function of temperature and pressure in the following form (Lasaga 1998 [117091], p. 322):

$$D = \frac{RT}{3\sqrt{2}\pi P N_A d_m^2}\sqrt{\frac{8RT}{\pi M}} \qquad \text{(Eq. 6.4-24)}$$

   where

   D = diffusion coefficient (m^2/s)
   R = gas constant (8.31451 m^2 kg s^{-2} mol^{-1} K^{-1})
   T = temperature in Kelvin units
   P = pressure (kg m^{-1} s^{-2})
   N_A = Avogadro's number (6.0221367×10^{23} mol^{-1})
   d_m = molecular diameter (m)
   M = molecular weight (kg/mol)

   The CO_2 diffusion coefficient is calculated using input values of d_m and M (Section 4.1.6).

7. Mineral precipitation or dissolution is modeled to occur uniformly over the smooth plane-parallel fracture walls (Section 6.4.4.2). However, mineral precipitation could be non-uniform, leading to a different relationship between changes in permeability and porosity. This approximation can be justified by the use of bulk permeabilities and porosities that initially account for the net effect of variability in fracture aperture at a macroscopic scale. Furthermore, effective (hydraulic) apertures are used instead of true apertures, the latter being much larger (Section 6.4.4.2). As a result, the permeability change is quite sensitive to porosity changes (in this study, a 10–14% drop in fracture porosity leads to zero permeability in fractures in the modeled repository units).

8. CO_2 gas is treated as an ideal gas (i.e., obeys the ideal gas law and its partial pressure equals its fugacity). This approximation is valid for the low ambient pressures (near atmospheric) considered in this study (Langmuir 1997 [100051], p. 15).

9. Except for smectites, the chemical and physical properties of minerals that form solid solutions are approximated by their individual endmember compositions and properties. Because smectite endmembers are (individually) near equilibrium with pore waters, some of the smectite endmembers could be calculated to precipitate while others dissolve. For this reason, an ideal solid-solution model is implemented for smectite (Na, Ca, and Mg endmembers), with each endmember's activity equaling its mole fraction. Treating the smectite as a solid solution, results in individual smectite endmembers either all dissolving or all precipitating, providing a better physical representation of dissolution/precipitation processes. Feldspar solid solutions are not considered because albite (Na-feldspar) and anorthite (Ca-feldspar) are generally strongly undersaturated in the simulations, and thus their dissolution rates are governed primarily by the kinetic-rate constant rather than the saturation index (Equation 6.4-5). In addition, nearly pure secondary K-feldspar compositions are observed in geothermal systems (Stefánsson and Arnórsson 2000 [153578], p. 2578). Therefore, the precipitation of secondary K-feldspar can be approximated fairly well with a pure endmember. These approximations are further validated by comparison of model results to measured water chemistry in the DST (Section 7.1) and in a plug-flow reactor experiment (Section 7.2).

10. The fracture continuum is modeled with grid blocks having an initial fraction of void space less than one (0.99 in the DST THC REV01 Model and Tptpmn THC REV01 Model, and 0.5 in the Tptpll THC REV01 and REV02 models). These values are chosen such that that the fracture medium always contains solids that can react with fluids in fractures. It is verified that there is always enough solid initially present in the fracture continuum to avoid the possibility that some of the primary rock forming minerals become exhausted (through dissolution). Note that the volume of each grid block assigned to the fracture continuum is then calculated in such a way that the true fracture porosity (i.e., the fraction of the bulk rock occupied by fracture void space) is always reproduced.

11. The thermal conductivities of fracture and matrix gridblocks are calculated assuming a linear interpolation between dry and wet conductivities as a function of liquid saturation. These are the thermal conductivities for the solid + fluid system. For fractures, thermal conductivities are multiplied by the fracture porosity to account for the correct fracture-to-fracture connection area in calculations of heat conduction (i.e., this is needed because full gridblock areas are input into the model). Fracture thermal conductivities are also multiplied by 0.1 (an arbitrary value less than 1) to account for the limited spatial continuity and connectivity between fracture gridblocks. The volume of the fracture continuum is, however, only a small fraction of the matrix continuum. Therefore heat conduction occurs primarily through the matrix continuum and, as a result, the model is not sensitive to the amount of heat conduction in fractures.

12. In REV01 simulations (Sections 6.5–6.7), vapor-pressure lowering due to capillary pressure (the Kelvin effect) is neglected. This effect is taken into account in simulations carried out for this current model revision (REV02) (Section 6.8 and 7.1). The impact of including or neglecting this effect is evaluated in Section 6.8.5.3.

13. Upon boiling or evaporation, the aqueous phase is treated as unreactive and is not concentrated further, once its ionic strength reaches an input upper limit of 4 or if the liquid saturation drops below an input lower limit of 10^{-4} to 10^{-5}. This ensures that the calculated ionic strength remains within the range of applicability of activity coefficient models (Section 6.4.1). Past these limits, different schemes are implemented in the various model revisions, as discussed below.

    In REV01 simulations (Sections 6.5–6.7), concentrations of aqueous species are saved (unchanged) during dryout and become available again for reaction at the time of rewetting, when the liquid saturation increases and the ionic strength decreases. This scheme has the effect that all salts that would precipitate from the point of the liquid saturation or ionic-strength limits (up to the point of complete dryout) would instantly redissolve upon rewetting.

    In REV02 simulations (Sections 6.8 and 7.1), solid phases are formed during dryout as described in Section 6.4.5. These solid phases are then available for dissolution upon rewetting (using a fast dissolution rate arbitrarily set at 10^{-6} mol s^{-1} kg_{H2O}^{-1}).

    At liquid saturations as small as 10^{-5}, the total amount of dissolved mass present in any given model gridblock is exceedingly small. Thus, ignoring chemical reaction for such small mass amounts (and over a limited time period) does not significantly affect the general computed trends of aqueous phase concentrations and precipitated mineral amounts over long periods of time and a wide range of liquid saturations.

14. Hydrogeologic rock properties in each hydrogeologic unit of the model are approximated as being laterally homogeneous, except in the Tptpmn Heterogeneous THC Model (Section 6.6). Results of the Tptpmn Heterogeneous THC Model (Section 6.6.2), including the natural heterogeneity in fracture permeability (4 orders of magnitude), do not show significantly different water chemistry in either space or time when compared to the homogeneous model (Section 6.5.5). Furthermore, good comparisons are obtained between modeled and measured water and gas chemistry for the DST (Section 7.1).

15. The capillary pressure in both fractures and matrix must reach some maximum, finite value upon complete dryout (zero liquid saturation). In REV01 simulations (Sections 6.5–6.7), for fractures and matrix in the Tptpmn, Tptpll, and Tptpln lithostratigraphic units (model units tsw34, tsw35, and tsw36, respectively), the limit is set by the calculated slope of the P_{cap} versus liquid saturation curve at a liquid saturation value equal to $S_r + \varepsilon$, with S_r being the residual saturation, and $\varepsilon = 0.01$ (Table 6.4-1). In these units, this results in maximum P_{cap} values of 10^{11}–10^{13} Pa in the matrix, and 10^{3}–10^{4} Pa in fractures. In other hydrogeologic units, in REV01 simulations, the limit is set to 10^{10} Pa by default. For the matrix, these values exceed the maximum tensile

strength of water (on the order of 10^8 Pa; e.g., Mercury and Tardy 2001 [161130]), and were therefore lowered in subsequent REV02 simulations.

In REV02 simulations (Sections 6.8 and 7.1), the default limit is set to 10^8 Pa. For fractures and matrix in the Tptpmn, Tptpll, and Tptpln lithostratigraphic units (model units tsw34, tsw35, and tsw36, respectively), the limit is set, as previously, by the calculated slope of the P_{cap} versus liquid saturation curve at a liquid saturation value equal to $S_r + \varepsilon$. For these units, ε values for the matrix yield maximum P_{cap} values of 10^8 Pa (Table 6.4-1); for fractures, ε is set to 0.01 as done for REV01 simulations (maximum P_{cap} values around 10^3–10^4 Pa).

The unrealistic maximum P_{cap} values used in REV01 previous do not have much effect on simulation results because vapor-pressure lowering (due to capillary pressure) is neglected in these simulations. Low values of maximum capillary pressures in fractures are justifiable, on the basis that the capillary suction in fractures is orders of magnitude less than in the rock matrix.

16. Open spaces in the drift are approximated as a porous medium with a large permeability (10^{-10} m^2) greater than in surrounding rocks, but not so large as to create numerical difficulties when computing flow. In addition, these open spaces are modeled with no capillarity, a unit porosity, and no residual saturation except directly against the drift wall (arbitrary small value of 0.01 to account for some water condensation, if any, against the drift wall). These approximations are made because the mathematical model is not formulated to handle fluid flow in non-porous media.
17. The fracture tortuosity value (0.7) (Section 4.1.6) is based on models of *in situ* testing data (DTN: LB991091233129.006 [111480]) and also corresponds to the highest tortuosity given by de Marsily (1986 [100439], p. 233), with the rationale that fracture tortuosity should be high compared to matrix tortuosity (i.e., less tortuous path in fractures than in the matrix). This fracture tortuosity was modified for fracture-fracture connections by multiplication of the tortuosity by the fracture porosity of the bulk rock. This operation yields a better approximation for the fracture-to-fracture interconnection area (only for calculation of diffusive fluxes; the entire gridblock connection area is used for calculating advective fluxes, because the bulk fracture permeability of the entire gridblock is entered into the model).

6.4.6.2 Approximations Specific to the THC Seepage Model

1. For the Tptpmn and Tptpll THC Model REV01 simulations (Sections 6.5–6.7), the drift wall is always closed to fluid fluxes except for gaseous CO_2 diffusive fluxes. The latter are limited because the drift, as modeled, is closed at each end. Therefore, the drift has a finite volume that is small compared to the near-field rock volume. If chemical reactions inside the drift do not take place to a large extent, the effect of exchange of components with the near-field environment would have little effect on near-field THC processes. There are further reasons for closing the drift to advective fluid fluxes. First, our objective is to calculate the water and gas compositions that reach the drift wall, and not THC processes in the drift itself (in-drift THC processes are considered in other model reports). Processes in the rock outside the drift are the most likely to govern compositions of aqueous liquids and gases entering the drift.

Second, for a homogeneous fracture system with constant vertical infiltration (from the top model boundary), the wall acts as a capillary barrier and water cannot seep into the drift even with an open drift and infiltration rates much larger than considered here. In this case, water fluxes into the drift could be conservatively approximated as the liquid fluxes very close to the drift wall.

For REV02 simulations, the drift wall is open to all fluid fluxes. No specific boundary conditions of pressure, relative humidity, or gas compositions are applied inside the drift (i.e., as if the repository were sealed off, and neglecting sources or sinks of CO_2 due to microbial activity or atmospheric CO_2). Computing fluid flow through open spaces of the drift using a model designed to calculate flow through porous media is by itself a very coarse approximation. Thus, modeling the drift wall as either open or closed to advective fluid flow are equally coarse approximations. However, the scope of this Model Report is to model THC processes in the near-field outside the drift and not in the drift itself. Comparisons between these alternatives are presented in Section 6.8. Note that for the open drift case (REV02), the invert is allowed to react with any water present in it (pore water or condensation).

2. The initial composition of water in fractures is taken to be the same as in the rock matrix throughout the model domain. Also, this initial water composition is set to be the same in all hydrogeologic units. Justifications for this modeling approach are provided in Section 6.2.2.1.

6.4.7 Summary of Hydrological and Thermal Properties

The hydrological and thermal properties of repository units used in simulations presented in the following sections of this report are summarized in Table 6.4-1. Sources of properties used for all modeled hydrogeological units and other input data are listed in Section 4.1 and 6.4.8.

6.4.8 Sources of Additional Model Inputs Used in Sensitivity Analyses

This section describes model inputs used for simulations considered as sensitivity analyses and which were not used for TSPA-LA. All direct input data and technical information used for simulations feeding TSPA-LA are summarized in Section 4.1. Data used for model validation are presented in Section 7. Sources of model input data used to evaluate model sensitivity, if different from data listed in Sections 4.1 and 7, are discussed below and summarized in Table 6.4-2.

6.4.8.1 Sensitivity to Historical (REV01) Model Inputs

Results of historical simulations carried out for REV01 of this report are presented in this report revision (REV02) in Sections 6.5, 6.6, and 6.7. These REV01 simulations provide useful information to assess the sensitivity of the THC Seepage Model to various input data and model improvements from REV01 to REV02. Sources of historical data for these simulations are shown in Table 6.4-2. For convenience, REV01 mineralogical data are listed in Attachments I and III, REV01 thermodynamic data in Attachment V, and REV01 kinetic data in Table 6.4-3.

6.4.8.2 Thermodynamic Data Sensitivity (REV02)

Simulations of "ambient" conditions (i.e., without thermal loading, under natural geothermal gradient, and without drift opening) were run using alternative thermodynamic data sets to evaluate the model sensitivity to these data (Section 6.8.5.1) and to justify the thermodynamic data (Set 1, below) selected for other REV02 simulations in this report. For these ambient simulations, the following three sets of data were used:

Set 1

This is the thermodynamic data set adopted for all REV02 simulations (DTN: LB0307THMDBRTM.001 [164434]) (Attachment VI) and discussed in Section 4.1.4.

Set 2

This thermodynamic data set contains all data from the YMP thermodynamic database data0.ymp.R2 (DTN: MO0302SPATHDYN.000 [161756]), except for necessary changes to data for a few minerals (not prevalent in the vicinity of the drift) as described below (see also Wang 2003 [161665], SN-LBNL-SCI-141-V2, pp. 158–160).

Heulandite in database data0.ymp.R2 contains significant amounts of barium and strontium. These chemical components are not considered in this study. For this reason, the data from database data0.ymp.R2 for heulandite could not be used. Instead, log(K) values used in Set 2 for heulandite were taken as the uncorrected log(K) values given in DTN: LB0307THMDBRTM.001 [164434] ("heuland/10" in Attachment VI). The source of these data and the calculation methods are the same as those used for the stellerite log(K) values in the data0.ymp.R2 database (DTN: MO0302SPATHDYN.000 [161756]).

Log(K) values for sepiolite are not given in database data0.ymp.R2 for temperatures above 100°C. For this reason, sepiolite log(K) values were taken from an earlier revision of this database (DTN: MO0204SPATHDYN.000 [158910]), containing sepiolite data consistent with the data in Set 1 above.

For clinoptilolite, log(K) values were taken for the mineral identified as clinoptilolite-Ca in database data0.ymp.R2, because this phase has a similar composition to the phase used in Set 1. However, this phase contains a very small amount of iron, which is not included in the clinoptilolite in Set 1. By using this phase, the already very small amount of iron in the aqueous phase was completely depleted, causing chemical convergence problems in simulations. For this reason, iron was removed from this phase. It was not deemed necessary to recompute log(K) values because the amount of iron in this phase is very small (approximately 0.1% stoichiometric proportion of Fe relative to Si).

No other changes were made to the data0.ymp.R2 database for Set 2. For calcium, magnesium, and sodium smectites, the phases identified as montmorillonite-Ca, montmorillonite-Mg, and montmorillonite-Na in the data0.ymp.R2 database were used. For potassium feldspar, the phase identified as maximum_microcline was used. Glass data from Set 1 were included in Set 2 because no glass data are included in the data0.ymp.R2 database. Note that if a mineral was specified with different unit cell stoichiometries in Set 1 and Set 2 (i.e. some clays and zeolites),

the kinetic rate of that mineral (Section 4.1.5) was corrected to account for the same stoichiometric Si release (or consumption) per unit time, for consistency between data sets.

Set 3

This set is identical to Set 2 (data0.ymp.R2 database), except that all zeolite thermodynamic data were taken from Set 1 (minerals identified as "mord/10-r02", "heul/10-r02", "stell/10-r02", and "clpt/10-r02 in Attachment VI").

Table 6.4-1 Summary of Hydrological and Thermal Properties of Repository Units

		REV01				REV02			
Model Layer > *Lithostratigraphic Unit >*		*tsw33* *Tptpul*	*tsw34* *Tptpmn*	*tsw35* *Tptpll*		*tsw33* *Tptpul*	*tsw34* *Tptpmn*	*tsw35* *Tptpll*	
MATRIX DATA					**DTN:**				**DTN:**
permeability	k_m (m^2)	3.08E-17	4.07E-18	3.04E-17	LB990861233129.001	6.57E-18	1.77E-19	4.48E-18	LB0208UZDSCPMI.002
porosity	ϕ_m	0.154	0.110	0.131	LB990861233129.001	0.1425	0.1287	0.1486	LB0210THRMLPRP.001
van Genuchten α	α_m (1/Pa)	2.13E-5	3.86E-6	6.44E-6	LB990861233129.001	6.17E-6	8.45E-6	1.08E-5	LB0208UZDSCPMI.002
van Genuchten m (or λ)	m_m	0.298	0.291	0.236	LB990861233129.001	0.283	0.317	0.216	LB0207REVUZPRP.002
residual saturation	S_{irm}	0.12	0.19	0.12	LB990861233129.001	0.12	0.19	0.12	LB0207REVUZPRP.002
satiated saturation	S_{ism}	1.00	1.00	1.00	LB990861233129.001	1.00	1.00	1.00	LB0207REVUZPRP.002
epsilon (for max P_{cap})	ε	0.01	0.01	0.01	(Section 6.4.6.1)	0.138	0.091	0.216	Yield maximum P_{cap} = 10^8 Pa (Section 6.4.6.1)
rock grain density	ρ_g (kg/m^3)	2510	2530	2540	LB990861233129.001	2358	2466	2325	LB0210THRMLPRP.001
rock grain specific heat	Cp (J/kg-K)	882	948	900	LB990861233129.001	985	985	985	LB0210THRMLPRP.001
dry conductivity	λ_{dry} (W/m-K)	0.79	1.56	1.20	LB990861233129.001	1.164*	1.419*	1.278*	LB0210THRMLPRP.001
wet conductivity	λ_{wet} (W/m-K)	1.68	2.33	2.02	LB990861233129.001	1.675*	2.074*	1.890*	LB0210THRMLPRP.001
tortuosity	t	0.2	0.2	0.2	Assumed (Section 5) from range of Accepted Data (de Marsily 1986 [100439])	0.2	0.2	0.2	Assumed (Section 5) from range of Accepted Data (de Marsily 1986 [100439])
FRACTURE DATA[1]									
permeability	k_f (m^2)	8.79E-13	3.68E-13	2.38E-12	LB0011DSTFRAC1.001	7.80E-13	3.30E-13	9.10E-13	LB0205REVUZPRP.001
porosity (Tptpmn Model)	ϕ_f	8.5E-3	1.0E-2	1.5E-2	LB997141233129.001	-	-	-	-
porosity (Tptpll Model)	ϕ_f	6.6E-3	1.0E-2		LB990861233129.001	5.8E-3	8.5E-3	9.6E-3	LB0205REVUZPRP.001
	ϕ_f			1.8E-2	LB0011DSTFRAC1.001				
van Genuchten α	α_f (1/Pa)	1.46E-3	5.16E-4		LB990861233129.001	1.59E-3	1.04E-4	1.02E-4	LB0208UZDSCPMI.002
	α_f (1/Pa)			8.23E-5	LB0011DSTFRAC1.001				

Table 6.4-1 Summary of Hydrological and Thermal Properties of Repository Units (continued)

		REV01				REV02			
Model Layer > Lithostratigraphic Unit >		***tsw33 Tptpul***	***tsw34 Tptpmn***	***tsw35 Tptpll***		***tsw33 Tptpul***	***tsw34 Tptpmn***	***tsw35 Tptpll***	
van Genuchten m (or λ)	m_r	0.608	0.608	0.611	LB990861233129.001	0.633	0.633	0.633	LB0205REVUZPRP.001
residual saturation	S_{irf}	0.01	0.01	0.01	LB990861233129.001	0.01	0.01	0.01	LB0205REVUZPRP.001
satiated saturation	S_{isf}	1.00	1.00	1.00	LB990861233129.001	1.00	1.00	1.00	LB0205REVUZPRP.001
active fracture parameter	gamma	0.41	0.41	0.41	LB990861233129.001	0.60	0.57	0.57	LB0208UZDSCPMI.002
frequency	f (1/m)	0.81	4.32	3.16	LB990861233129.001	0.81	4.32	3.16	LB0205REVUZPRP.001
fracture to matrix area	A (m^2/m^3)	4.44	13.54	9.68	LB990861233129.001	4.44	13.54	9.68	LB0205REVUZPRP.001
tortuosity	t	0.7	0.7	0.7	LB991091233129.006	0.7	0.7	0.7	LB991091233129.006
epsilon (for max P_{cap})	ε	0.01	0.01	0.01	Model Setup (Section 6.4.6.1)	0.01	0.01	0.01	Model Setup (Section 6.4.6.1)

NOTE: [1] Fracture thermal properties are derived using matrix properties as discussed in Section 6.4.6

* Bulk conductivities converted from grain conductivity values and lithophysal porosities listed in DTN shown, using $K_{bulk} = K_{grain}(1-\phi_{lith}) + \phi_{lith} K_{air}$, with K_{air} = 0.028 (W/m-K) (extrapolated at 50°C from Lide 1993 [123032], p. 6-172).

Table 6.4-2 Data Tracking Numbers for Sources of Model Inputs Used in REV01 and Sensitivity Analyses[1]

DTNs	THC Model	Data/Parameter Description
Hydrological and Thermal Rock Properties		
LB990861233129.001 [110226]	Tptpmn REV01 and DST REV01	Permeability (except tsw33, tsw34 and tsw35 fractures), matrix porosity, van Genuchten m, van Genuchten alpha (except tsw35 fractures), residual saturation, satiated saturation, active fracture parameter, fracture frequency, fracture to matrix area; matrix thermal properties: bulk dry and wet conductivity, grain specific heat, and grain density
LB997141233129.001 [104055]		Fracture porosity
LB0011DSTFRAC1.001 [153470]		Fracture parameters: permeability (tsw33, tsw34, and tsw35 only) and van Genuchten alpha (tsw35 only)
LB990861233129.001 [110226]	Tptpll REV01	Permeability (except tsw33, tsw34 and tsw35 fractures), porosity (except tsw35 fractures), van Genuchten m, van Genuchten alpha (except tsw35 fractures), residual saturation, satiated saturation, active fracture parameter, fracture frequency, fracture to matrix area; matrix thermal properties: bulk dry and wet conductivity, grain specific heat, and grain density
LB0011DSTFRAC1.001 [153470]		Fracture parameters: permeability (tsw33, tsw34, and tsw35 only), porosity (tsw35 only), and van Genuchten alpha (tsw35 only)
Mineralogical Data		
LB991200DSTTHC.003 [161276]	DST REV01 and Tptpmn REV01	Mineral volume fractions (Attachment I)
LB0101DSTTHCR1.003 [161278]	DST REV01 and Tptpmn REV01	Mineral surface areas (Attachment III)
Thermodynamic and Kinetic Data		
LB0101DSTTHCR1.006 [161280]	All REV01 models	Thermodynamic data for aqueous species and minerals: equilibrium constants, molecular weights, molar volumes, Debye-Hückel parameters, CO_2 molecular diameter (Attachment V)
MO0302SPATHDYN.000 [161756]	Tptpll REV02 (sensitivity only)	Equilibrium constants, molecular weights, molar volumes
BSC (2002 [158375], Table 4)	All REV01	Rate constants and activation energies (Table 6.4-3)
Repository Drift Design Data		
CRWMS M&O 2000 [151014]	Tptpmn REV01	Invert thickness (0.6 m)
LB0101DSTTHCR1.007 [161281]	All REV01 THC Seepage models	Heat load (Attachment VII)
CRWMS M&O 2000 [120903], Section 4.2	All REV01 THC Seepage models	Heat removal by ventilation (70%)

NOTE: [1] Not used for TSPA-LA

able 6.4-3. REV01 Kinetic Rate Law Data for Mineral-Water Dissolution and Precipitation

Mineral	k_0 (mol m^{-2} s^{-1})	E_a (kJ/mol)	m[1]	n[1]	Comment[2]
α-Cristobalite	3.1623×10^{-13}	69.08	1	1	dissolution
Quartz	1.2589×10^{-14}	87.5	1	1	dissolution only
Tridymite	3.1623×10^{-13}	69.08	1	1	dissolution only
Amor. Silica	7.9433×10^{-13}	62.8	1	1	dissolution
	1.0×10^{-10}	0.0	4.4	1	precipitation
Opal_proxy	7.9433×10^{-13}	62.8	1	1	no precip.
Calcite	1.6×10^{-6}	41.87	1	1	reversible
	equilibrium	NA	NA	NA	local equilibrium
Microcline	1.0×10^{-12}	57.78	1	1	reversible
Albite-Low	1.0×10^{-12}	67.83	1	1	reversible
Anorthite	1.0×10^{-12}	67.83	1	1	dissolution only
Smectite-Ca	1.0×10^{-14}	58.62	1	1	reversible
Smectite-Na	1.0×10^{-14}	58.62	1	1	reversible
Smectite-Mg	1.0×10^{-14}	58.62	1	1	reversible
Smectite-K	1.0×10^{-14}	58.62	1	1	reversible
Illite	1.0×10^{-14}	58.62	1	1	reversible
Kaolinite	1.0×10^{-13}	62.8	1	1	reversible
Sepiolite	1.0×10^{-14}	58.62	1	1	reversible
Stellerite	1.99×10^{-12}	62.8	1	1	reversible
Heulandite	1.99×10^{-12}	62.8	1	1	reversible
Mordenite	1.99×10^{-12}	62.8	1	1	reversible
Clinoptilolite	1.99×10^{-12}	62.8	1	1	reversible
Glass (vphyr)†	7.7233×10^{-15}	91	1	1	dissolution only
Gypsum	equilibrium	NA	NA	NA	local equilibrium
Hematite	7.9433×10^{-13}	62.8	1	1	dissolution only
Goethite	equilibrium	NA	NA	NA	NA
Fluorite	1.2224×10^{-7}	0	1	2	reversible

Source: Taken from Table 4 in MDL-NBS-HS-000001 REV01, ICN02 (BSC 2002 [158375]) (not used for TSPA-LA).

NOTES: k_o Rate Constant

E_a Activation Energy

NA Not Applicable

† "Vphyre" refers to the basal vitrophyre of the Topopah Spring welded hydrogeologic unit (TSw) unit. The composition of this glass was used for all glass-bearing units, including the nonwelded Paintbrush nonwelded hydrogeologic unit (PTn) glassy tuffs.

(1) Exponents *m* and *n* in Equation 6.4-8.

(2) "dissolution only" means precipitation of this mineral is not allowed. "reversible" indicates the same precipitation and dissolution rate apply.

6.5 Tptpmn THC MODEL REV01

The Tptpmn THC Model REV01 is an earlier variation of the THC Seepage Model completed as part of the previous version (REV01) of this Model Report. The conceptualizations and mathematical formulations developed for this model are presented in Sections 6.1 to 6.4. The Tptpmn THC Model is a two-dimensional numerical model along a laterally continuous, vertical geologic section with stratigraphy similar to that in borehole USW SD-9 (at Nevada State Plane coordinates E171234, N234074; DTN: LB990501233129.004 [111475]). The modeled drift is located in the Topopah Spring Tuff middle nonlithophysal geologic unit (Tptpmn unit, corresponding to model layer name tsw34, DTN: LB990501233129.004 [111475]). Only part of the repository is planned to be located in the Tptpmn, and therefore the model is not representative of the entire repository. However, most hydrogeologic data available for the repository horizon are from the Tptpmn unit, including data from the Single Heater Test, DST, and many other data collected in the ESF. Alternative models presented in Sections 6.7 and 6.8 consider a drift in the Topopah Spring Tuff lower lithophysal lithostratigraphic unit, or Tptpll, where most of the repository is planned to be located.

The key elements of the Tptpmn THC Model REV01 include:

- Initial heat load of (1.45 kW/m) (Attachment VII)
- 50-year preclosure period with 70% ventilation efficiency
- Drift in the Tptpmn unit
- Model stratigraphy from geology at borehole SD-9
- Consideration of a base-case and extended-case geochemical system (Section 6.2.2.2)
- Drift wall closed to fluid and gas advection (but open to diffusive fluxes)
- Omission of vapor-pressure lowering by capillary pressure
- Older set of rock thermal and hydrological properties (Table 6.4-1)
- Slightly older thermodynamic database (Attachment V), although not much different than newer data
- Utilization of an older TOUGHREACT version (V2.3 (LBNL 2001 [153101])), a version which does not consider precipitation of solids in dry gridblocks, but into which water influx occurs (Section 6.4.5), and thus underestimates mineral precipitation
- Most useful for comparison with the Tptpll THC Model REV01 results to evaluate effects of drift location (Tptpmn versus Tptpll, see Section 6.7) and model stratigraphy

6.5.1 Numerical Mesh

Simulations were performed on a vertical 2-D mesh, using a drift spacing of 81 m (center to center, 800-IED-EBS0-00402-000-00B (BSC 2003 [161727])) and a drift diameter of 5.5 m (800-IED-EBS0-00301-000-00A, BSC 2003 [162444]). With rock properties laterally homogeneous between drifts (Section 6.4.6.1), this setup can be viewed as a series of symmetrical, identical half-drift models with vertical no-flow boundaries between them. Accordingly, the numerical mesh was reduced to a half-drift model with a width of 40.5 m, corresponding to the midpoint between drifts (Figure 6.5-1). Geologic data from borehole USW SD-9, as implemented in UZ model grid UZ99_2_3D.mesh (DTN: LB990501233129.004 [111475]), were used as a basis to map geologic contacts into the 2-D mesh. The mesh coordinate system was set with reference to the center of the drift (Table 6.5-1). The gridblock size was kept sufficiently fine to provide enough resolution at key model locations (such as at the vicinity of drift and geologic contacts), but as coarse as possible to provide the computing efficiency needed for reasonable simulation times. The area extending approximately 50 m above the drift is more finely gridded than other areas to capture THC effects potentially affecting seepage into the drift. Outside the drift, the smallest grid spacing was specified at the drift wall (20 cm) and increased outward. Because of its minor relevance to this modeling effort, the geology below the tsw38 model layer was simplified compared to the original USW SD-9 data, thus allowing for coarser gridding in this area. The mesh has a total of 2,510 gridblocks, including those representing matrix, fracture, and in-drift design elements.

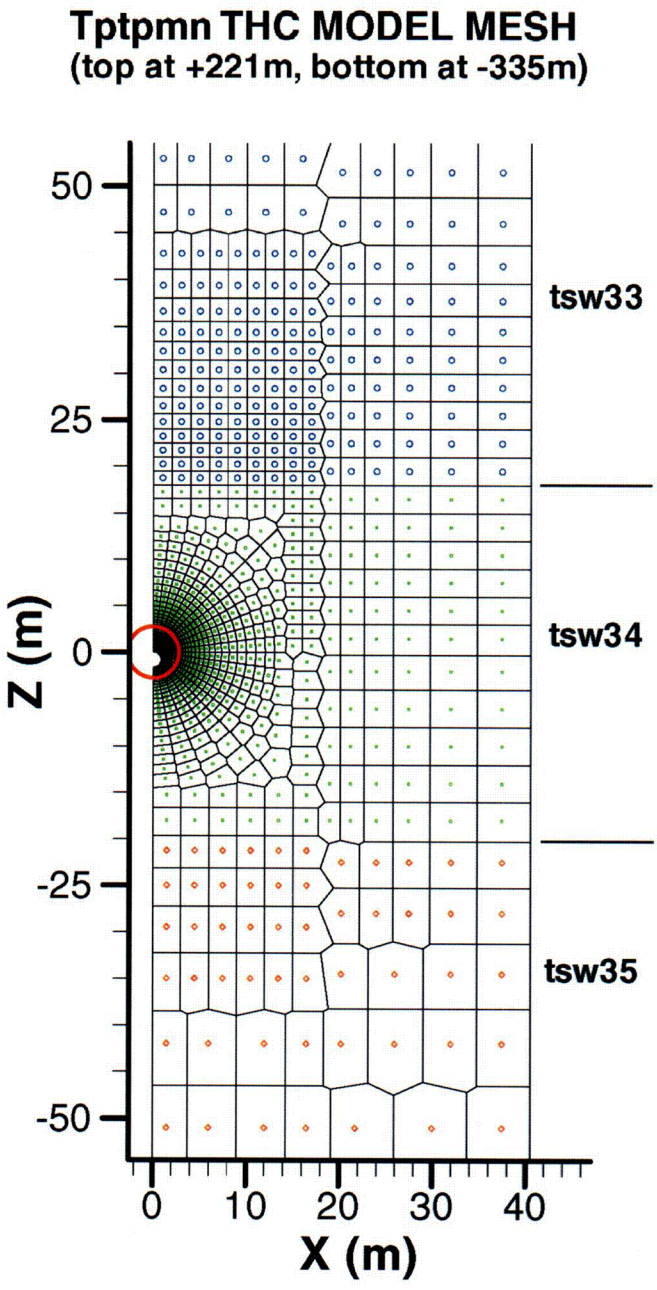

DTN: LB991200DSTTHC.002 [142162]

NOTE: Grid detail around (0, 0) is shown in Figure 6.5-2.

Figure 6.5-1. Tptpmn THC Model Mesh with Hydrogeologic Units Shown in the Vicinity of the Drift: Topopah Spring Tuff Upper Lithophysal (tsw33-circles), Middle Nonlithophysal (tsw34-dots), and Lower Lithophysal (tsw35-diamonds) Units

Table 6.5-1. Vertical Mesh Dimensions and Geologic Contacts in the Tptpmn THC Model

Model Layer	USW SD-9 Top of Layer Elevation (m)	Mesh Top of Layer Z Coordinate (m)
Top	1286.0	220.7
tcw13	1285.4	220.1
ptn21	1279.6	214.2
ptn22	1275.0	209.7
ptn23	1269.1	203.7
ptn24	1264.5	199.2
ptn25	1255.5	190.1
ptn26	1233.8	168.4
tsw31	1221.0	155.7
tsw32	1219.0	153.7
tsw33	1165.7	100.4
tsw34	1080.4	18.0*
Drift center	1065.3	0.0
tsw35	1045.1	-20.2
tsw36	942.6	-122.7
tsw37	906.9	-158.4
tsw38	889.1	-176.3
ch2z	868.4	-197.0
Bottom	730.0	-335.3

DTN: LB990501233129.004 [111475]

NOTE: * Contact raised, compared to USW SD-9 data, to provide for better lateral continuity between the fine mesh above the drift and coarser mesh laterally away from the drift (See Figure 6.5-1).

The drift was discretized to include the design elements and dimensions shown on Figure 4.1-1 (338 gridblocks total) (Figure 6.5-2). The drip shield is not explicitly modeled (Section 4.1.7). The gridblock size inside the drift was chosen small enough to provide a realistic drift model (compare Figure 6.5-2 to Figure 4.1-1). Two in-drift configurations are considered in this model:

- Preclosure configuration (during the first 50 years): waste package, upper invert, lower invert, and the open space between the waste package and the drift wall
- Postclosure configuration (after 50 years): waste package, upper invert, lower invert, drip shield, and two open zones: the inner zone, between the waste package and the drip shield; and the outer zone, between the drip shield and drift wall.

The discretization of the drift was kept the same for the two configurations. As such, the preclosure period was simulated by assigning identical open-space properties to gridblocks representing the inner zone and outer zone.

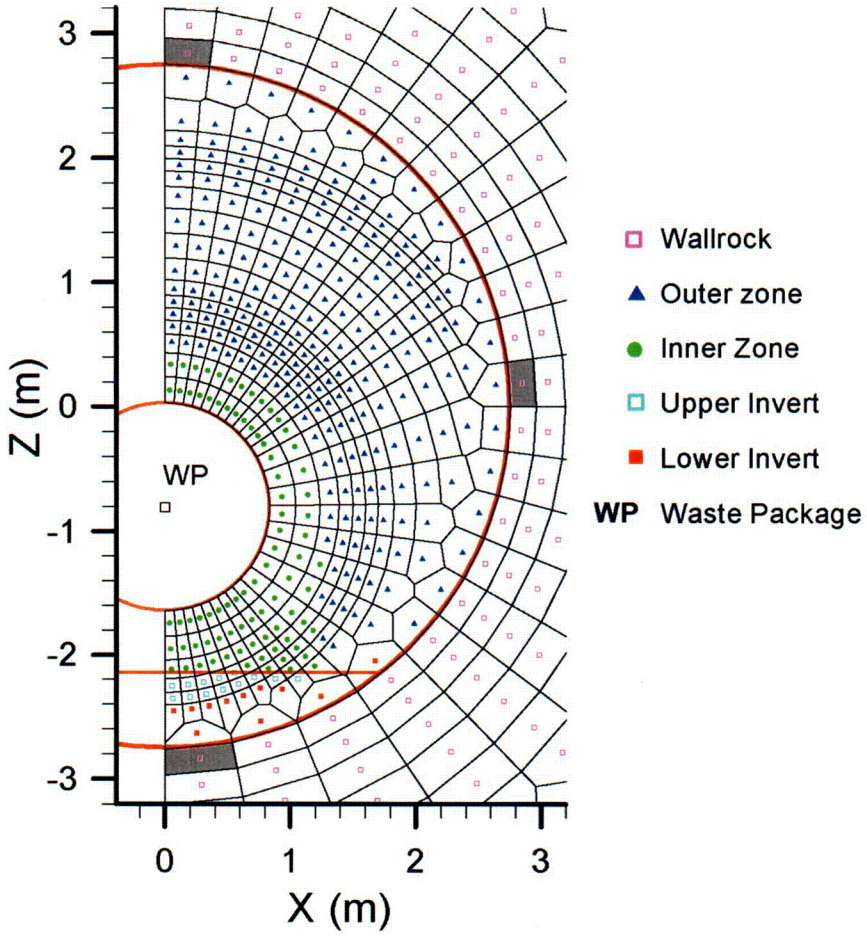

DTN: LB0011DSTTHCR1.001 [154759]

NOTE: Shaded gridblocks are those with top, side, base designations in other figures.

Figure 6.5-2. Discretization of the Repository Drift—Tptpmn THC Model

6.5.2 Boundary Conditions

The following boundary conditions were imposed on the Tptpmn THC Model (Table 6.5-2):

- Top boundary: stepwise changing infiltration rate (Table 6.5-3), temperature, pressure, and gas saturation (representing open atmosphere); constant CO_2 partial pressure and composition of infiltrating water
- Bottom boundary: constant temperature, pressure, and liquid saturation (representing the water table). Constant water composition and CO_2 partial pressure at equilibrium
- Side boundaries: no heat, fluid, and chemical fluxes
- Waste package: variable heat load with time, including effect of 70% heat removal by ventilation for first 50 years (preclosure).

One mean infiltration regime was modeled, simulating future climatic conditions including present day, monsoon, and glacial-transition periods (Table 6.5-3).

Table 6.5-2. Tptpmn THC Model REV01 Boundary Conditions

Boundary	Boundary Condition	Reference
Top	T = 17.68°C	Table 4.1-1
	S_g = 0.99	Table 4.1-1
	P = 86339 Pa	Table 4.1-1
	Time-varying infiltration rate (mean infiltration regime only)	Table 6.5-3
	Constant composition of infiltration and PCO_2	Table 6.2-1
Bottom	T = 31.68°C	Table 4.1-1
	S_L = 0.99999	Table 4.1-1
	P = 92000 Pa	Table 4.1-1
	Constant water composition and PCO_2	Table 6.2-1
Sides	No flux for water, gas, heat, and chemical species	Not Applicable
Drift Wall	No flux for water, gas and chemical species (except for CO_2 diffusive flux); conduction only for heat (zero permeability in drift gridblocks)	Not Applicable
Waste Package	Initial full heat load of 1.45 kW/m decreasing with time (due to radioactive decay), and reduced by 70% during the first 50 years (due to heat removal by ventilation)	Attachment VII and Table 6.4-2

NOTES: T = Temperature
S_g = Gas saturation
S_L = Liquid saturation
P = Pressure

Table 6.5-3. Tptpmn THC Model Infiltration Rates and Corresponding Rock-Property Sets

Case	Infiltration Rate (mm/yr)	Time Period (years)	Calibrated Properties Set	Reference
Mean Infiltration	6	0 to 600 (present day)	Present Day Mean	Table 4.1-1
	16	600 to 2000 (monsoon)		
	25	2000 to 100,000 (glacial transition)		

6.5.3 Input Data and Modeling Procedure

Simulations for the Tptpmn THC Model were run using TOUGHREACT V2.3 (LBNL 2001 [153101]), the thermodynamic data shown in Attachment V, and kinetic data in Table 6.4-3. Input water and gas compositions are shown in Table 6.2-1. Initial mineralogy and mineral surface areas are given in Attachments I and III, respectively. This model was run using the base-case and extended-case sets of chemical components and mineral assemblages described in Section 6.2.2.2. Rock hydraulic properties calibrated for a mean infiltration case were used (Table 6.4-1).

To provide initial thermal and hydrological conditions, a simulation was performed without reactive transport, heat load, or a drift (i.e., with rock at the location of the drift) until steady-state thermal and hydrological conditions were achieved. A steady state was considered to have been met under at least one of the following conditions:

1. Liquid saturations, temperatures, and pressures remained constant within the model over a time span of at least 100,000 years.

2. The total liquid and gas inflow at the top of the model matched the total liquid and gas outflow at the base of the model within 0.01 percent.

THC simulations were then run with the drift in place and heat transfer from the waste package, using the steady-state temperatures, pressures, and liquid saturations as initial conditions. Open spaces within the drift were set to zero liquid saturation and permeability.

"Ambient" reactive-transport simulations with the drift in place but without heating (i.e., no heat release from the waste package) were also performed for comparison of chemical trends to simulations under thermal loading. These simulations of ambient conditions were run using the same mean infiltration regime as the simulations of thermal loading (Table 6.5-3).

As discussed in Section 4.1.7, THC simulations were run for an initial period of 50 years, using the preclosure drift configuration and thermal properties. The simulations were then restarted using the postclosure drift configuration and properties from 50 years to a total simulation time of 100,000 years. At times corresponding to changes in infiltration rates (at 600 and 2,000 years, Table 6.5-3), the simulations were stopped and then restarted with the new infiltration rate (thus resulting in a stepwise change in infiltration).

Maximum time steps of 1, 2, 5, and 10 years were used for the time periods spanning 50–600, 600–2,000, 2,000–20,000, and 20,000-100,000 years, respectively. The runs were restarted for each of these time periods to accommodate for the change in maximum time step and/or infiltration rate.

In this model, calcite was set to remain locally at equilibrium because calcite reaction rates reported in the literature (Table 6.4-3) are quite rapid. Very similar results in simulations of the DST are obtained when using local equilibrium for calcite and assuming a kinetically controlled reaction rate (Section 7.1). Using equilibrium has the advantage of allowing simulations with larger time steps than would be required with a kinetically controlled fast calcite reaction rate.

Using pH and calcium concentrations measured in pore-water samples (Table 6.2-1), together with independently measured CO_2 partial pressures in ambient pore-gas samples (see data sources in Table 7-1), calcite is calculated to supersaturate in pore waters by approximately 1 $\log(Q/K)$ unit at 25°C. The reason for this supersaturation has not been determined and could be the result of various factors, including (but not limited to) analytical errors, kinetic inhibition caused by organic or other compounds in solution, or effects caused by high capillary pressure or pressures developed during the ultra-centrifuge water-extraction process. To reconcile measured pH, calcium, and CO_2 concentrations, calcite was allowed to remain supersaturated by approximately 1 $\log(Q/K)$ unit at 25°C. This "precipitation gap" was set to decrease exponentially with temperature and become negligible (one hundredth of the gap value at 25°C) at an arbitrarily selected temperature of 200°C. This approach (using a precipitation gap) can be viewed as a crude approximation of precipitation with a nucleation threshold. Note that dissolution still occurs only if $\log(Q/K) < 0$.

A fairly stable (near steady-state) hydrochemical system was achieved using revised thermodynamic data (Attachment V) primarily for smectites and zeolites. More recent simulations of ambient conditions (no thermal pulse) using various sources of thermodynamic data are presented in Section 6.8 and provide an additional justification for using the thermodynamic data selected here. The stability of water and gas concentrations calculated for ambient conditions over long periods of time was also improved by implementing the calcite supersaturation gap as described above.

6.5.4 Model Runs

A total of five simulations were completed, as summarized in Table 6.5-4.

Table 6.5-4. Tptpmn THC Model Runs (REV01)

Infiltration-Property Set (Table 6.5-3)	Geochemical System (Section 6.2.2.2)	Simulation Type	Run ID (used in DTN: LB0011DSTTHCR1.002 [161282]; also see Attachment X)
Mean Infiltration	None	TH	th6_16_25_7
Mean Infiltration	Base Case	THC	thc6_16_25_9
	Base Case	THC - Ambient	thc6_16_25_9_amb
	Extended Case	THC	thc6_16_25_10
	Extended Case	THC - Ambient	thc6_16_25_10_amb

NOTES: TH: Thermal-hydrological
THC: Thermal-hydrological-chemical

6.5.5 Simulation Results

Simulation results are presented below in Figures 6.5-3 through 6.5-18, and focus on areas in the vicinity of the drift. THC effects in other geologic horizons, even though considered in the simulations, are not discussed in this Model Report because they are not directly relevant to the primary purpose of evaluating THC effects at the drift scale. Much of the data (temperatures, liquid saturations, water compositions, CO_2 concentrations, and liquid/gas fluxes) are examined as a function of time at three locations around the modeled drift. These are the crown, the side (approximately 20 cm above the springline) and the base (model gridblocks F257, F 92, and F272, respectively) at points located 10 cm to the outside of the drift wall (i.e., in the rock) (Figure 6.5-2). These data were tabulated and submitted to the technical database under DTN: LB0011DSTTHCR1.001 [154759] and are discussed below.

6.5.5.1 Thermal-Hydrological Simulation Results

For comparison to the THC simulations, a model run was performed considering only thermal and hydrological (TH) processes. This simulation was run using the mean infiltration case (Table 6.5-3) and serves as a baseline for interpreting the effects of water-gas-rock chemical interaction on the thermal and hydrological behavior of the system.

Calculated temperatures, liquid saturation, and air mass fractions around the drift are shown in Figures 6.5-3 through 6.5-6. Postclosure temperatures quickly climb above the boiling point (near 96°C at Yucca Mountain), with temperatures at the drift crown peaking to around 135°C between the times of 55 and 75 years. The highest modeled temperature in the waste package is attained during this time interval as well (the highest output value is near 155°C). Temperatures are lower at the base of the drift (approximately 10°C or less than at the crown) because of the insulating effect of the invert (Figure 6.5-3). The return to ambient temperatures after heating takes 50,000 to 100,000 years.

Around the drift, the matrix is predicted to rewet at times between 1,200 and 1,400 years (Figure 6.5-3). Rewetting of fractures occurs within the same time frame, except at the drift base where fractures do not rewet until approximately 2,000 years (Figure 6.5-3). A contour plot of temperatures and matrix saturations in the vicinity of the drift at a simulated time of 600 years

(near maximum dryout) shows the dryout zone (represented by zero matrix saturations) extending approximately 8 m above the drift, 10 m to the side of it, and 13 m below it (Figure 6.5-4). In fractures, liquid saturations (Figure 6.5-5) show strong diversion of water around the dryout zone. Air mass fractions in the gas phase at the drift wall (the complement of the steam mass fraction; Figure 6.5-6) drop to near-zero values during dryout (i.e., the gas phase is almost entirely water vapor) and is essentially identical in both matrix and fractures.

The calculated rate of vertical water influx in fractures at the drift crown (Figure 6.5-7) shows a small short-lived influx peak at the time of rewetting. However, the intensity of this peak may only reflect the time intervals at which data are output from the model. The general flux increase after 2,000 years reflects the increase in infiltration rate at that time (from 16 to 25 mm/y). For the ambient simulation, the flux increase at 600 years also reflects the infiltration rate increase at that time (from 6 to 16 mm/yr).

Note that TH results presented in this section do not exactly match results presented in BSC (2003 [161530], Section 6.2.2) for a similar TH model. This is because simulations presented in this section were run with an older set (REV01) of rock properties (see Table 6.4-1) than in BSC (2003 [161530], Section 6.2.2.

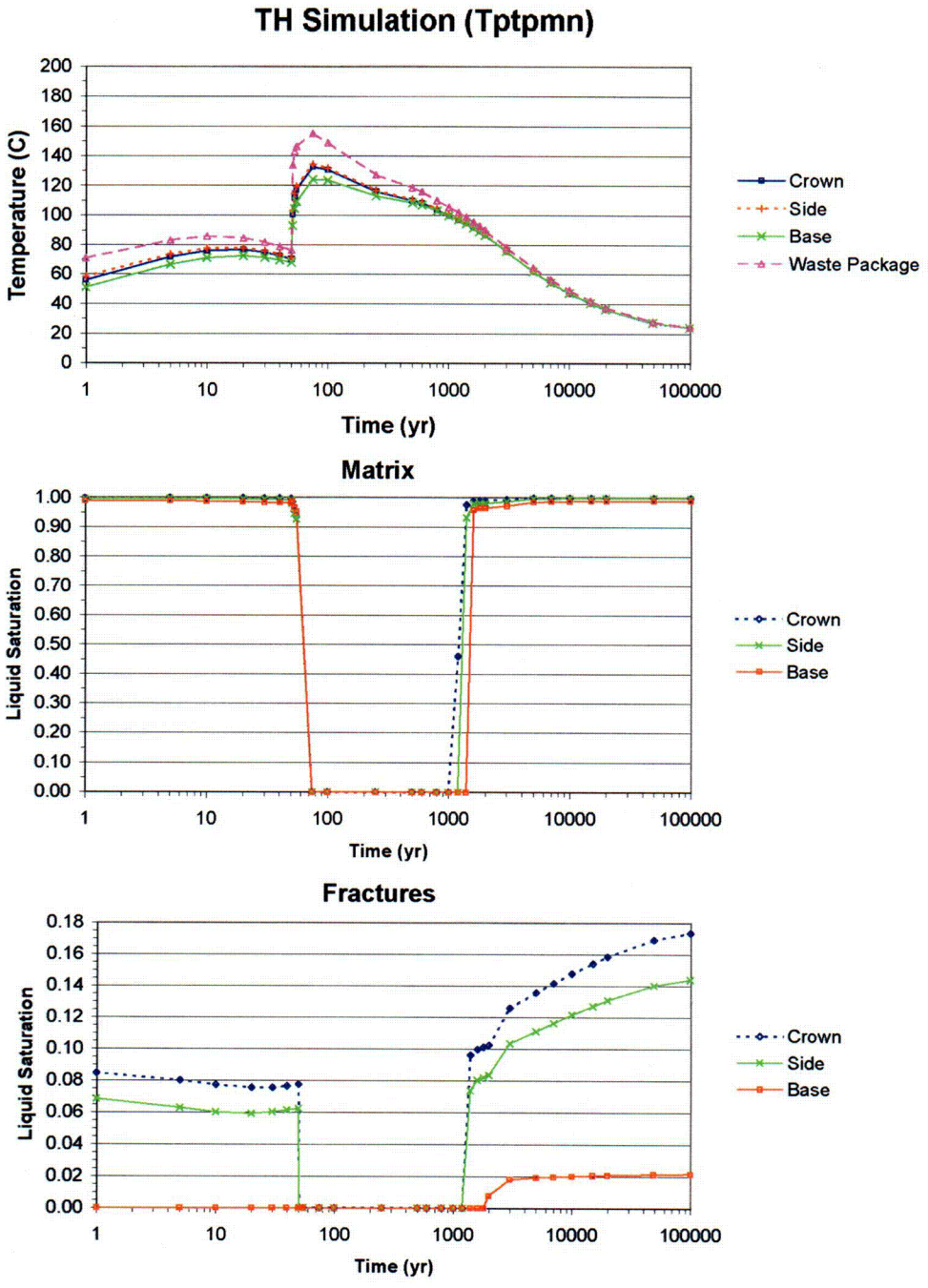

DTN: LB0011DSTTHCR1.001 [154759]

Figure 6.5-3. TH Simulation (Tptpmn Model): Time Profiles of Modeled Temperatures and Liquid Saturations in Fractures and Matrix at Three Drift-Wall Locations and in the Waste Package

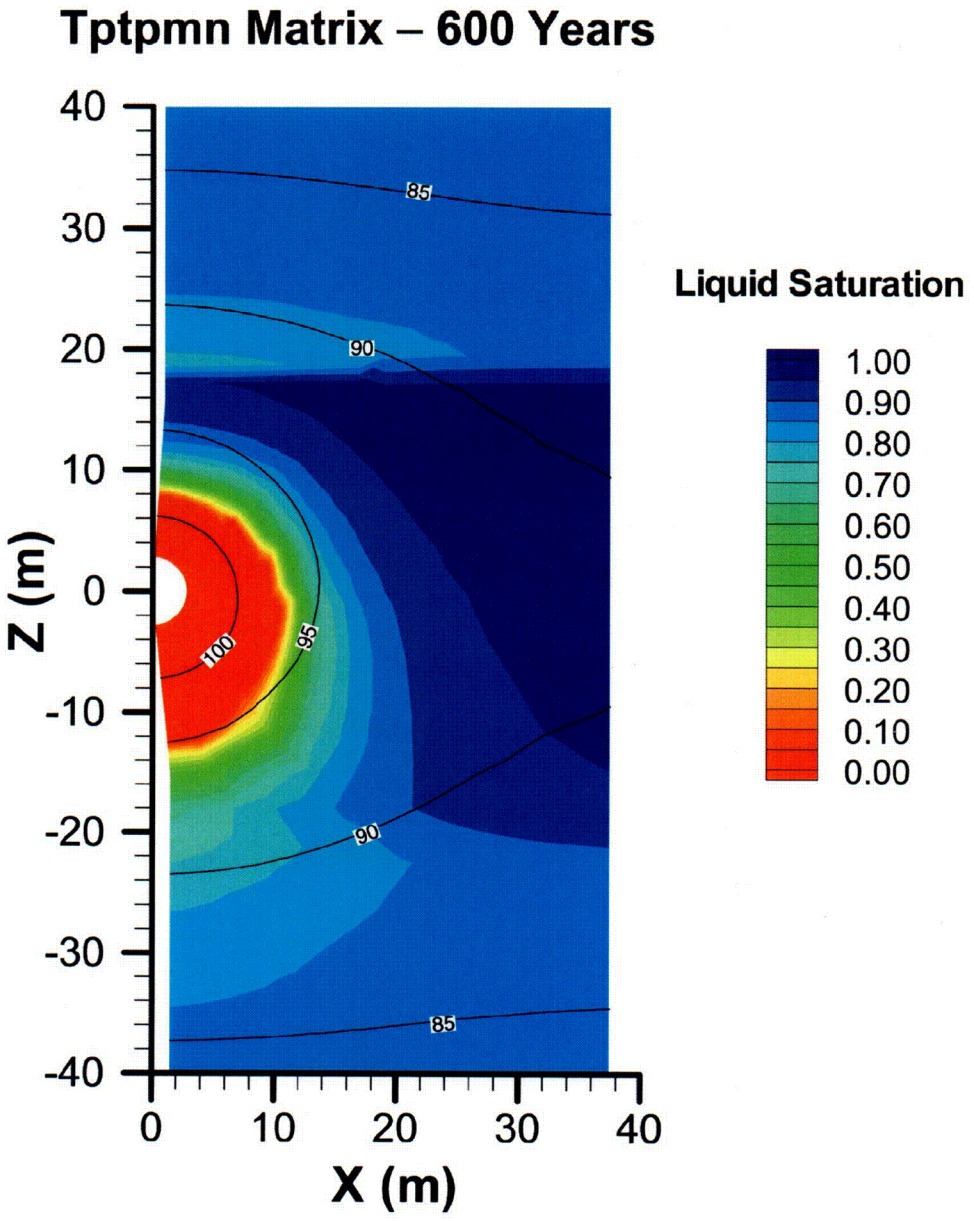

DTN: LB0011DSTTHCR1.002 [161282]

Figure 6.5-4. TH Simulation (Tptpmn Model): Contour Plot of Modeled Temperatures (°C) and Liquid Saturations in the Matrix at 600 Years (Near Maximum Dryout—Mean Infiltration)

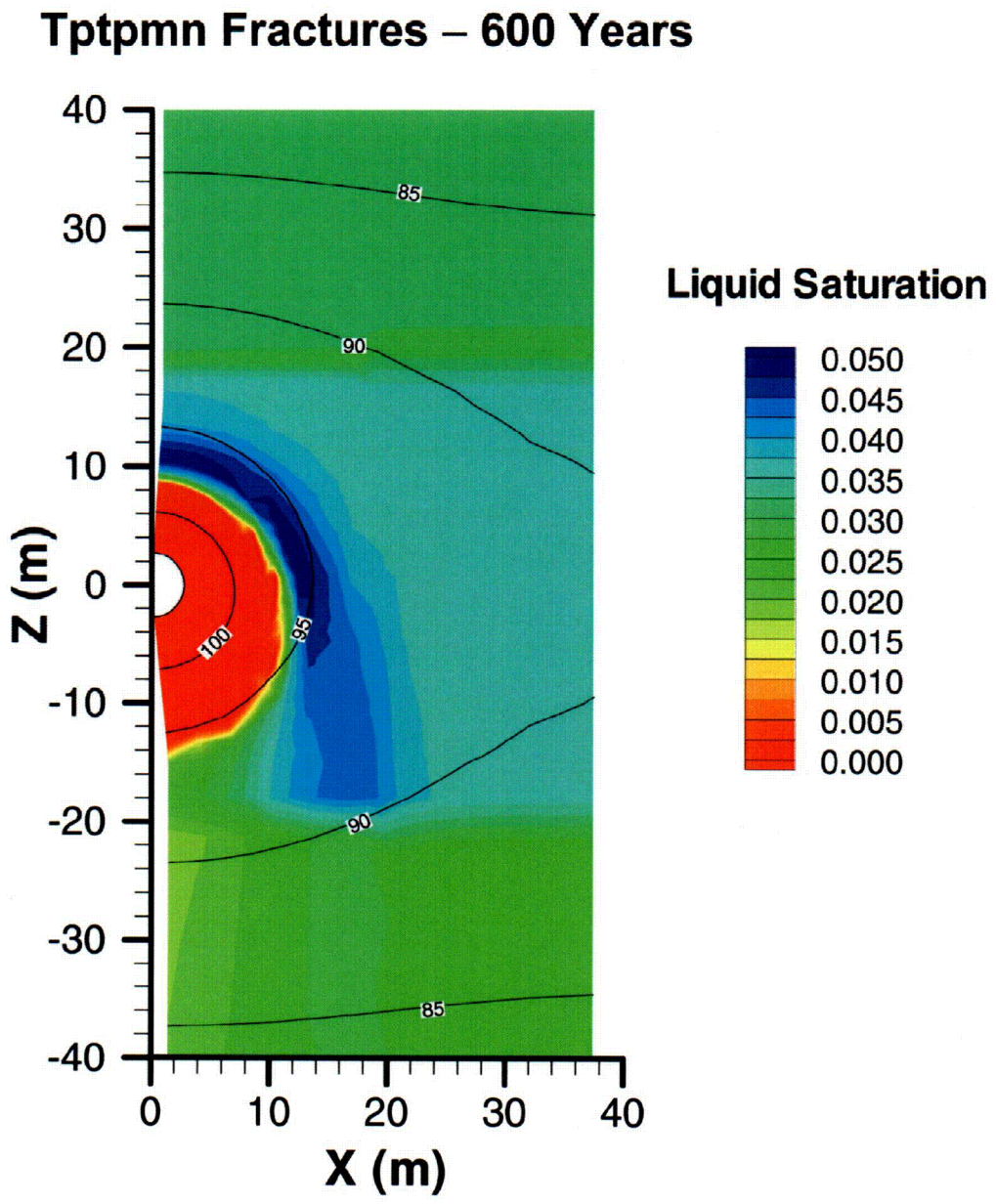

DTN: LB0011DSTTHCR1.002 [161282]

Figure 6.5-5. TH Simulation (Tptpmn Model): Contour Plot of Modeled Temperatures (°C) and Liquid Saturations in Fractures at 600 Years (near Maximum Dryout—Mean Infiltration)

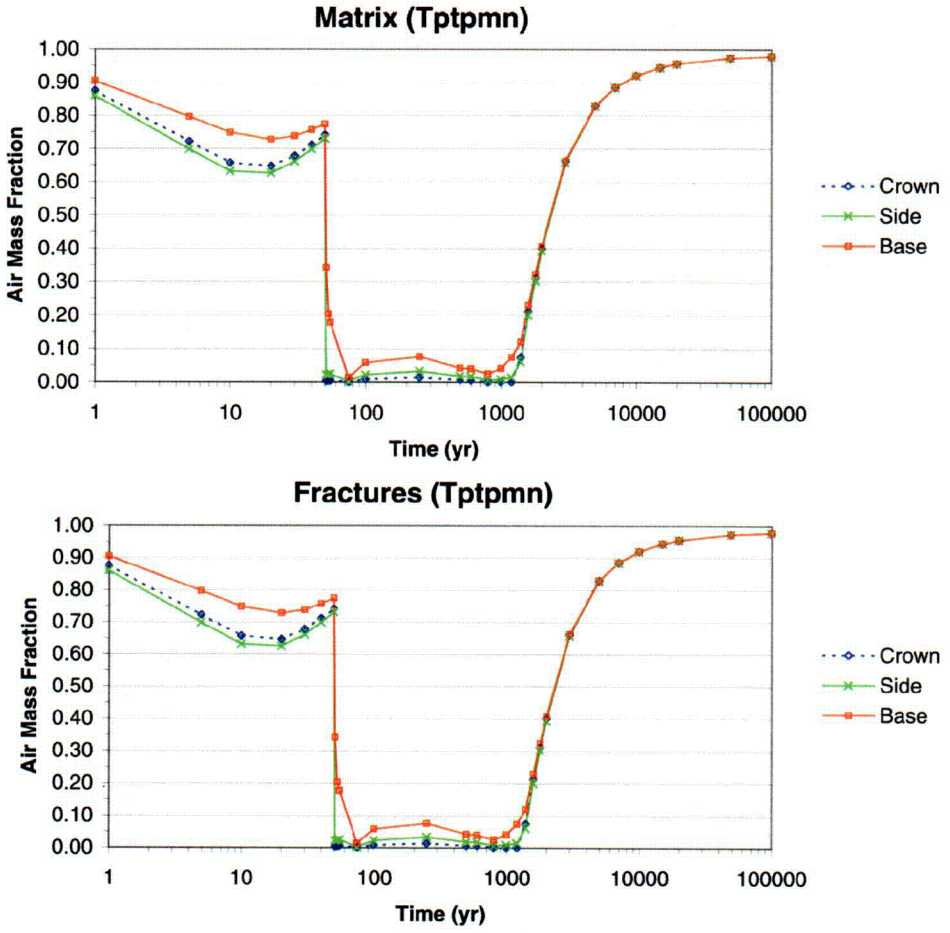

DTN: LB0011DSTTHCR1.001 [154759]

Figure 6.5-6. TH Simulation (Tptpmn Model): Time Profiles of Modeled Air Mass Fractions in the Gas Phase in Fractures and Matrix at Three Drift-Wall Locations

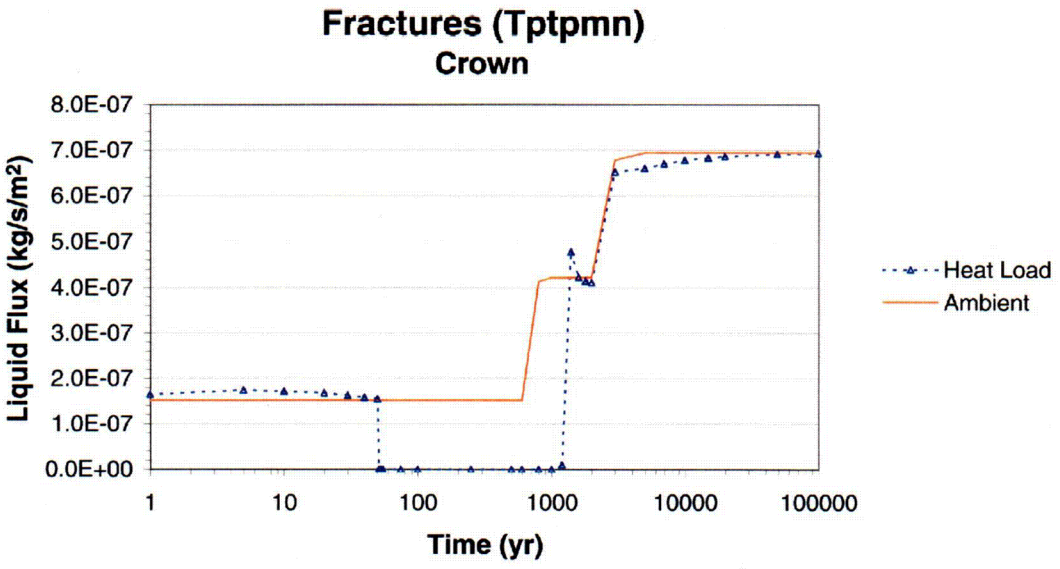

DTN: LB0011DSTTHCR1.001 [154759]

Figure 6.5-7. TH Simulation (Tptpmn Model: Time Profiles of Modeled Water Flux at the Drift Crown (positive downward)

6.5.5.2 THC Simulation Results

Time profiles of predicted CO_2 and various aqueous species concentrations in fractures are shown in Figures 6.5-8 to 6.5-15. These figures combine the results of ambient and heat-load calculations for both base-case (no aluminum silicates) and extended-case geochemical systems (Section 6.2.2.2).

The results of simulations under ambient conditions are presented to provide a baseline by which comparisons can be made with simulations of thermal loading. Obtaining an initial "steady-state" hydrochemical system yielding aqueous species concentrations consistent with measured concentrations in pore water is difficult. This is because the stability of the system depends on reaction rates and relative mineral thermodynamic stability, as well as infiltration rates and rock properties. The difficulty in reaching a chemical steady state increases with the number of reactive minerals included in the system, because each additional mineral adds its own uncertainty in reaction rate to the total model uncertainty. A reasonably "steady" ambient hydrochemical state was achieved here by reducing the stability of smectites and zeolites (Attachment V), and allowing some degree of calcite supersaturation (Section 6.5.3) in pore waters. In earlier simulations with unrevised thermodynamic data (DTN: LB991200DSTTHC.002 [142162]), smectites and zeolites were too stable and formed in unreasonable amounts. This yielded an unrealistic predicted pH increase, calcium depletion, and an increase in sodium in the pore waters under ambient conditions. Similar unrealistic trends predicted with new simulations using unrevised thermodynamic data for clays and zeolites are discussed in Section 6.8.5.1. These trends are governed by feldspar and glass hydrolysis reactions such as those discussed below.

The use of alternative geochemical systems is useful in assessing the sensitivity of the model to inclusion of aluminum silicate minerals. Extended-case simulations are quite sensitive to the

effective reaction rates of aluminum silicates, particularly clays and calcium zeolites. For example, the dissolution of albite (a sodium feldspar) to form sodium smectite (a clay) results in an increase in pH (decrease in H^+ activity), as follows:

$$2.33NaAlSi_3O_8 \text{ (albite)} + 2H^+ \Longrightarrow$$

$$Na_{0.33}Al_{2.33}Si_{3.67}O_{10}(OH)_2 \text{ (smectite)} + 3.32SiO_2 + 2Na^+ \qquad \text{(Eq. 6.5-1)}$$

The alteration of albite to stellerite (a calcium zeolite) can also drive pH to higher values if the calcium necessary to form stellerite originates from calcite dissolution, as in the following reaction:

$$2NaAlSi_3O_8 \text{ (albite)} + SiO_2 + CaCO_3 \text{ (calcite)} + H^+ + 7H_2O \Longrightarrow$$

$$CaAl_2Si_7O_{18} \cdot 7H_2O \text{ (stellerite)} + 2Na^+ + HCO_3^- \qquad \text{(Eq. 6.5-2)}$$

In addition, the consumption of calcium to form calcium zeolites or clays inhibits calcite precipitation as a means of controlling the increase of pH and total aqueous carbonate concentrations. As a result of such reactions, simulations with the extended geochemical system generally yield higher pH and total aqueous carbonate concentrations, and generally lower CO_2 partial pressures than with the base-case system. Also, because of these reactions, predicted calcium concentrations under ambient conditions tend to decrease with time, while the sodium concentrations increase—trends that are not observed with base-case simulations.

The predicted trend of CO_2 concentrations with time in fracture gas (Figure 6.5-8) generally shows a large decline during dryout, followed by a steep increase during the initial cooling and rewetting stage. The decrease during dryout is the direct result of displacement by steam upon boiling. The increase after dryout remains below 10,000 ppmv for both the base case and the extended case, and concentrations are predicted to return to ambient values after 20,000 to 50,000 years.

The predicted pH of fracture water around the drift (Figures 6.5-9) is higher in the extended case (approximate range 7.7 to 8.4) than in the base case (approximate range 7.4 to 7.8). Total aqueous carbonate concentrations (as HCO_3^-) (Figure 6.5-10) are similar in the base and extended cases, showing a typical decrease at the drift wall during the thermal pulse due to temperature-driven decarbonation. During preclosure, pH and carbonate concentrations drop quickly to values near pH 7.8 and 80 mg/L, respectively, as a result of calcite precipitation accompanying increasing temperature.

Calcium concentrations (Figure 6.5-11) are predicted to be generally lower in the extended case than the base case, resulting from increased calcite precipitation (caused by higher pH) and precipitation of calcium zeolites and clays as in reactions discussed earlier. Predicted ambient sodium concentrations (Figure 6.5-12) approximately double over the 100,000-year simulated time period, which could reflect somewhat higher feldspar and/or glass dissolution rates relative to the precipitation rate of clay minerals. Relatively elevated calcium and sodium concentrations during rewetting at the drift wall at the base of the drift are the result of remobilization of water containing dissolved salts previously concentrated by evaporation at the time of dryout. Note that in these REV01 simulations, the formation of residual salts upon complete dryout and their

redissolution upon rewetting is not modeled. The water, however, is concentrated up to a limit ionic strength of 4 upon drying, then is saved for reintroduction into the system at the time of rewetting—see Section 6.4.6.1.

Upon heating, aqueous silica concentrations (Figure 6.5-13) rise significantly above ambient values because of the dissolution of silica phases at higher temperatures. Simulations with the extended geochemical system yield higher aqueous silica concentrations because of the dissolution of aluminosilicate minerals. These minerals are not included in base-case simulations (mostly cristobalite dissolves in the base-case simulations). Upon boiling to dryness, aqueous silica concentrations may significantly exceed the solubility of amorphous silica (near 370 mg/L at 100°C) because the precipitation rate of this mineral, even though quite fast, does not keep up with boiling rates. During the initial cooling stage, primarily the 600- to 2,000-year time interval, aqueous silica around the drift precipitates as amorphous silica and, as will be discussed later, accounts for most of the reduction in porosity around the drift during this time. With the base-case geochemical system, ambient aqueous silica concentrations remain fairly constant and well below the solubility of amorphous silica (approximately 120 mg/L at 25°C), increasing slightly with increasing infiltration rates, thus reflecting a kinetic control on the dissolution of silica phases. With the extended case, modeled ambient aqueous silica concentrations increase to values at or near amorphous silica solubility (higher than measured pore water concentrations), which seems to indicate that the dissolution rate of feldspar and or glass may be somewhat overestimated relative to the precipitation rate of clays.

Chloride concentrations in fracture water computed for both the base case and the extended case (Figure 6.5-14) are essentially identical because of the conservative behavior of this aqueous species (i.e., it is not affected by pH or the reaction rates of other minerals in the simulation). The profiles also show, at the time of rewetting, the effect of remobilization of concentrated solutions that was mentioned earlier. After rewetting, chloride concentrations drop relatively quickly towards ambient values near 110 mg/L.

Upon rewetting, fluoride concentrations in fracture water (Figure 6.5-15) quickly drop towards ambient values of less than 1 mg/L. In this chemical system, at intermediate to high pH, fluoride concentrations are not affected significantly by pH. Therefore, there are not many differences between base-case and extended-case simulations. It should be remembered that no fluorite (CaF_2 mineral) is present as a primary mineral here. In the Tptpll simulations presented in Sections 6.7 and 6.8, fluorite is included as a mineral in the repository host rock, causing higher fluoride concentrations to be predicted during the cooling phase.

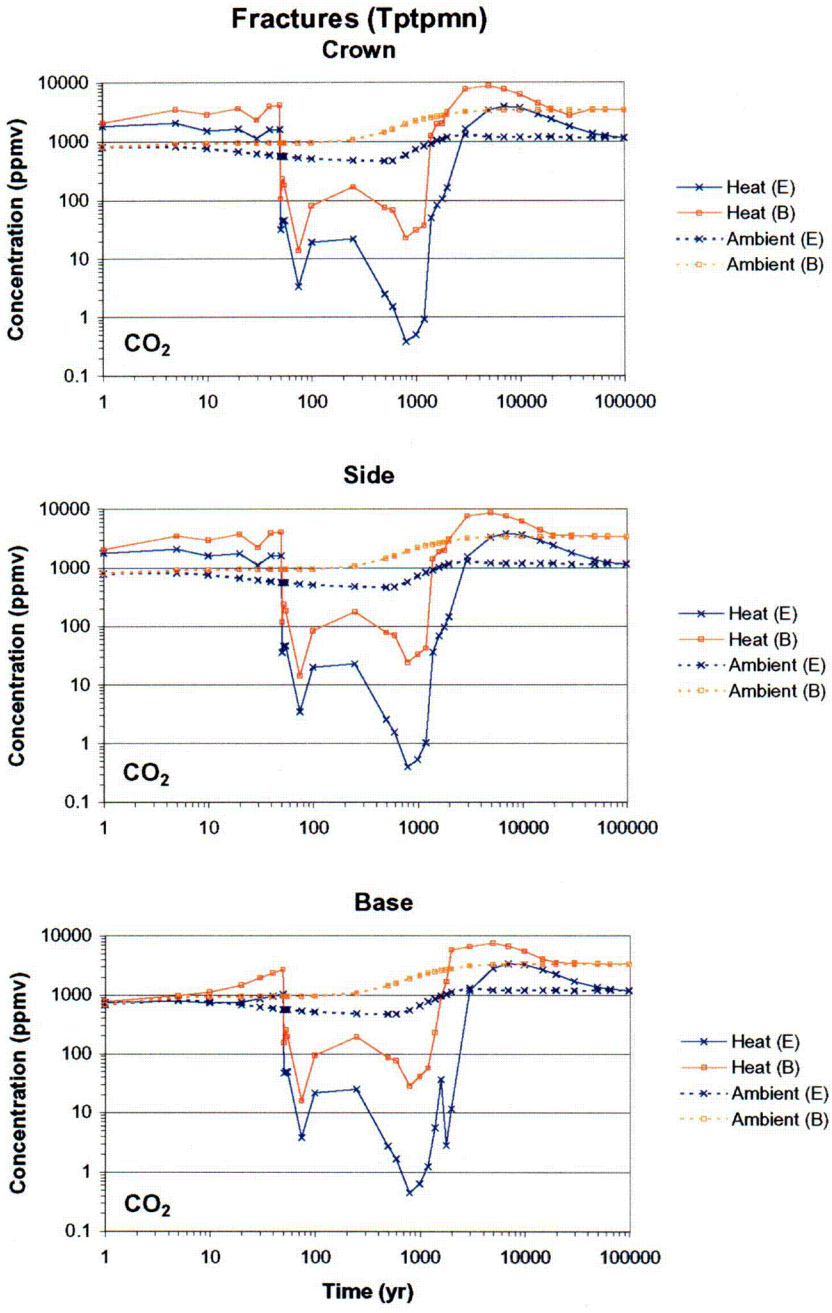

DTN: LB0011DSTTHCR1.001 [154759]

Figure 6.5-8. THC Simulation (Tptpmn Model): Time Profiles of Modeled CO_2 Concentrations in the Gas Phase in Fractures at Three Drift-Wall Locations under Heating (Heat) and Non-Heating (Ambient) Conditions for the Extended (E) and Base-Case (B) Geochemical Systems

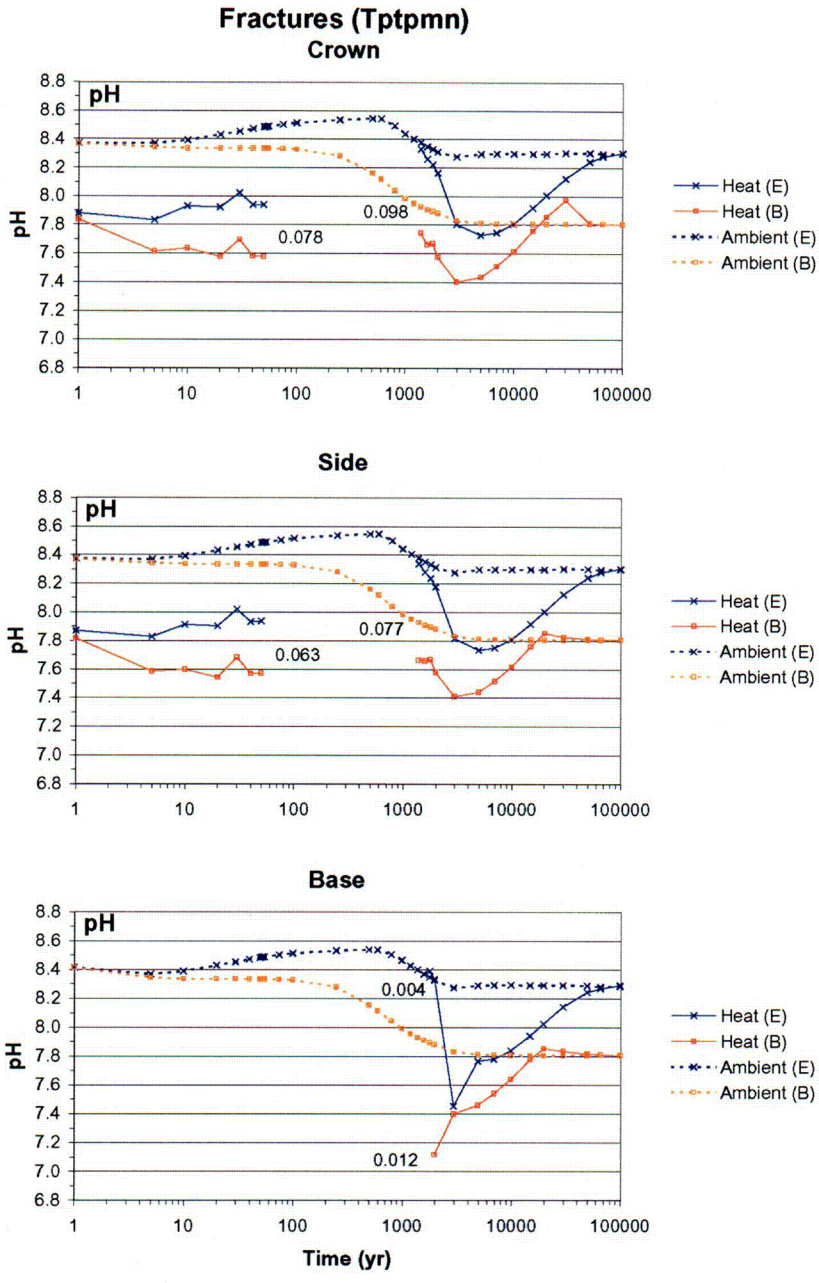

DTN: LB0011DSTTHCR1.001 [154759]

NOTE: The dryout period is left blank. Numbers by each curve indicate the last output liquid saturation before dryout and the first output liquid saturation during rewetting.

Figure 6.5-9. THC Simulation (Tptpmn Model): Time Profiles of the Modeled pH of Fracture Water at Three Drift-Wall Locations under Heating (Heat) and Non-Heating (Ambient) Conditions for the Extended (E) and Base-Case (B) Geochemical Systems

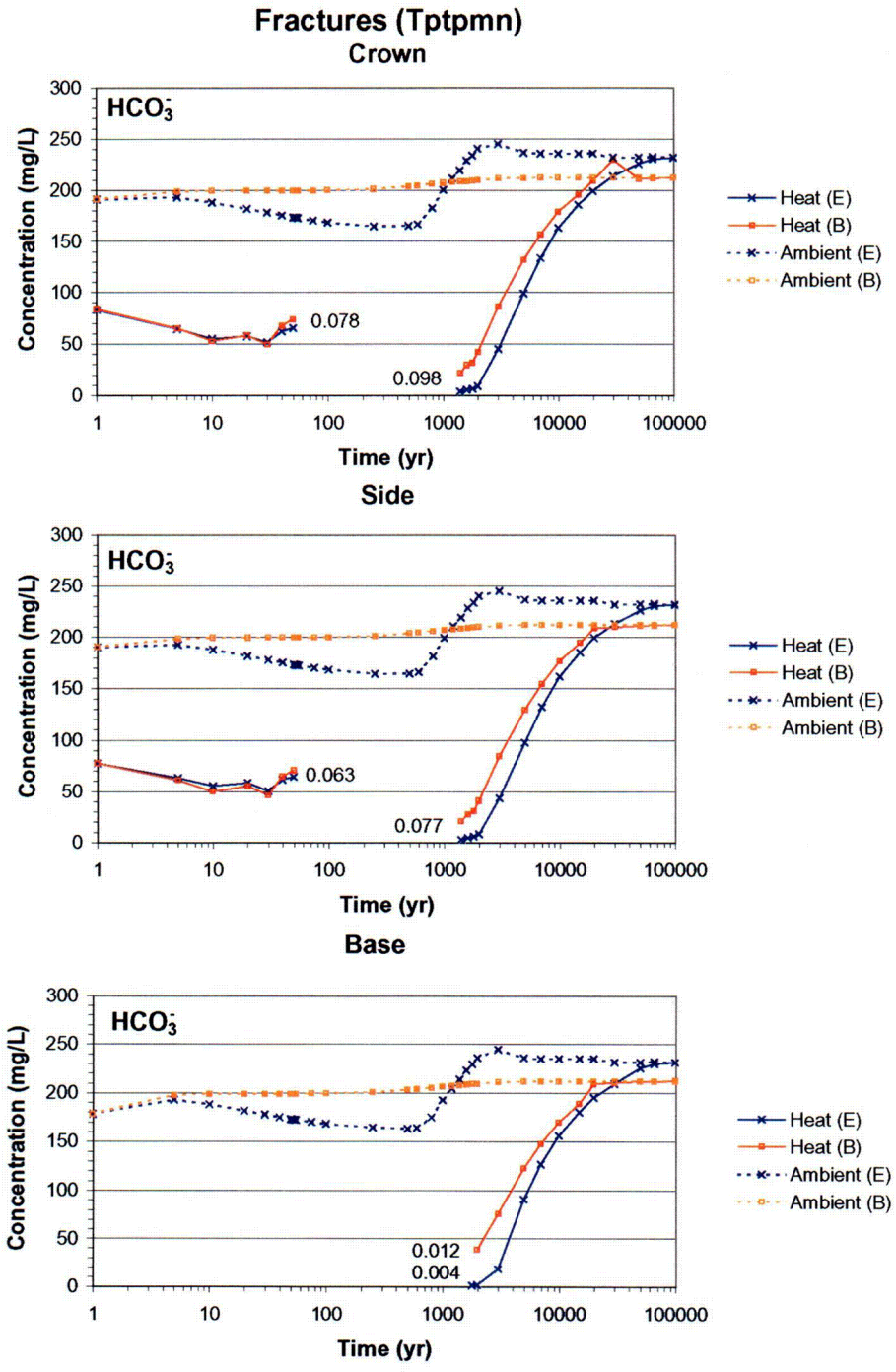

DTN: LB0011DSTTHCR1.001 [154759]

NOTE: The dryout period is left blank. Numbers by each curve indicate the last output liquid saturation before dryout and the first output liquid saturation during rewetting.

Figure 6.5-10. THC Simulation (Tptpmn Model): Time Profiles of Modeled Total Aqueous Carbonate Concentrations (as HCO_3^-) in Fracture Water at Three Drift-Wall Locations under Heating (Heat) and Non-Heating (Ambient) Conditions for Extended (E) and Base-Case (B) Geochemical Systems

C13

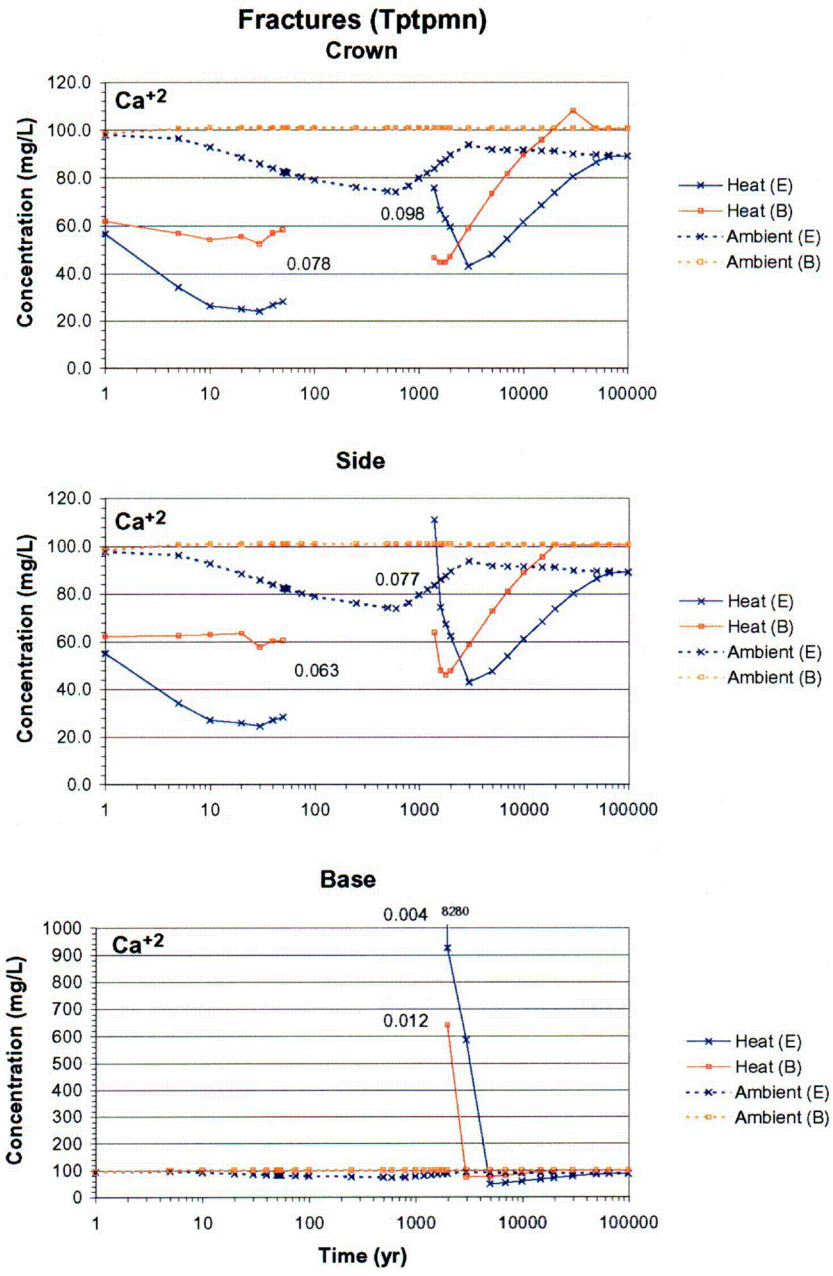

DTN: LB0011DSTTHCR1.001 [154759]

NOTE: The dryout period is left blank. Numbers by each curve indicate the last output liquid saturation before dryout and the first output liquid saturation during rewetting.

Figure 6.5-11. THC Simulation (Tptpmn Model): Time Profiles of Modeled Total Aqueous Calcium Concentrations in Fracture Water at Three Drift-Wall Locations under Heating (Heat) and Non-Heating (Ambient) Conditions for Extended (E) and Base-Case (B) Geochemical Systems

C14

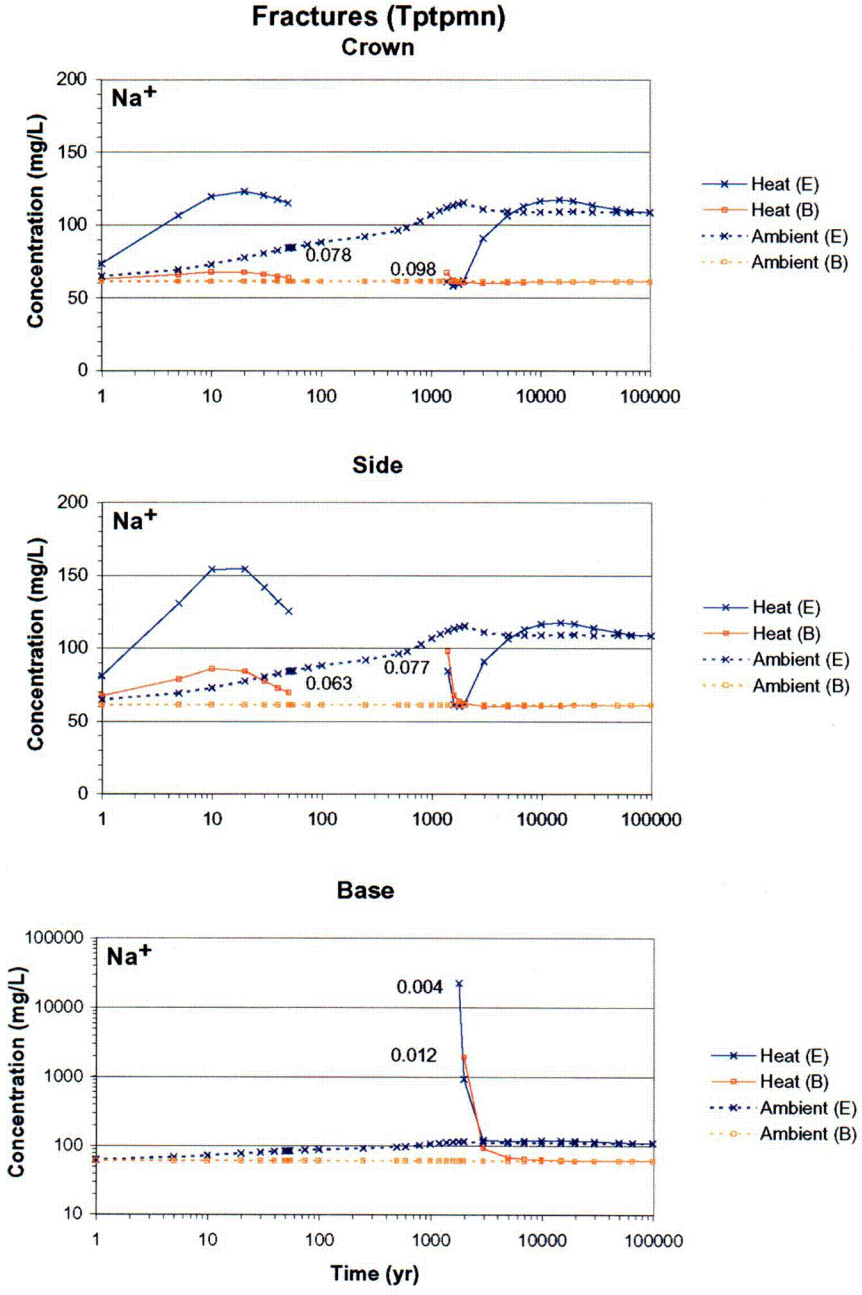

DTN: LB0011DSTTHCR1.001 [154759]

NOTE: The dryout period is left blank. Numbers by each curve indicate the last output liquid saturation before dryout and the first output liquid saturation during rewetting.

Figure 6.5-12. THC Simulation (Tptpmn Model): Time Profiles of Modeled Total Aqueous Sodium Concentrations in Fracture Water at Three Drift-Wall Locations under Heating (Heat) and Non-Heating (Ambient) Conditions for Extended (E) and Base-Case (B) Geochemical Systems

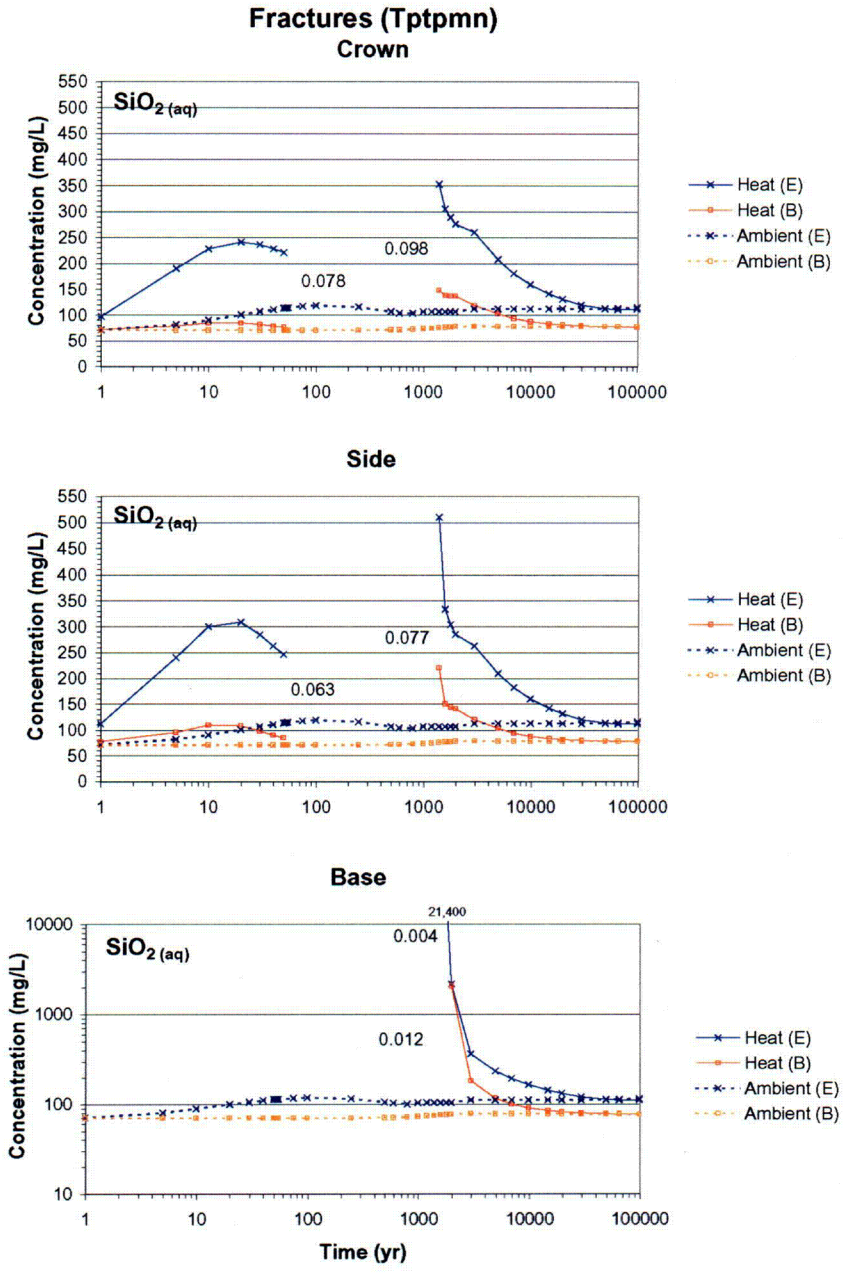

DTN: LB0011DSTTHCR1.001 [154759]

NOTE: The dryout period is left blank. Numbers by each curve indicate the last output liquid saturation before dryout and the first output liquid saturation during rewetting.

Figure 6.5-13. THC Simulation (Tptpmn Model): Time Profiles of Modeled Total Aqueous Silica Concentrations in Fracture Water at Three Drift-Wall Locations under Heating (Heat) and Non-Heating (Ambient) Conditions for Extended (E) and Base-Case (B) Geochemical Systems

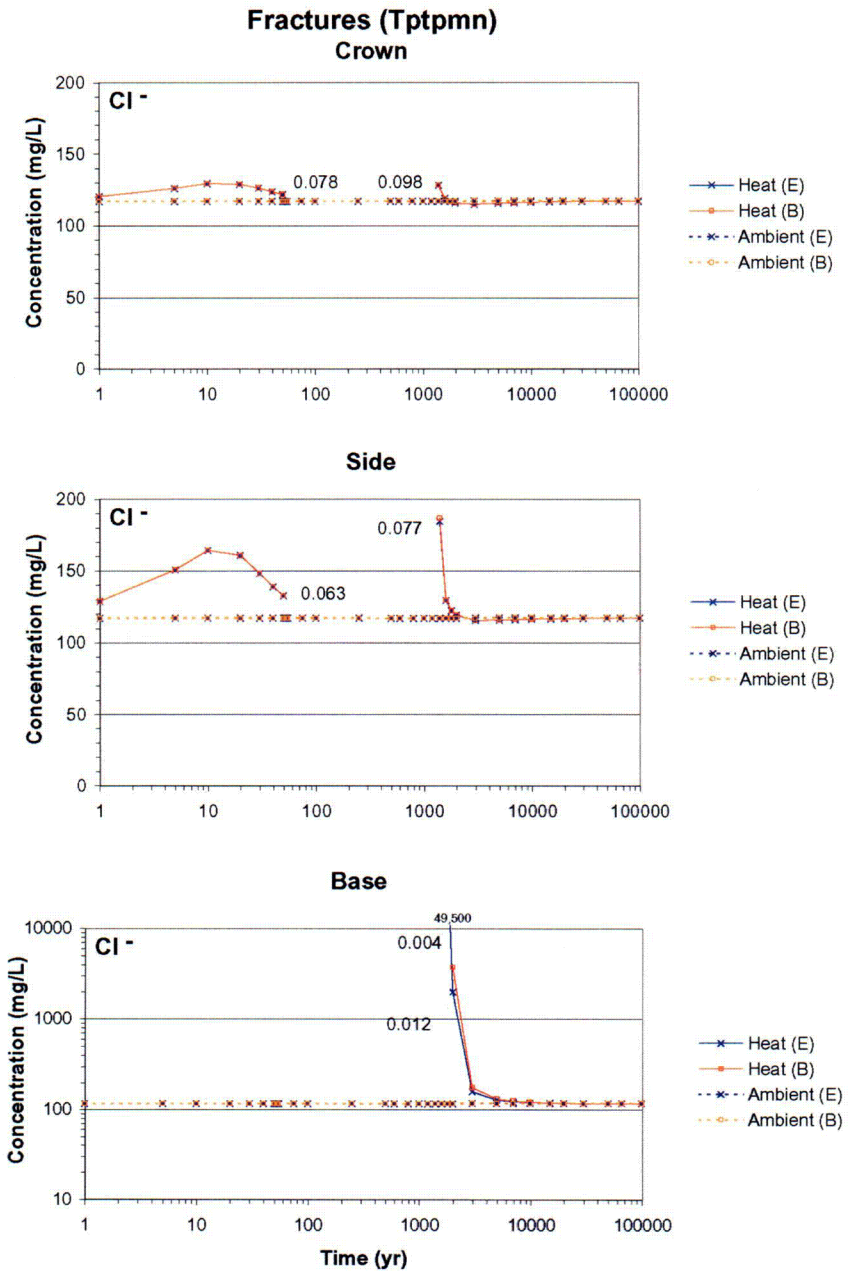

DTN: LB0011DSTTHCR1.001 [154759]

NOTE: The dryout period is left blank. Numbers by each curve indicate the last output liquid saturation before dryout and the first output liquid saturation during rewetting.

Figure 6.5-14. THC Simulation (Tptpmn Model): Time Profiles of Modeled Total Aqueous Chloride Concentrations in Fracture Water at Three Drift-Wall Locations under Heating (Heat) and Non-Heating (Ambient) Conditions for Extended (E) and Base-Case (B) Geochemical Systems

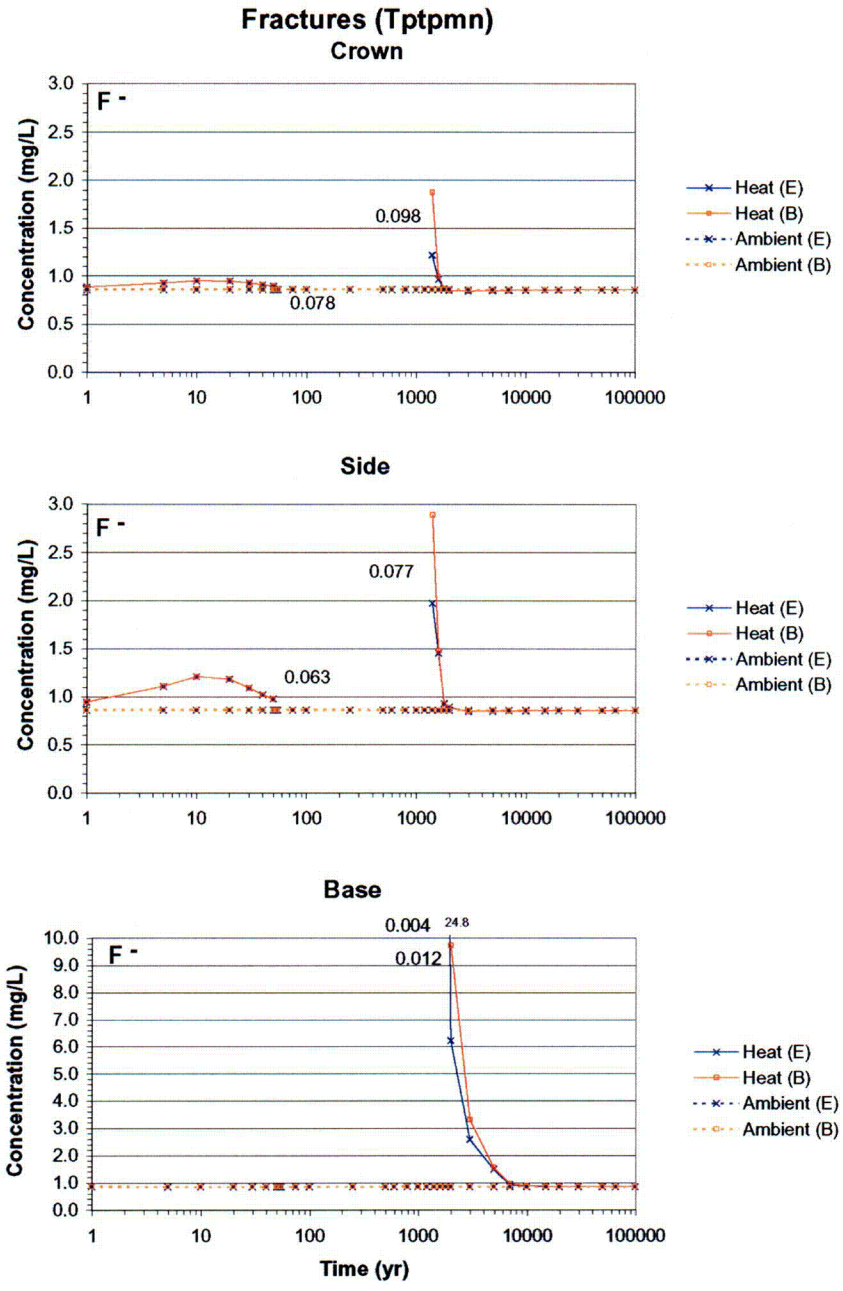

DTN: LB0011DSTTHCR1.001 [154759]

NOTE: The dryout period is left blank. Numbers by each curve indicate the last output liquid saturation before dryout and the first output liquid saturation during rewetting.

Figure 6.5-15. THC Simulation (Tptpmn Model): Time Profiles of Modeled Total Fluoride Concentrations in Fracture Water at Three Drift-Wall Locations under Heating (Heat) and Non-Heating (Ambient) Conditions for Extended (E) and Base-Case (B) Geochemical Systems

C18

Modeled fracture porosities around the drift all decrease over time (negative). The maximum reductions occur approximately 8 to 9 m above the drift center, in a pattern approximately delineating the maximum extent of the dryout zone (Figure 6.5-16). At this location, the porosity decreases by approximately 1% after 20,000 years and 3% after 100,000 years. This reduction results primarily from the precipitation of amorphous silica and calcite. Amorphous silica precipitates mostly from 600 to 2,000 years, accounting for approximately a 0.5% porosity reduction. Amorphous silica precipitation is followed at later times by calcite precipitation as infiltration waters, replenished in aqueous carbonate and calcium, are heated as they percolate back towards the drift where temperatures remain above ambient values for several tens of thousands of years. Lesser amounts of gypsum (to a maximum near 0.3% volume at 600 years) and very small amounts of fluorite also precipitate in the same zone, but dissolve rapidly upon rewetting. The magnitude of porosity changes predicted for the base-case and extended-case systems is similar. The maximum porosity reduction is predicted with the extended case, but the overall extent of the decrease is slightly larger for the base case because of somewhat more widespread calcite precipitation than with the extended case. The predicted porosity change is smaller than modeled with the REV02 simulations (Section 6.8), because the code version (TOUGHREACT V2.3 (LBNL 2001 [153101])) used for REV01 does not account for mineral precipitation into dry gridblocks upon influx of water. Also, this older model considers a somewhat larger fracture porosity than more recent simulations (Table 6.4-1).

Note that in this model, zeolites in fractures around the drift (mostly stellerite) primarily dissolve. Small amounts of stellerite (less than 0.02% volume) precipitate in the rock matrix mostly below the drift during the initial cooling stage, but redissolve entirely after approximately 5,000 years. More recent simulations (Section 6.8) with somewhat revised stellerite thermodynamic properties predict more stellerite precipitation than in this simulation (although not much more). Clay minerals are predicted to precipitate around the drift, but only in minute quantities (less than 10^{-4}% by volume). Figures showing predicted patterns for some of these minerals around the drift are shown in Section 6.6, where the effect of heterogeneous permeability fields are investigated. Predicted mineral patterns of illite and stellerite are similar to those shown in Section 6.7.5.2 for the Tptpll THC Model REV01.

Slightly higher liquid saturations in fractures during the cooling phase are calculated when THC processes are considered (Figure 6.5-17). This is the direct result of increased capillarity caused by permeability reduction. However, the permeability reduction is not large enough to significantly affect modeled fluxes at the drift crown (Figure 6.5-18) or the general thermohydrology around the drift. This is in contrast with more recent simulations (Section 6.8) incorporating updated rock properties and a better treatment of mineral precipitation at the boiling front. These more recent simulations show a significant diversion of percolating water around the drift because of a zone of reduced permeability above the drift (Section 6.8.5.2). In the current case, the only visible effect of mineral precipitation is a slight flux increase (relative to ambient values) after 20,000 years predicted with the extended geochemical system (Figure 6.5-18). This effect is caused by minor flow focusing, stemming from an uneven precipitation of calcite artificially enhanced by numerical discretization effects. In this case, an average of a few gridblocks would give a closer approximation to the flux at the drift crown. Changes in permeability caused by THC effects around the drift are further investigated for alternative models in the next sections. It should also be noticed that steps in the curves displayed for ambient simulations in Figures 6.5-17 and 6.5-18 reflect a change in infiltration rates input into the model (Table 6.5-3).

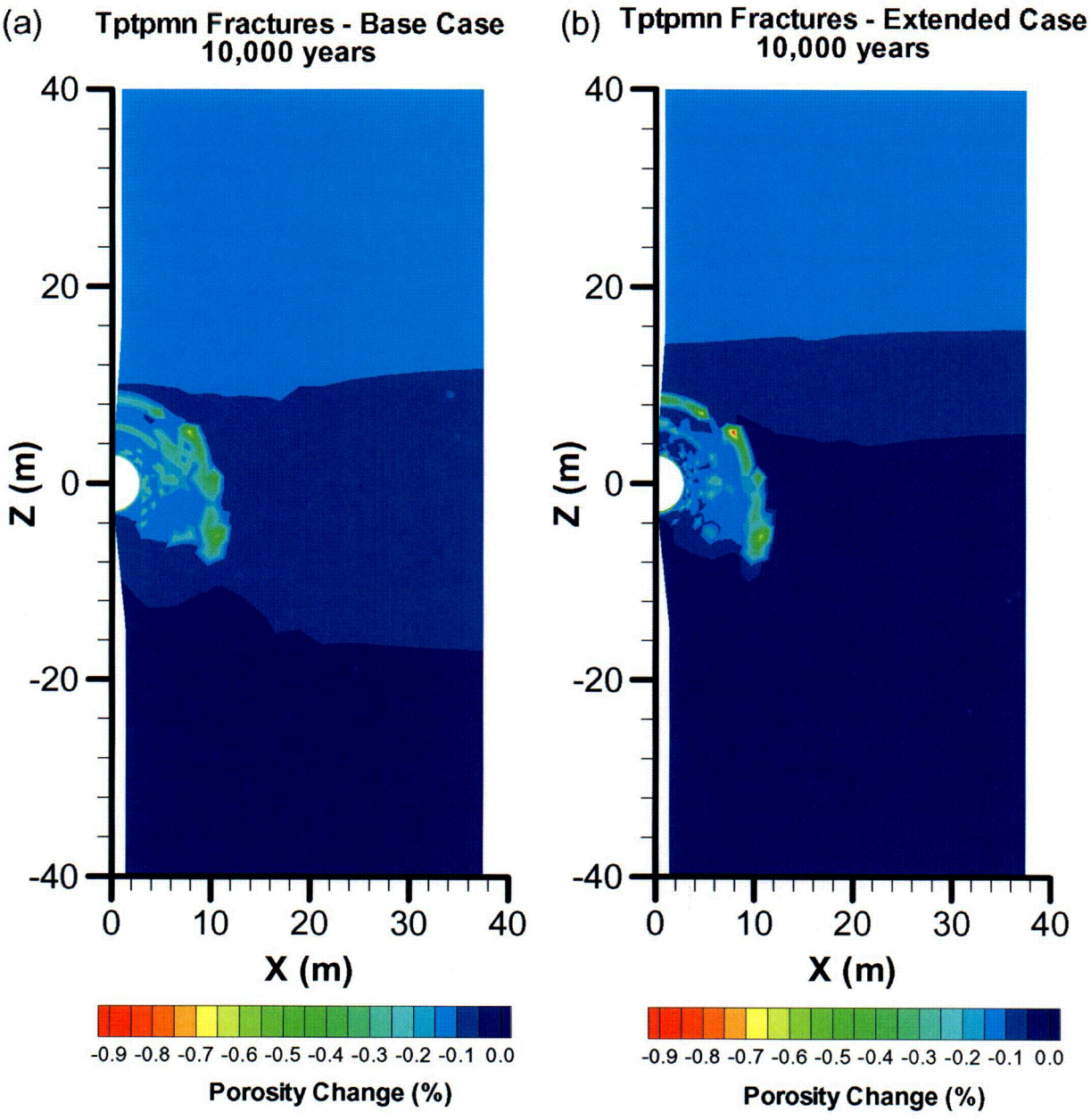

DTN: LB0011DSTTHCR1.002 [161282]

NOTE: Decrease in porosity is primarily due to the precipitation of calcite and amorphous silica.

Figure 6.5-16. THC Simulation (Tptpmn Model): Contour Plot of Modeled Fracture Porosity Change at 10,000 Years for (a) Base-Case and (b) Extended Geochemical Systems

C19

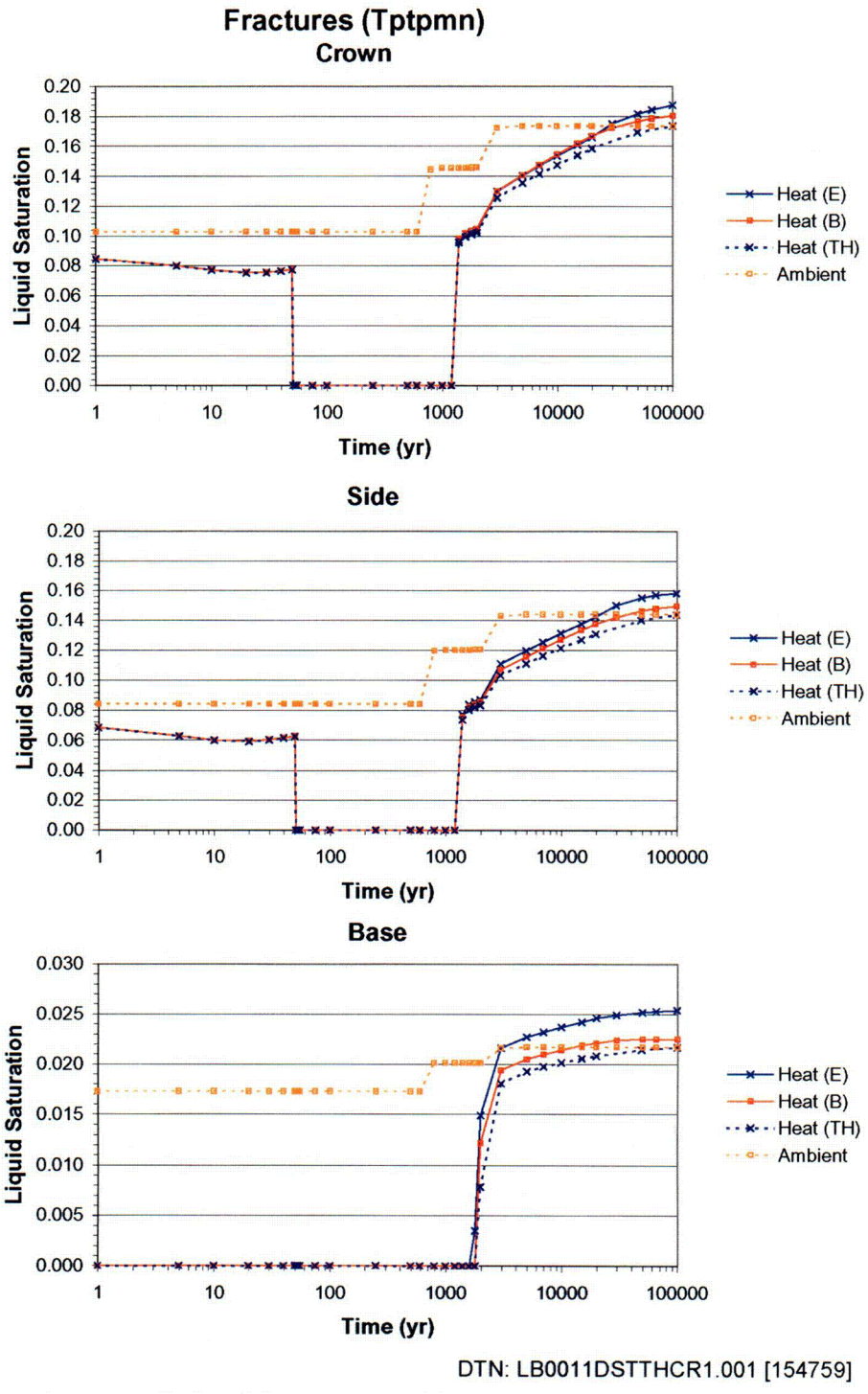

DTN: LB0011DSTTHCR1.001 [154759]

Figure 6.5-17. TH and THC Simulations (Tptpmn Model): Comparison of Modeled Liquid Saturations in Fractures at Three Drift-Wall Locations under Heating (Heat) and Non-Heating (Ambient) Conditions for the Extended (E) and Base-Case (B) Geochemical Systems, and for the TH Simulation

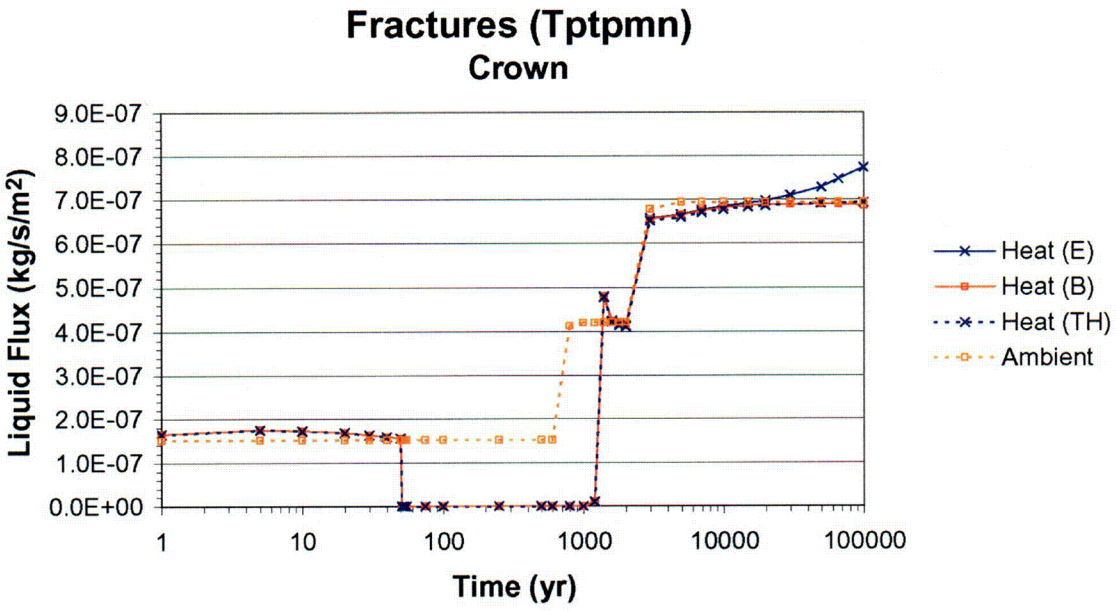

DTN: LB0011DSTTHCR1.001 [154759]

NOTE: The small flux increase above ambient values after 20,000 years is in part due to numerical discretization effects (see text).

Figure 6.5-18. TH and THC Simulations (Tptpmn Model): Comparison of Modeled Liquid Flux at the Drift Crown in Fractures under Heating (Heat) and Non-Heating (Ambient) Conditions for the Extended (E) and Base-Case (B) Geochemical Systems, and for the TH Simulation

C20A